Observation of Bose Polarons
in a Quantum Gas Mixture

Nils Byg Jørgensen
Department of Physics and Astronomy
Aarhus University, Denmark

PhD Thesis
January 2018

ABSTRACT

Ultracold atomic gases provide an excellent setting for studying regimes of quantum physics that are not accessible otherwise. A principal element is the freedom to choose the interaction strength between atoms arbitrarily, facilitated by Feshbach resonances. In this thesis, a series of studies on ultracold Bose mixtures with tunable interactions are presented. The studies are divided into three different research paths, each exploring a different area of physics.

The primary research path concerns the physics of impurities. For the first time, the polaron quasiparticle in a Bose-Einstein condensate is observed. Experimentally, the polaron is studied by performing radio frequency spectroscopy of a ^{39}K Bose-Einstein condensate, which is used to simultaneously create and characterize the impurity quasiparticle. The observations are successfully compared to a comprehensive theory, which confirms the existence of well-defined polaron states. The results are further supported by several models which treat relevant physical aspects.

The second research path investigates the properties of dual-species Bose-Einstein condensates of ^{39}K and ^{87}Rb. The main focus is the phase separation of the two components, which can be controlled by tunable interactions. The in-trap distributions and expansion behavior is studied theoretically and compared with experimental observations, which reveals interesting features. The studies show that it is challenging to predict the phase separation from the interaction strengths only.

In the third research path, the three-body physics of KRb mixtures is explored. Previously, the first observation of a heteronuclear Efimov resonance was made in a ^{41}K^{87}Rb mixture, but has since been debated. Here, thorough measurements are performed in both ^{41}K^{87}Rb and ^{39}K ^{87}Rb mixtures. No Efimov resonances are observed in either mixture. Preliminary measurements performed in a single-component ^{39}K ensemble are presented as well, and reveal an intriguing temperature dependence of an Efimov resonance.

The results presented in the thesis open up for exciting new opportunities to study unexplored regions in the realm of quantum mechanics.

RESUMÉ (DANISH ABSTRACT)

Ultrakolde atomare gasser gør det muligt at udforske områder af kvantefysikken, der ellers ikke er tilgængelige. Et af nøgleelementerne er adgangen til frit at vælge interaktionsstyrken imellem atomer igennem brugen af Feshbach-resonanser. I denne afhandling præsenteres en række studier af ultrakolde blandede Bose-gasser med regulerbare interaktioner. Studierne forgrener sig ud i tre forskellige retninger, der hver udforsker et område af fysikken.

Den vigtigste forskningsretning omhandler fysikken bag urenheder. For først gang er kvasipartiklen kaldet en polaron blevet observeret i et Bose-Einstein-kondensat. Polaronen er studeret ved at foretage spektroskopi af et ^{39}K Bose-Einstein-kondensat, hvilket på en gang danner og karakteriserer urenhedskvasipartiklen. Observationerne bliver sammenlignet med en omfattende teori, hvilket bekræfter eksistensen af veldefinerede polarontilstande. Resultaterne bliver yderligere bakket op af flere modeller, der omhandler relevante fysiske aspekter.

Den anden forskningsretning undersøger egenskaber bag dobbelte Bose-Einstein-kondensater af ^{39}K og ^{87}Rb. Der bliver fokuseret på faseseparationen imellem de to komponenter, der kan kontrolleres igennem interaktionerne. Fordelingen af atomerne i fælden og deres opførsel, når de ekspanderer, bliver studeret teoretisk og sammenlignes med eksperimentelle observationer, hvilket afslører interessante egenskaber. Studierne viser, at det er udfordrende at forudse fasesepareration udelukkende ud fra interaktionerne.

I den tredje forskningsretning udforskes trelegemefysikken i KRb-blandinger. Den første observation af en heteronuklear Efimov-resonans blev foretaget i en ^{41}K^{87}Rb-blanding, men er siden da blevet blevet kritiseret. Som en del af denne afhandling er der udført grundige målinger i både ^{41}K^{87}Rb- og ^{39}K ^{87}Rb-blandinger, men der observeres ingen Efimov-resonanser. Her præsenteres desuden indledende målinger af en Efimov-resonans i ^{39}K, der viser en uventet temperaturafhængighed.

Resultaterne, der præsenteres i denne afhandling, giver anledning til nye muligheder for at undersøge uudforskede områder af kvantefysikkens verden.

PREFACE

This thesis covers the scientific research I have conducted during my PhD studies. The work has mainly been carried out at the Multi Species Quantum Gases Experiment in the Ultracold Quantum Gases Group at the Department of Physics and Astronomy at Aarhus University. This experimental setup is capable of cooling down ensembles of potassium and rubidium atoms to ultracold temperatures, which allows studies of quantum physics.

I was admitted in the PhD program without a Master's degree, which permitted a duration of four years to my PhD education. This is a standard procedure at the institution. The studies officially started August 1st, 2013, but due to parental leave, the education was extended until January, 2018.

The past years have been quite a journey. Many new friends and acquaintances, exciting research, conferences around the world, fathering two children. I have greatly developed and matured both as a researcher, and as a person.

I would like to use this opportunity to thank some people. First, a big thanks to my supervisor Jan Arlt. We had many great scientific discussions during the past years, and he has really been a great source of knowledge. I am grateful for the amount of liberty he has granted me in my day-to-day work life. Along these lines, I would also like to thank Jacob Sherson and Georg Bruun, who have also advised and scientifically mentored me during my education.

A special thanks to Nils Winter and Lars Wacker, who trained and educated me in the lab. They have taught me a large part of the technical

skills I have acquired during my studies. I am sure their German spirit will linger on in the lab for many years to come.

During my education Danny Birkmose and Kristoffer Theis Skalmstang both conducted their Master's thesis projects with us. Both made huge technical and scientific contributions, as well as provided great company.

I would also like to thank Thomas Guldager Skov and Magnus Graf Skou, the next generation of physicists in the lab. I sincerely enjoyed mentoring them, and they both show great promise as scientists. I believe great research awaits.

Furthermore, I would like to thank friends and family for being a part of my life. Although I have certainly enjoyed academia all the way through, it is nice to encounter the real world once in a while.

Lastly, for proofreading, I would like to give my thanks Thomas Guldager Skov, Magnus Graf Skou, Jan Arlt, and Karl Anker Jørgensen. Finally, for careful proofreading of the entire thesis, an enormous thanks to Anne Viborg.

I hope you will enjoy reading the thesis.

Nils Byg Jørgensen

LIST OF PUBLICATIONS

N. B. Jørgensen, M. G. Bason, and J. F. Sherson, One- and two-qubit quantum gates using superimposed optical-lattice potentials, Phys. Rev. A **89**, 032306 (2014).

L. Wacker, N. B. Jørgensen, D. Birkmose, R. Horchani, W. Ertmer, C. Klempt, N. Winter, J. Sherson, and J. J. Arlt, Tunable dual-species Bose-Einstein condensates of ^{39}K and ^{87}Rb, Phys. Rev. A **92**, 053602 (2015).

K. L. Lee, N. B. Jørgensen, I.-K. Liu, L. Wacker, J. J. Arlt, and N. P. Proukakis, Phase separation and dynamics of two-component Bose-Einstein condensates, Phys. Rev. A **94**, 013602 (2016).

N. B. Jørgensen, D. Birkmose, K. Trelborg, L. Wacker, N. Winter, A. J. Hilliard, M. G. Bason, and J. J. Arlt, A simple laser locking system based on a field-programmable gate array, Rev. Sci. Instrum. **87**, 073106 (2016).

N. B. Jørgensen, L. Wacker, K. T. Skalmstang, M. M. Parish, J. Levinsen, R. S. Christensen, G. M. Bruun, and J. J. Arlt, Observation of attractive and repulsive polarons in a Bose-Einstein condensate, Phys. Rev. Lett. **117**, 055302 (2016).

L. J. Wacker, N. B. Jørgensen, D. Birkmose, N. Winter, M. Mikkelsen, J. Sherson, N. Zinner, and J. J. Arlt, Universal three-body physics in ultracold KRb mixtures, Phys. Rev. Lett. **117**, 163201 (2016).

K. L. Lee, N. B. Jørgensen, L. Wacker, M. G. Skou, K. T. Skalmstang, J. J. Arlt, and N. P. Proukakis, Time-of-flight expansion of binary Bose-Einstein condensates at finite temperature, arXiv:1712.07481, submitted to New J. Phys. (2017).

L. Wacker, N. B. Jørgensen, K. T. Skalmstang, M. G. Skou, A. G. Volosniev, and J. J. Arlt, Temperature dependence of an Efimov resonance in ^{39}K, in preparation.

L. A. P. Ardila, N. B. Jørgensen, K. T. Skalmstang, J. J. Arlt, S. Giorgini, G. M. Bruun, and T. Pohl, Analysis of Bose polaron observations, in preparation.

CONTENTS

CHAPTER 1

INTRODUCTION

More than a 100 years ago, Niels Bohr hypothesized the quantization of the hydrogen atom, which initiated a new era of perceiving Nature [1]. To this day, the atom remains an essential object of study at the forefront of physics research. Advancements in technology and experimental techniques now allow dilute samples of atoms to be cooled down to temperatures well below a millionth of a kelvin, where the fundamental quantum nature of particles unravels in a striking manner. The hallmark example is the Bose-Einstein condensate where a macroscopic number of particles accumulate in the quantum-mechanical ground state to form a new state of matter where quantum phenomena become apparent [2, 3].

The theory of quantum mechanics has been extremely successful in explaining a vast number of phenomena in our universe. This includes the behavior of subatomic particles, the structure of the periodic table of elements, covalent bonds of molecules, as well as the existance of neutron stars. Quantum mechanics is also essential in modern technology, through inventions such as the transistor and the laser. Currently, the rules of quantum mechanics are being utilized in the development of a

new generation of technology, such as quantum computation, quantum cryptography, and quantum simulation [4].

A quantum simulator employs a versatile physical environment to mimic another system which is otherwise difficult to study [5]. Atomic gases cooled to ultracold temperatures are excellent candidates for such quantum simulators. In particular, atomic trapping potentials can be tailored arbitrarily, the composition of particles within a system can be controlled to a high degree, and different kinds of interactions are available and tunable at will. By these means, ultracold gases have proven to be a capable setting for exploring and probing physical phenomena in parameter regimes which are not accessible in natural condensed matter systems [6].

Especially the prospect of choosing the interaction strength of a system at will has opened up a wealth of research paths [6–10]. This liberty is not restricted to quantum gases of a single component; tunable interactions in multi-component gases allow a wide range of phenomena to be studied. One prominent example is the recent interest of the mobile quantum impurity immersed in a medium with which it interacts. Ground-breaking research performed with ultracold Fermi gases have recently provided many new insights to this fundamental problem in physics [9, 11–16].

In this thesis, studies of ultracold bosonic mixtures with tunable interactions are presented. The research branches into three different directions.

The primary study is the first observation of a polaron in a Bose-Einstein condensate [17, 18]. The polaron is a quasiparticle composed of an impurity and its excitations of the surrounding medium [19, 20], and it is crucial in understanding exotic and technologically important materials [21–23]. However, the general scenario of an impurity interacting with its surrounding is found in many different areas of physics. It is therefore highly interesting to study the properties of impurities and polarons in the flexible environment offered by ultracold mixtures of tunable interactions.

Moreover, the properties of two-species Bose-Einstein condensates with tunable interactions are explored [24–26]. This setting is usable to study the dynamics of interacting macroscopic quantum systems, which

is a non-trivial and highly relevant research field, since it is relevant in understanding a new generation of quantum technology.

The third topic of the dissertation is few-body physics [27, 28]. Quantum mechanical few body-physics is conceptually simple but offers a remarkable richness, of which the Efimov effect is a primary example. Here, the two-body interactions of three particles produce an intricate spectrum of three-body bound states with universal characteristics. Ultracold quantum gases have become a primary tool for exploring such few-body systems, due to the tunability of interactions. However, since the properties of these systems are universal, the resulting phenomena stretch beyond the field of ultracold gases [10, 29].

The areas of research investigated within each topic are introduced in greater detail later, together with important experimental and theoretical results.

Within the work of this dissertation, two additional studies were carried out but not included in the main text. The first study is purely theoretical and considers using ultracold atoms in superimposed optical lattice potentials for one- and two-qubit quantum gates [30]. The second study is mainly technical and presents a simple new method to stabilize a laser frequency by the employment of a field-programmable gate array to implement laser lock electronics [31]. The published manuscripts are found in Appendix A.

1.1 Ultracold mixtures of ^{39}K and ^{87}Rb

The research of this thesis utilizes the tunable interactions offered by ultracold mixtures of bosonic ^{39}K and ^{87}Rb, briefly introduced here. By tuning the magnetic field, the interaction strengths within these systems can be altered through the employment of Feshbach resonances [8].

The Feshbach resonance structure for a mixture of ^{87}Rb and ^{39}K in the $|F = 1, m_F = -1\rangle$ hyperfine state is introduced in Fig. 1.1(a). The interaction strength is parameterized by the scattering length a, which is shown in units of the Bohr radius a_0. Two ^{39}K Feshbach resonances offer a wide region of positive scattering length [32], and within this region, an interspecies Feshbach resonance is located [33]. This remarkable struc-

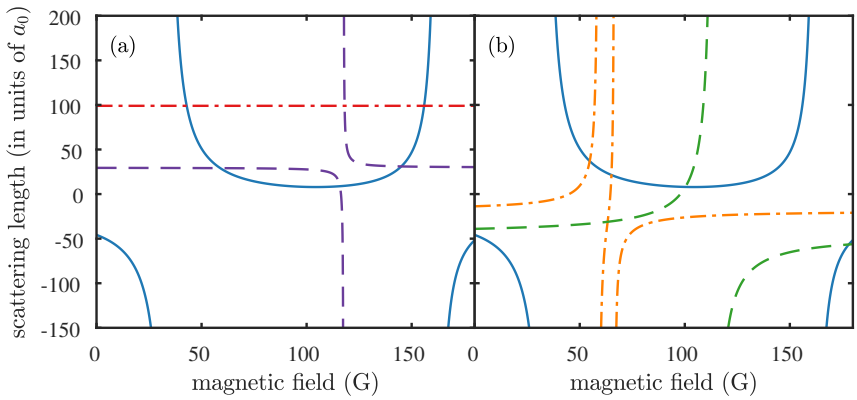

Figure 1.1: Feshbach resonance structure and interaction strengths of ultracold ^{39}K and ^{87}Rb. (a) Scattering length of ^{39}K and ^{87}Rb in the $|F=1, m_F=-1\rangle$ state where the solid blue line is for ^{39}K, dash-dotted red line is for ^{87}Rb and dashed purple line is between ^{39}K and ^{87}Rb. (b) Scattering length in ^{39}K spin mixtures, where the solid blue line is for the $|F=1, m_F=-1\rangle$ state, dash-dotted orange line is for the $|F=1, m_F=0\rangle$ state, and dashed green line is between the two states.

ture allows production of mixtures and dual-species condensates of ^{39}K and ^{87}Rb with tunable interactions. Otherwise, ^{39}K is not an obvious candidate for a constituent in dual-species condensates since it has a negative background scattering length, which prohibits the production of large stable condensates [34, 35].

The region of positive scattering length additionally contains Feshbach resonances which open up possibilities for tuning interactions of spin mixtures of ^{39}K atoms, as shown in Fig. 1.1(b). An interstate resonance allows tunable interactions between ^{39}K atoms in the $|1,-1\rangle$ and $|1,0\rangle$ states and, furthermore, the interactions of atoms in the $|1,0\rangle$ state are tunable by two Feshbach resonances [32, 36].

The ^{39}K ^{87}Rb system is thus rich in possibilities. Not only can the interaction within one species be modified, but interactions between species and spin states are also tunable.

The experimental apparatus used and described within this dissertation is additionally capable of producing ultracold mixtures of ^{41}K and ^{87}Rb, a system which also contains Feshbach resonances allowing tun-

able interspecies interactions. In the absence of other species, only very narrow Feshbach resonances exists for both ^{41}K and ^{87}Rb atoms [32, 37].

1.2 Thesis outline

Chapter 2, Properties and Interactions of Ultracold Mixtures: Some of the key physical principles important for ultracold quantum gases are explored, including Bose-Einstein condensation of non-interacting bosons, interatomic interactions, and the Gross-Pitaevskii equation. The three main research topics of the thesis are also introduced in great detail. This includes overviews of key experimental and theoretical findings.

Chapter 3, Experimental Procedure and Apparatus: The apparatus used within this dissertation is introduced, and the procedure to obtain ultracold samples is summarized.

Chapter 4, Tunable Dual-Species Bose-Einstein Condensates: A Series of studies of dual-species Bose-Einstein condensates of ^{39}K and ^{87}Rb are presented. First, the relevant Feshbach resonance is characterized experimentally. Next, the phase separation and dynamics dual-species condensates are examined theoretically. Finally, the expansion properties of dual-species condensates are investigated.

Chapter 5, Three-Body Physics in ^{39}K and Mixtures of KRb: The three-body physics in the two isotope mixtures ^{39}K ^{87}Rb and ^{41}K^{87}Rb are studied. Furthermore, the temperature dependence of an Efimov resonance in ^{39}K is characterized.

Chapter 6, Observation of Polarons in a Bose-Einstein Condensate: The observation of polarons in a Bose-Einstein condensate is presented. This includes a characterization of the relevant Feshbach resonance, a examination of the experimental approach and procedure, and a detailed discussion of the results. Furthermore, a number of different models are presented to better understand the experimental findings.

Chapter 7, Thesis Conclusions: The key results of the thesis are summarized and an outlook is provided.

CHAPTER 2

PROPERTIES AND INTERACTIONS OF ULTRACOLD MIXTURES

In this chapter a number of selected relevant topics will be examined theoretically. This includes basic theory of Bose-Einstein condensation, theory of interatomic interactions, and more specific subjects such as Efimov and polaron physics. The main aim of this chapter is to outline some central theoretical derivations and theories, not to present them in full detail. Some topics are also covered more thoroughly by presenting relevant experimental results from literature. This serves as both introduction and perspective for the experimental results presented later in the thesis.

The phenomenon of Bose-Einstein condensation concerns a macroscopic occupation of the quantum-mechanical ground state and was originally hypothesized by S. N. Bose and A. Einstein in 1924–1925. The theory was first developed by Bose for quanta of light, known today as photons [38], and afterwards for particles with mass by Einstein [39, 40]. These original theoretical works considered particles without interac-

tions, and since ultracold atomic gases typically have relatively weak interactions, these theories apply well.

Bose-Einstein condensation is, however, also found in other systems. The superfluidity of He, which was discovered in 1938, is believed to be due to partial Bose-Einstein condensation, and many properties of superfluid He are similar to those of gaseous condensates. However, the high particle density of liquid He results in strong interactions, and theories of Bose-Einstein condensation must be heavily modified to describe these systems. In fact, due to interactions, only about 10 % or less of the He atoms can enter a Bose-Einstein condensate [41].

The creation of Bose-Einstein condensates in dilute gases in 1995 was therefore the first realization of "true" Bose-Einstein condensates [2, 3]. More recently, Bose-Einstein condensation has also been observed in systems of quasiparticles, which are collective excitations that are effectively described as particles. Quasiparticle condensates composed of magnons [42], exitons [43] and exciton polaritons [44] have thus also been observed. Even more recently, condensation of photons was observed in an optical microcavity [45], bringing to life the original theory of Bose.

The interactions between neutral alkali atoms are mainly mediated through collisions. Due to the ultralow temperatures of quantum gases, the collisions can be described in a relatively simple framework. One of the powerful tools of quantum gases is magnetic Feshbach resonances which allow the strength of the collisional interactions to be tuned. The ability to change the interaction in a system to arbitrary values opens up a wealth of research directions. This includes the main studies conducted within this thesis; dual-species condensates with tunable interactions, three-body physics and the Efimov effect in KRb mixtures, and the observation of the polaron quasiparticle in a Bose-Einstein condensate.

The rest of this chapter is structured as follows. The theory behind condensation of non-interacting bosons as suggested by Bose and Einstein is reviewed in Sec. 2.1. Then, interactions in ultracold gases is examined in Sec. 2.2, and the possibility to tune these interactions by utilizing Feshbach resonances is introduced in Sec. 2.3. The impact of interactions to the condensed state is discussed in Sec. 2.4 by outlining the

derivation of the Gross-Piteavskii equation. Additionally, the equation is extended to include two components, which is directly relevant for experimental work presented later in the thesis. The final two sections concern specific research topics which are also relevant for experimental work presented later. In Sec. 2.5, Efimov physics is introduced, and, finally, in Sec. 2.6 polaron physics in ultracold gases is examined.

2.1 Condensation of Non-Interacting Bosons

Bose-Einstein condensation is a macroscopical accumulation of particles in the quantum-mechanical ground state. The phenomenon arises from the quantum statistics of non-interacting particles. The derivations presented in the following are from reference [41].

In general, quantum effects appear if the density of particles satisfies

$$\frac{N}{V}\lambda_{\mathrm{dB}}^3 \gtrsim 1, \tag{2.1}$$

where N is the number of particles in a volume V and

$$\lambda_{\mathrm{dB}} = \frac{h}{\sqrt{2\pi m k_{\mathrm{B}} T}} \tag{2.2}$$

is the thermal de Broglie wavelength where h is the Planck constant, k_{B} is the Boltzmann constant, m is the particle mass, and T is the temperature.

If Eq. (2.1) is fulfilled, the wave functions of different particles overlap due to a large de Broglie wavelength and effects of quantum mechanics are important.

In quantum mechanics particles are sorted into two catagories depending on their spin; fermions and bosons. Bosons have integer spin and do not obey the Pauli exclusion principle. Indistinguishable bosons are thus able to accumulate in a single quantum state. By assuming that light quanta have this behavior, Bose derived Planck's law of radiation without any assumptions from classical physics [38]. This idea was extended from light quanta to matter particles by Einstein [39, 40], and the concept of a Bose gas was born.

A Bose gas is governed by Bose-Einstein statistics which dictate that the mean occupation number of the single-particle state ν is given by the Bose distribution function

$$f_{\mathrm{BE}}(\epsilon_\nu) = \frac{1}{\mathrm{e}^{(\epsilon_\nu-\mu)/k_{\mathrm{B}}T}-1}, \tag{2.3}$$

where μ is the chemical potential and ϵ_ν is the energy of the state. At high temperatures μ lies well below the energy of the lowest energy state ϵ_0 and the distribution can be approximated by the Maxwell-Boltzmann distribution $f_{\mathrm{BE}}(\epsilon_\nu) \approx \mathrm{e}^{-(\epsilon_\nu-\mu)/k_{\mathrm{B}}T}$. At lower temperatures, the chemical potential approaches ϵ_0 from below, but can never exceed the energy of this lowest state, as the Bose distribution function would become negative, which is unphysical.

If at any point the number of particles in the ground state becomes large, the system has a Bose-Einstein condensate. The temperature at which this happens is denoted the critical temperature of Bose-Einstein condensation T_{c}. When the system does not have a condensate, all particles N can be accounted for by considering particles in excited states only N_{ex}. The greatest value of μ for which this is the case is when μ equals the energy of the lowest energy state of the system ϵ_0 which can be set to 0. Using a semi-classical approximation where the energy spectrum is treated as a continuum, the number of particles at the critical temperature can be expressed as

$$N = N_{\mathrm{ex}}(T_{\mathrm{c}}, \mu = 0) = \int_0^\infty \mathrm{d}\epsilon \frac{g(\epsilon)}{\mathrm{e}^{\epsilon/k_{\mathrm{B}}T_{\mathrm{c}}}-1}, \tag{2.4}$$

where $g(\epsilon)$ is the density of states. In a box of volume V the density of states is

$$g(\epsilon) = \frac{V m^{3/2}}{2^{1/2}\pi^2\hbar^3}\epsilon^{1/2}, \tag{2.5}$$

where $\hbar$ is Planck's reduced constant, and solving Eq. (2.4) yields

$$k_{\mathrm{B}}T_{\mathrm{c}} = \frac{2\pi\hbar^2 n^{2/3}}{[\zeta(3/2)]^{2/3} m}, \tag{2.6}$$

where ζ is the Riemann zeta function and $n = N/V$ is the density. This critical temperature can also be expressed in terms of the de Broglie wavelength

$$n\lambda_{\mathrm{dB}} = \zeta(3/2) \approx 2.612, \tag{2.7}$$

where the left-hand side is known as the phase-space density ρ. This critical temperature is reminiscent of Eq. (2.1), but now derived stringently for bosons.

In experiments the particles are typically confined by a harmonic trap. For a three-dimensional harmonic oscillator potential of frequencies $\omega_x, \omega_y, \omega_z$, the density of states is

$$g(\epsilon) = \frac{\epsilon^2}{2\hbar^3\omega_x\omega_y\omega_z}, \tag{2.8}$$

which with Eq. (2.4) gives

$$k_{\mathrm{B}}T_{\mathrm{c}} = \frac{\hbar\bar{\omega}N^{1/3}}{[\zeta(3)]^{1/3}} \approx 0.94\hbar\bar{\omega}N^{1/3}, \tag{2.9}$$

where $\bar{\omega}$ is the geometric mean of the trap frequencies $\bar{\omega} = (\omega_x\omega_y\omega_z)^{1/3}$. The peak phase-space density in such a trap is

$$\rho_{\mathrm{osc}} = N\left(\frac{\hbar\bar{\omega}}{k_{\mathrm{B}}T}\right)^3. \tag{2.10}$$

If one considers bosons in a harmonic oscillator, it is not surprising that at some sufficiently cold temperature particles start to enter the ground state. What is truly remarkable is that the temperature T_{c} at which this happens corresponds to an energy which is much greater than the energy level spacing of the harmonic oscillator

$$k_{\mathrm{B}}T_{\mathrm{c}} \approx 0.94\hbar\bar{\omega}N^{1/3} \gg \hbar\bar{\omega}, \tag{2.11}$$

for any system with a macroscopic number of particles.

Below T_{c} the number of particles in the Bose-Einstein condensate N_0 is given by

$$N_0(T) = N - N_{\mathrm{ex}}(T). \tag{2.12}$$

By solving Eq. (2.4) for a three-dimensional harmonic oscillator potential with an arbitrary T and $\mu = 0$, a simple expression for the condensate fraction is obtained

$$\frac{N_0}{N} = 1 - \left(\frac{T}{T_c}\right)^3. \tag{2.13}$$

Expressions for the critical temperature of Bose-Einstein condensation and the condensate fraction have thus been derived for bosons without interactions. Corrections to these can enter through e. g. interactions and finite particle numbers, but in most contexts the equations above provide a good estimate of what is found experimentally.

2.2 Interactions Between Ultracold Atoms

In ultracold atomic gases, the interparticle spacing is typically far greater than the range of atom-atom interactions. The interactions are strong, but only occur when atoms are close together. Consequently, two-body interactions are usually dominating, although three- and higher-body interactions can become important, which is discussed later. The many-body wave function of a large ensemble of atoms varies slowly in space, but when two atoms approach, rapid spatial variations occur. To avoid evaluating this in detail, the idea of an effective mean-field interaction is often used, where the short-wavelength degrees of freedom have been integrated out.

In this section, basic concepts behind scattering of neutral atoms are introduced, based on references [41, 46]. It is shown that interactions can be described in terms of a single parameter, denoted the scattering length, which describes the strength of the effective interaction. Additionally, the coupling between different scattering channels gives rise to Feshbach resonances, which makes it possible to tune this interaction strength.

2.2.1 Interatomic Potentials and the van der Waals Radius

Ultracold atoms are usually subject to a polarizing magnetic field. The van der Waals interaction caused by the electric dipole–dipole interaction between atoms has a range which is much greater than the size of an atom. The exact potential between two atoms $V(r)$ is difficult to calculate from theory alone and often a semi-empirical potential is employed. One such potential is the Lennard-Jones potential which can be expressed as

$$V(r) = \frac{C_{12}}{r^{12}} - \frac{C_6}{r^6}. \tag{2.14}$$

It consists of a short-range repulsive term and a long-range attractive term determined by the empirical coefficients C_{12} and C_6, which can be determined experimentally. The range of the long-range van der Waals interaction between two atoms, known as the van der Waals radius R_{vdW}, is connected to the C_6 coefficient

$$R_{\mathrm{vdW}} = \frac{1}{2}\left(\frac{2m_{\mathrm{r}}C_6}{\hbar^2}\right)^{1/4}, \tag{2.15}$$

where $m_{\mathrm{r}} = m_1 m_2/(m_1 + m_2)$ is the reduced mass of the two atoms of masses m_1 and m_2 [8]. This provides a general magnitude of the range of interactions.

The Lennard-Jones potential for a pair of ^{87}Rb atoms compared with their van der Waals radius is shown in Fig. 2.1, with C_6 and C_{12} values from reference [47]. It is remarkable that the length scale of the interactions is far greater than the size of the atoms and the extend of the deep potential. Due to the low energy of the atoms, the long range r^{-6} tail of the van der Waals interaction is significant even at long ranges. Additionally, alkali atoms have a large electrical dipole moment because of their loosely bound electron.

The van der Waals radii relevant to the work within this thesis have been determined to be approximately $65a_0$ for all isotopes of K [48], $83a_0$ for ^{87}Rb [47] and $72a_0$ between K and ^{87}Rb [33], where a_0 is the Bohr radius.

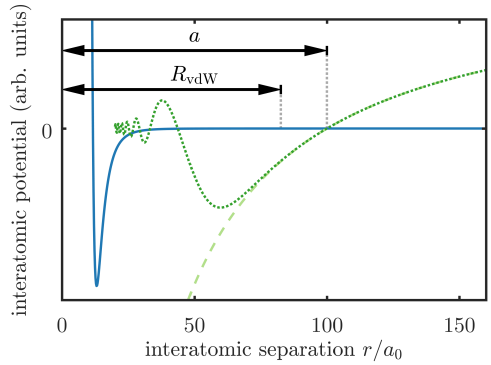

Figure 2.1: The interatomic potential of two ^{87}Rb atoms. The potential shown as a solid blue line is calculated using the Lennard-Jones potential Eq. (2.15). The wave function at large r is shown in dashed light green, and a sketch of a more accurate wave function which oscillates in the presence of an attractive potential is shown as a dotted dark green line. Additionally, the magnitude of the van der Waals radius R_{vdW} and the scattering length a of ^{87}Rb is shown.

2.2.2 Basic Scattering Theory

The elastic scattering between two particles is considered. In coordinates relative to the center-of-mass, the motion satisfies a Schrödinger equation with the mass m_{r}.

The scattering is described by composing the wave function of an incoming wave and a scattered wave

$$\psi(\mathbf{r}) = \psi_{\mathrm{inc}}(\mathbf{r}) + \psi_{\mathrm{sc}}(\mathbf{r}). \tag{2.16}$$

The incoming wave can be described as a plane wave of wave number k, chosen to propagate in the z-direction, and at large r the scattered wave is an outgoing spherical wave

$$\psi(\mathbf{r}) = \mathrm{e}^{\mathrm{i}kz} + f(\theta)\frac{\mathrm{e}^{\mathrm{i}kr}}{r}, \tag{2.17}$$

where $f(\theta)$ is the scattering amplitude. It has been assumed that the interaction between atoms is spherically symmetric, such that f only depends on the angle θ between relative momentum of the atoms before

and after the scattering. The square modulus of f describes the probability $\mathrm{d}\sigma$ of scattering at a certain solid angle $\mathrm{d}\Omega$ as follows

$$\frac{\mathrm{d}\sigma}{\mathrm{d}\Omega} = |f(\theta)|^2, \tag{2.18}$$

which is denoted the differential cross section. By integration of all solid angles the total scattering cross section is obtained

$$\sigma = \int \frac{\mathrm{d}\sigma}{\mathrm{d}\Omega}\mathrm{d}\Omega. \tag{2.19}$$

Due to the axial symmetry of the problem, the wave function can be expanded in terms of Legendre polynomials $P_l(\cos\theta)$

$$\psi(\mathbf{r}) = \sum_{l=0}^{\infty} A_l P_l(\cos\theta) R_{kl}(r), \tag{2.20}$$

where the radial wave function $R_{kl}(r)$ for $r \to \infty$ is given approximately by

$$R_{kl}(r) \approx \frac{1}{kr}\sin\left(kr - \frac{l\pi}{2} + \delta_l\right), \tag{2.21}$$

where δ_l is the scattering phase shift. By inserting Eq. (2.20) and (2.21) into Eq. (2.19) one can obtain an expression for the cross section as a sum of partial wave cross sections

$$\sigma = \sum_{l=0}^{\infty} \sigma_l, \qquad \sigma_l = \frac{4\pi}{k^2}(2l+1)\sin^2\delta_l. \tag{2.22}$$

This approach is naturally only useful when a small number of partial waves contribute to the scattering, which is indeed the case at low energies. This can be argued by considering the centrifugal barrier $\sim l(l+1)/r^2$ which becomes difficult to overcome with increasing l. A low energy particle cannot overcome this barrier to see the actual interatomic potential. Thus, only the $l = 0$ scattering is significant for atoms at ultracold temperatures. This type of scattering is referred to as s-wave scattering, following the naming of atomic orbitals.

With only s-wave scattering being important, $f(\theta)$ loses its angular dependence and can be expressed as a constant $-a$ which is referred to as the scattering length. For $k \to 0$, Eq. (2.17) can now be written as

$$\psi(r) = 1 - \frac{a}{r}, \tag{2.23}$$

and a thus provides the interception of the wave function on the r axis as shown in Fig. 2.1. Note that this is for large r. The actual wave function oscillates rapidly in the presence of the attractive van der Waals potential.

More formally, a can also be defined as

$$a = -\lim_{k\to 0} \frac{\tan\delta_0}{k} \tag{2.24}$$

from which $f = -\lim_{k\to 0} a$ can be derived.

The total cross section can now also be calculated

$$\sigma = \sigma_0 = 4\pi a^2. \tag{2.25}$$

The scattering between two particles can thus be described by a single parameter a of dimensionality length, which can be interpreted as the distance at which two particles see each other in a scattering event.

It is possible to calculate scattering lengths of simple interatomic trial potentials, as outlined in the following, where a hard core potential with a van der Waals tail r^{-6} is examined. The value of the scattering length oscillates as the radius of the hard core is increased, in a manner similar to a mathematical tangent function. The oscillatory behavior is connected to the disappearance of bound states as the potential gets more shallow. As the radius is increased and a bound state of the attractive potential is about to disappear into the continuum, the interaction strength increases towards $+\infty$. As the radius is increased further, the strength increases from $-\infty$, towards 0, and increases again towards $+\infty$ when a new bound state approaches the continuum. Thus, the value of the scattering length a can in principle take on any value from $-\infty$ to $+\infty$ and it depends sensitively on the exact potential, since a bound state near the continuum has a strong influence.

It is not possible to make precise predictions of the scattering length for large atoms from theory alone. Instead, a Lennard-Jones type potential can be employed including a number of C coefficients, which can be determined experimentally. From such a potential, the scattering length can be calculated.

It is possible to extend the use of the scattering length to a many-body context. By using the Born approximation to first order, the scattering length can by calculated as

$$a = \frac{m_{\mathrm{r}}}{2\pi\hbar^2}\int \mathrm{d}\mathbf{r}U(\mathbf{r}), \tag{2.26}$$

where $U(\mathbf{r})$ is an arbitrary interatomic potential. This expression shows that the interaction can be described by an effective interaction

$$\int \mathrm{d}\mathbf{r}U(\mathbf{r}) = \frac{2\pi\hbar^2 a}{m_{\mathrm{r}}} \equiv g. \tag{2.27}$$

In this manner, the interactions of a physical system of many particles which have a complicated dependence on the interparticle separations and potentials, can be effectively described by a single parameter g proportional to the scattering length. It is now also clear that the sign of a directly determines whether the nature of an interaction is attractive or repulsive.

The physical size of systems are on the order of several μm, much larger than typical scattering lengths. Therefore, the interaction between two particles at positions $\mathbf{r}$ and $\mathbf{r}'$ can be described by a contact form

$$U(\mathbf{r},\mathbf{r}') = g\delta(\mathbf{r}-\mathbf{r}'), \tag{2.28}$$

where δ is the Dirac delta function. This effective interaction is highly useful when including interatomic interactions to the description of a Bose-Einstein condensate.

2.2.3 Three-Body Recombination

Until now, elastic two-body scattering was discussed. Depending on the exact states of the atoms, two-body inelastic scattering is often not allowed due to conservation of energy, momentum and spin. However, when three atoms collide, it is possible for two of the atoms to form a deeply bound molecule where the excess energy is converted into kinetic energy. This energy is typically large enough for the involved atoms to leave the trap in which they are held. This process, denoted three-body recombination, thus results in atom loss.

As obtained from the scattering cross section Eq. (2.25), the probability of two atoms colliding is proportional to a^2. The probability of one more atom entering the collisional process adds another factor a^2, and three-body recombination is thus proportional to a^4. In a similar manner, the probability of two atoms colliding is proportional to the density n and the probability of a three-body process is proportional to n^2.

Assuming all three atoms are lost, the general three-body recombination rate is

$$L_3 = C\frac{3\hbar}{m}a^4, \tag{2.29}$$

where C is a dimensionless factor depending on the system [49]. The resulting loss rate is

$$\frac{\dot{N}}{N} = L_3 n^2. \tag{2.30}$$

In most experimental systems the atom density is inhomogeneous due to a trapping potential, which have to be taken into account to understand the losses. In a harmonic trap, the density is larger in the center of the trap. Additionally, atoms found in the center are more likely to have a lower energy. Three-body losses thus preferentially remove atoms of low energy from a harmonic trap, also resulting in heating of the system. This heating process is opposite to evaporative cooling, where the most energetic atoms are removed to cool a system. Three-body losses are discussed in more detail in Chapter 5.

2.3 Feshbach Resonances

A Feshbach resonance is a scattering phenomenon which can be utilized to tune the scattering length a to arbitrary values. The first observation of a Feshbach resonance in an ultracold gas was performed in a gas of sodium atoms [50]. Since then, the ability to choose the interaction strength of your system at will has made Feshbach resonances a central tool in the field of ultracold gases [8].

When ultracold atoms scatter, the only internal states of relevance are the hyperfine states of the atoms. The presence of multiple hyperfine states results in different scattering channels as shown schematically in Fig. 2.2(a). Here an atom is scattering in the open channel, with vanishing kinetic energy due to low temperature. If a bound state of a closed channel is near the scattering continuum, it couples to the scattering state, changing the scattering phase and scattering length. This is especially interesting when the open and closed channels have different magnetic moments. If so, the position of the bound states in the closed channel can be shifted relative to the open channel, allowing the scattering length to be tuned by changing the magnetic field. As a result, a magnetic scattering resonance is formed: a Feshbach resonance [8].

In the vicinity of a Feshbach resonance the scattering length can be expressed as a function of the magnetic field

$$a(B) = a_{\mathrm{bg}}\left(1 - \frac{\Delta_{\mathrm{F}}}{B - B_0}\right), \tag{2.31}$$

where B is the magnetic field [8]. The Feshbach resonance is characterized by three parameters; the width Δ_{F}, the position B_0, and the background scattering length a_{bg} which describes the interaction strength far away from the resonance. In Fig. 2.2(b), a plot of Eq. (2.31) is shown, which displays how the scattering length can be tuned by control of the magnetic field. The precision of the magnetic field limits the precision with which the interaction can be tuned, especially near the resonance position B_0 where the scattering length diverges. Here the three-body recombination rate is also greatly enhanced due to the a^4 dependence of Eq. (2.29).

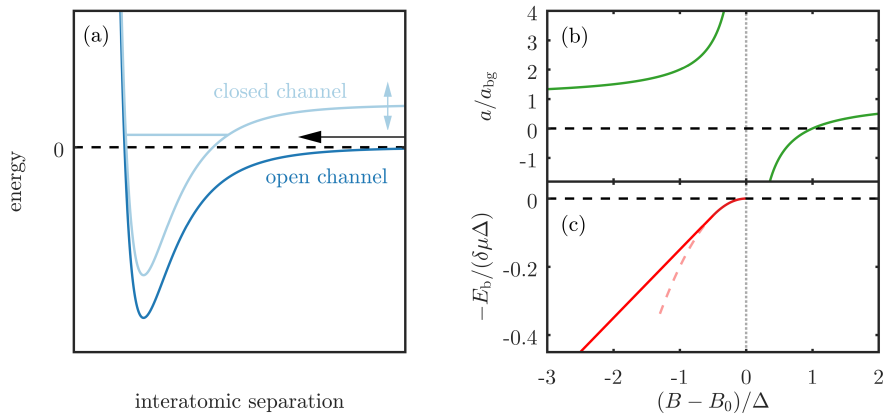

Figure 2.2: Schematic overview of a Feshbach resonance. (a) The scattering of atoms in an open channel can be affected by the presence of a bound state in a closed channel, if the state is close to the continuum, which creates a Feshbach resonance. (b) The scattering length in the vicinity of the Feshbach resonance. (c) The bound molecular state in the closed channel couples to the continuum. The energy of this state is shown as a solid red line and the dashed light red line show universal behavior $E_{\mathrm{b}} = \hbar^2/2m_{\mathrm{r}}a^2$ near the resonance center.

In Fig. 2.2(c) the binding energy of the bound molecular state which causes the Feshbach resonance is shown. At the resonance center it couples to the scattering state, creating an avoided crossing with the continuum, which results in a binding energy of

$$E_{\mathrm{b}} = \frac{\hbar^2}{2m_{\mathrm{r}}a^2}. \tag{2.32}$$

The scattering length is related to the binding energy, independent of details of the interatomic potential. Additionally, it is clear that a Feshbach resonance can be utilized to tune the interaction range far beyond the characteristic size of an interatomic potential R_{vdW}. In this regime interactions become independent of the details of the potentials and acquire a universal character. Consequently, the physical phenomena arising in such a system can be applied to many different systems in nature. In general, the extent of universal region is dependent on the width of a

resonance. A broad resonance $\Delta_F \gg 1\,\mathrm{G}$ has a relatively large universal region, whereas a narrow resonance $\Delta_F \ll 1\,\mathrm{G}$ does not [8].

The avoided crossing between the molecular state and the scattering state can also be utilized to create bound molecules. By performing a rapid adiabatic sweep of the magnetic field across a Feshbach resonance, from negative to postive interactions, pairs of atoms can enter the weakly bound molecular state [8, 51]. The approximate size of such a molecule is set by the scattering length.

As explained above, the scattering length diverges when a molecular state of a closed channel approaches the scattering continuum. It is worth noting that this behavior is similar, as when considering the influence of bound states in the open channel. As discussed in Sec. 2.2, an interatomic potential having a bound state which approaches the continuum results in a divergence of the scattering length. The divergence of the scattering length due to a Feshbach resonance is similar, the bound state is merely in a different channel.

At the exact center of the Feshbach resonance, the scattering length diverges towards infinity, which is known as the unitary regime. The origin of this name is the $\sin^2\delta_0$ term in the partial wave cross section Eq. (2.22), which reaches its maximum value of unity. The scattering length a is here no longer the relevant length scale of interactions. Instead, it is replaced by the de Broglie wavelength Eq. (2.2) in a thermal gas, or the interparticle spacing $n^{1/3}$ in a condensed gas [52].

2.4 Interactions in the Condensed State

In Sec. 2.1, the statistical origin of Bose-Einstein condensation of non-interacting bosons was presented, followed by an introduction to the interactions of ultracold gases in Sec. 2.2. In this section, the impact of interatomic interactions on the Bose-Einstein condensate is introduced. The Gross-Pitaevskii equation is derived, based on reference [41]. This equation is similar to the Schrödinger equation, but describes the condensed state including interactions. The equation is extended to two-component Bose-Einstein condensates, which is relevant for the studies of dual-species Bose-Einstein condensates presented in Chapter 4.

2.4.1 The Gross-Pitaevskii Equation

To derive the Gross-Pitaevskii equation, a fully condensed Bose gas of N particles at $T = 0$ is considered. The resulting physics is however often also valid for the condensed fraction of a partially condensed ensemble with $T \neq 0$.

It is assumed that all particles are in the same single-particle state which has the usual normalization

$$\int \mathrm{d}\mathbf{r}|\phi(\mathbf{r})|^2 = 1, \tag{2.33}$$

and that the wave function is a symmetrized product of single-particle wave functions

$$\Psi(\mathbf{r}_1, \mathbf{r}_2, ..., \mathbf{r}_N) = \prod_{i=1}^{N} \phi(\mathbf{r}_i). \tag{2.34}$$

Interactions are included by a mean-field approach, which use the effective contact interaction $g\delta(\mathbf{r} - \mathbf{r}')$, where $g = 4\pi\hbar^2 a/m$. The resulting Hamiltonian is

$$H = \sum_{i=1}^{N} \left[\frac{\mathbf{p}_i^2}{2m} + V_{\mathrm{ext}}(\mathbf{r}_i) \right] + g \sum_{i<j} \delta(\mathbf{r}_i - \mathbf{r}_j), \tag{2.35}$$

where $V(\mathbf{r})_{\mathrm{ext}}$ is an external potential. The corresponding energy of the state of Eq. (2.34) is

$$E = N \int \mathrm{d}\mathbf{r} \left[\frac{\hbar^2}{2m} |\nabla\phi(\mathbf{r})|^2 + V_{\mathrm{ext}}(\mathbf{r})|\phi(\mathbf{r})|^2 + \frac{N-1}{2} g|\phi(\mathbf{r})|^4 \right]. \tag{2.36}$$

For a large number of particles, the local interaction energy is well approximated by

$$\frac{N(N-1)}{2V} g \approx \frac{1}{2} V n^2 g, \tag{2.37}$$

where n is the density $n = N/V$. It is convenient to include the density in the wave function and thereby introduce the concept of the wave function of the condensed state

$$\psi(\mathbf{r}) = N^{1/2}\phi(\mathbf{r}), \qquad n(\mathbf{r}) = |\psi(\mathbf{r})|^2, \qquad N = \int \mathrm{d}\mathbf{r}|\psi(\mathbf{r})|^2. \tag{2.38}$$

With this, the energy described by Eq. (2.36), can be expressed as

$$E(\psi) = \int \mathrm{d}\mathbf{r} \left[\frac{\hbar^2}{2m} |\nabla\psi(\mathbf{r})|^2 + V_{\mathrm{ext}}(\mathbf{r})|\psi(\mathbf{r})|^2 + \frac{1}{2} g|\psi(\mathbf{r})|^4 \right], \tag{2.39}$$

for $N \gg 1$. To arrive at the Gross-Pitaevskii equation, this energy is minimized with respect to variations of $\psi(\mathbf{r})$ and its complex conjugate $\psi^*(\mathbf{r})$, by the method of Lagrange multipliers. The constraint $\delta E - \mu\delta N = 0$, where μ is the chemical potential, ensures that the number of particles is conserved. After some calculations, this provides

$$\mu\psi(\mathbf{r}) = \left[-\frac{\hbar^2}{2m}\nabla^2 + V_{\mathrm{ext}}(\mathbf{r}) + g|\psi(\mathbf{r})|^2 \right] \psi(\mathbf{r}), \tag{2.40}$$

which is the time-independent Gross-Pitaevskii equation. It is useful for both numerical and analytical calculations of condenstate properties, including ground state and dynamical behavior.

In a harmonic trap, the strength of the interaction can be parameterized by the dimensionless quantity Na/a_{osc}, where $a_{\mathrm{osc}} = \sqrt{\hbar/m\bar{\omega}}$ is the oscillator length. In many contexts a and N are thus equivalent.

If a is negative, the interaction will tend to shrink the condensate wave function spatially. This is counteracted by the kinetic energy term which tries to increase the size of the condensate. For sufficiently attractive interactions the kinetic energy can, however, not prevent a collapse of the wave function towards a singularity. For a spherical trap [34] the critical lower bound of a stable condensate is

$$\left(\frac{Na}{a_{\mathrm{osc}}} \right)_{\mathrm{crit}} = -0.575. \tag{2.41}$$

Collapsing condensates have been observed experimentally by preparing a condensate at repulsive interactions, and subsequently changing the interactions to be negative via a Feshbach resonance [35, 53–57], a phenomenon known as a Bose nova. As the condensate contracts, the density increases rapidly and atoms are lost due to three-body recombination. The remaining number of atoms after the losses is approximately provided by Eq. (2.41).

To produce large, stable condensates, it is therefore required that the atoms of the condensate have $a \geq 0$. This fact is crucial to the experimental procedure which will be introduced in Chapter 3, where ^{39}K has a negative background scattering length, making Feshbach resonances a necessary tool for producing Bose-Einstein condensates.

For $Na/a_{\text{osc}} \gg 1$ it is possible to apply the Thomas-Fermi approximation which neglects the kinetic energy by simply removing the Laplacian term. By doing so, one can easily obtain information about the condensate ground state [34], e. g. radius

$$R_i^2 = 2\mu/m\omega_i^2, \qquad i = x, y, z, \tag{2.42}$$

chemical potential

$$\frac{\mu}{\hbar\bar{\omega}} = \frac{15^{2/5}}{15}\left(\frac{Na}{a_{\text{osc}}}\right)^{2/5}, \tag{2.43}$$

and energy per particle

$$\frac{E}{N} = \frac{5}{7}\mu. \tag{2.44}$$

It is thus possible to describe properties of an interacting many-body quantum state—the Bose-Einstein condensate—through relatively simple means.

2.4.2 Two-Component Bose-Einstein Condensates

The framework of the Gross-Pitaevskii equation can be extended to describe Bose-Einstein condensates of two components

$$\begin{aligned}
\mu_1\psi_1(\mathbf{r}) &= \left[-\frac{\hbar^2}{2m_1}\nabla^2 + V_{\text{ext},1}(\mathbf{r}) + g_{11}|\psi_1(\mathbf{r})|^2 + g_{12}|\psi_2(\mathbf{r})|^2\right]\psi_1(\mathbf{r}),\\
\mu_2\psi_2(\mathbf{r}) &= \left[-\frac{\hbar^2}{2m_2}\nabla^2 + V_{\text{ext},2}(\mathbf{r}) + g_{22}|\psi_2(\mathbf{r})|^2 + g_{12}|\psi_1(\mathbf{r})|^2\right]\psi_2(\mathbf{r}),
\end{aligned} \tag{2.45}$$

where 1 and 2 refer to the two components [41]. The two components, are thus described by a set of equations, coupled by the interactions $g_{ij} = 2\pi\hbar^2 a_{ij}/m_{ij}$, where $m_{ij} = m_i m_j/(m_i + m_j)$ and a_{ij} is the scattering length between atoms of components i and j.

One interesting property to study is the stability of two overlapping Bose-Einstein condensates determined by their interactions. With the prospect of utilizing Feshbach resonances, this stability can be studied systematically.

Within the Thomas-Fermi approximation it has been shown that the stability can be expressed through a simple relation between the interactions

$$\Delta_{\text{stab}} = \frac{g_{11}g_{22}}{g_{12}^2} - 1, \tag{2.46}$$

where g_{11} and g_{22} are typically positive [58, 59]. In the interval $\Delta_{\text{stab}} > 0$ the two condensates can overlap spatially. If however $\Delta_{\text{stab}} < 0$, the two condensates cannot stably coexists in the same region of space.

When $\Delta_{\text{stab}} < 0$ and $g_{12} < 0$, the attractive interactions between the two condensates overcome the repulsive potential of the seperate condensates, resulting in a collapse similar to that of a single component Bose nova.

If however $\Delta_{\text{stab}} < 0$ and $g_{12} > 0$, a new phenomenon emerges. The repulsion between the two condensates is so large that the two condensates phase separate spatially, with an interface segregating them. In this state, the condensates are described as immiscible, whereas two condensates with interactions $\Delta_{\text{stab}} > 0$ are said to be miscible.

The phase separation and density profiles of two-component condensates have been studied both theoretically [58–74] and experimentally [75–78]. However, experimental imaging of atoms have a limited spacial resolution, which typically hinders the observation of separation in situ. Instead, the two components are released from their trap and imaged after some duration of time-of-flight expansion. The miscibility of two-component condensates is thus often analyzed based on data aquired after a dynamical expansion and not by an investigation of the ground state.

In Chapter 4, the time-of-flight expansion of two-component condensates are studied. Here, one central aim is to discuss the validity of using data acquired after time-of-flight to determine the miscibility of the condensates. Additionally, it is debated whether the criterion set by

Eq. (2.46) is a meaningful property of two-component condensates at all.

2.5 Efimov Physics in Ultracold Gases

In 1970, V. Efimov predicted that three identical spinless particles interacting via two-body forces could produce a series of three-body bound states, where no two-body bound state exists [29]. The theoretical prediction was initially made in context of nuclear physics, e. g. three α-particles of a ^{12}C nucleus, but detection in nuclei has failed so far [79].

Efimov physics is a central example of the universality of low-energy physics, since the properties of Efimov states are independent of many microscopic details of a given system. Consequently, Efimov physics can be applied to a wide range of fields [10].

In 2006, the first observation of Efimov states was made in an ultracold gas of cesium atoms [80]. This initiated a strong interest to the field of few-body and Efimov physics in context of ultracold gases which is covered in several reviews [10, 81–85]. These reviews are the basis for the introduction to Efimov physics given in the following. Furthermore, an overview of the experimental accomplishments of the field is provided. This serves as introduction and perspective to the experimental studies of Efimov physics presented in Chapter 5.

What makes ultracold gases especially suitable for studying Efimov physics is the prospect of employing Feshbach resonances to tune the interatomic interaction. The presence of an Efimov state at a given interaction manifests as a change of the three-body recombination rate L_3. To study Efimov physics in an atomic gas, ultracold temperatures are required, but the gas does not need to be condensed.

The origin of Efimov physics is an attractive three-body force, arising from the two-body forces between three particles. The appearance of Efimov states near a Feshbach resonance is shown in Fig. 2.3(a). The first Efimov state appears at a negative scattering length a_-, and extends across the Feshbach resonance to a positive scattering length a_*, where it connects with the molecular dimer state. The next Efimov state exists inwards at stronger interactions relative to the first and has a similar

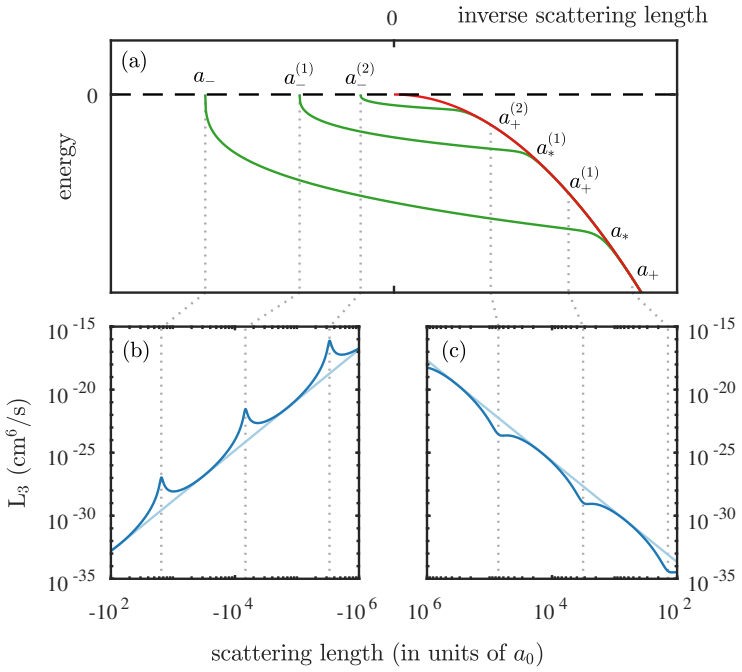

Figure 2.3: Efimov states in the vicinity of a Feshbach resonance. (a) The nested structure of Efimov states is shown as green lines and the molecular state as a red line. The manifestation of Efimov states in the recombination rate is shown at various interaction strengths for negative a in (b) and positive a in (c). The recombination rate in absence of Efimov states, plotted in light blue, increases regularly proportional to a^4 towards the center of the Feshbach resonance. In the presence of Efimov states, a periodic modulation of the recombination rate appears, as shown in dark blue.

structure across the Feshbach resonance, appearing and disappearing at interactions $a_-^{(1)}$ and $a_*^{(1)}$. This nested structure of states continues indefinitely.

The alteration of three-body recombination coefficient L_3 due to the presence of Efimov states is shown in Fig. 2.3(b-c). If an Efimov trimer state has the same energy as three unbound atoms, a strong coupling occurs which opens up additional decay paths. If a sample of atoms is held at an interaction $a_-^{(n)}$, the three-body recombination is therefore in-

creased, compared to if no Efimov state is present. Such a loss resonance is referred to as an Efimov resonance.

Similarly to three atoms, an atom and a dimer will undergo enhanced recombination at interactions $a_*^{(n)}$. Additionally, the three-body recombination coefficient has regions of reduced recombination for attractive interactions, which are labeled by $a_+^{(n)}$. These minima of L_3 are due to a destructive interference between two different decay paths in the atom-dimer channel [86, 87].

The interactions at which the Efimov states appear are linked by a universal scaling law

$$\mathrm{e}^{\pi/s_0} = \frac{a_-^{(n+1)}}{a_-^{(n)}} = \frac{a_+^{(n+1)}}{a_+^{(n)}} = \frac{a_*^{(n+1)}}{a_*^{(n)}} \approx 22.7, \tag{2.47}$$

where $s_0 \approx 1.00624$ describes the scaling which, together with the position of the first resonance a_-, dictate the properties of all the trimer states. The position of the first Efimov resonance a_- is also known as the three-body parameter, as it indicates at what interactions three-body physics become important. Compared to a_-, the first atom-dimer resonance appears at $a_-^{(n)}/a_*^{(n+1)} \approx -1.06$ and the first recombination minimum at $a_-^{(n)}/a_+^{(n+1)} \approx -22.7/4.9$. The size of an Efimov trimer is given approximately by the scattering length at which it appears. Its binding energy is on the order of the dimer binding energy, and scales with $\mathrm{e}^{-2\pi/s_0} \approx 1/515$ at $1/a = 0$.

The three-body recombination in presence of Efimov states can be expressed together with Eq. (2.29) as

$$C(a) = 4590 \frac{\sinh(2\eta_-)}{\sin^2\left[s_0 \ln\left(a/a_-\right)\right] + \sinh^2\eta_-} \qquad \text{if } a < 0 \tag{2.48}$$

$$C(a) = 67.1\mathrm{e}^{-2\eta_+}\left(\sin^2\left[s_0\ln\left(a/a_+\right)\right] + \sinh^2\eta_+\right) + 16.8\left(1-\mathrm{e}^{-4\eta_+}\right) \qquad \text{if } a > 0, \tag{2.49}$$

where $\eta_\pm$ is the elasticity parameter which describes the width of a resonance and is connected with the lifetime of the trimer state [81, 84]. These expressions are used to calculate L_3 in Fig. 2.3(b-c), with $\eta_\pm = 0.05$, $a_- = 650a_0$, and $a_+ = -4.5a_-$. The three-body recombination rate in the absence of Efimov states is plotted by setting the $\sin^2$-terms to 1.

In theory, the nested Efimov states continue indefinitely, but in practice, various constraints limit the region of interactions where Efimov physics can be studied. The lower limit of this window is when the interaction range is comparable to the van der Waals radius $|a| \sim R_{\mathrm{vdW}}$. Here, the scattering starts to depend sensitively on the details of the interatomic potentials, and universality and Efimov physics is lost.

Several different mechanisms introduce upper limits of the interaction strength. The typical limit is the temperature, which defines the extension of atomic wave functions through the de Broglie wavelength given by Eq. (2.2). No matter the value of $|a|$, atoms which interact by contact interactions do not see each other at a distance $|a|$ if their wave functions do not overlap [88]. Another upper limitation is the physical size of the system which must necessarily be larger than $|a|$. Finally, a finite resolution of the magnetic field can limit the resolution of $|a|$ at strong interactions.

2.5.1 Studies of Homonuclear Efimov Physics

Efimov resonances have presently been observed within several different atomic species [80, 89–92], including Fermi spin mixtures of three components [93, 94], and universality has been confirmed across different Feshbach resonances [95–98]. Remarkably, the value of the three-body parameter a_- is universally determined by the van der Waals radius of a given species as $R_{\mathrm{vdW}}/a_- \approx 9.7$, except for very narrow resonances [98, 99]. The physical interpretation of this relation is that a decrease in the two-body interactions at R_{vdW} results in an effective barrier in the three-body potential at a similar distance, which prevents the particles from seeing the nonuniversal potentials at short distances [99–102].

Furthermore, the universal scaling of approximately 22.7 has been studied by observation of the second Efimov resonance [103] and by observation of multiple recombination minima [89, 90]. Evidence of an excited-state trimer has also been observed in a three-component Fermi gas [104]. Moreover, the atom-dimer recombination resonance has been observed [105–107] and trimers have been associated directly by using radio frequency radiation [108–110]. Very recently, Efimov trimers were associated by sweeping the magnetic field away from a resonantly interacting Bose gas, in a manner similar to association of molecules by sweeping across a Feshbach resonance [111].

Additional studies include the observations of four- [112] and five-body [113] states associated with the three-body Efimov states and of the impact of temperature on an Efimov resonance [114].

Recently, the first unambiguous experimental observation of Efimov physics outside the field of ultracold gases was made in a beam of He by Coulomb explosion imaging of the trimer states [115].

2.5.2 Heteronuclear Efimov Physics

The original theoretical work by Efimov involved three identical spinless particles [29]. If one of these is exchanged with a new particle, the properties of the Efimov states are changed dramatically, depending on the properties of the new particle and its interaction with the others. This scenario is relevant for two-neutron halo nuclei such as ^{11}Li, where two neutrons orbit the core nucleus [10, 79].

Systems of different particles are more complicated to describe than systems of identical particles, but can potentially provide a richer spectrum of Efimov states. When exchanging one of the identical bosons of mass m_1 with a new particle of mass m_2, new aspects have to be taken into account, which influence a_- and s_0.

The relative mass m_1/m_2 influences the scaling s_0. A system of two heavy particles and one light is considered "Efimov-favoured", since the scaling $a_-^{(n+1)}/a_-^{(n)}$ decreases, which allows for easier detection of multiple resonances. The opposite is the case for two light and one heavy particle, where the scaling increases [116].

Furthermore, the tunability of the interactions is generally restricted to the interactions between the two different types of particles, whereas the interaction between the identical particles remains constant and relatively low. This also results in an increased scaling factor [116].

The value of a_-, the three-body parameter, is still universal, but the physical origin of the universality is different, depending on whether the system is Efimov-favoured or not [98, 116]. As a consequence a_- can not be expressed as a trivial function of R_{vdW} [116]. Except for heavily mass-imbalanced systems, a_- is generally not experimentally accessible.

Heteronuclear Efimov resonances have been observed in mixtures of ^{41}K^{87}Rb [117], ^{6}Li^{133}Cs [118, 119], and ^{6}Li^{87}Rb [120] and atom-dimer recombination maxima has been observed in mixtures of ^{40}K^{87}Rb [121] and ^{41}K^{87}Rb [122].

The ^{6}Li^{133}Cs system has proved very rewarding to study. Due to the mass imbalance, up to three consecutive Efimov resonances have been observed [119], the effect of the interaction between the identical bosons has been studied [123, 124], and the universality across Feshbach resonances has been shown experimentally [98, 125, 126].

The first observation of a heteronuclear Efimov resonance was performed in a ^{41}K^{87}Rb system [117], but these results have been heavily debated [116, 121, 127]. This controversy motivated the study of three-body physics in KRb mixtures presented in Chapter 5, and will be discussed in more detail there.

2.6 Polarons in Ultracold Gases

The scenario of a mobile impurity interacting with its surroundings is central in physics. A key example is an electron moving in a crystal lattice. The charge of the electron can displace nearby ions to create a local polarization of the lattice as shown in Fig. 2.4. In other terms, the electron is dressed by lattice phonons. This composition of an impurity particle interacting with excitations of the surrounding medium is best described in terms of a quasiparticle, denoted a polaron [19, 20]. This concept is important in understanding various exotic materials [21, 22] and semiconductors of technological importance [23]. However, the

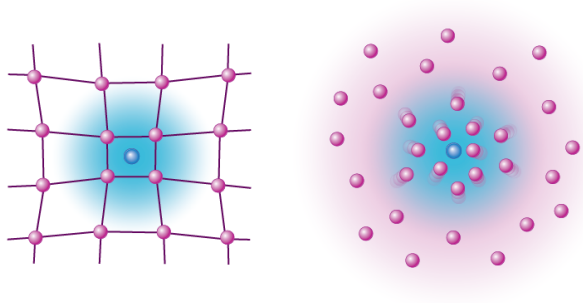

Figure 2.4: Polarons in solid-state physics and ultracold quantum gases. In solid-state physics, a moving electron can perturb the surrounding lattice to form a quasiparticle called a polaron, which is shown artistically to the left. In a similar manner, an impurity in an ultracold gas can perturb the surrounding medium to form the same quasiparticle, as shown to the right. The image is reprinted with permission from reference [132]. Credit: APS/Carin Cain.

picture of an impurity immersed in an interacting medium is found in diverse areas of physics, such as superfluid ^{3}He-^{4}He mixtures [128], Λ-baryons in nuclear matter [129], and high-temperature superconductors [130]. Even elementary particles acquire their mass through coupling to a medium of Higgs bosons [131].

Being able to understand the general properties of an impurity interacting with its surroundings is therefore highly desirable. The field of ultracold quantum gases provide an excellent setting to do so, given the capability to tune interactions, the high degree of purity and the flexibility of dimensionality and traps.

The first observation of a polaron in an ultracold gas was made in 2009 in a ^{6}Li Fermi gas [11]. Since then additional studies have been conducted, altogether providing new insights to the interacting impurity. Despite immense theoretical interest, a polaron in a Bose-Einstein condensate had not yet been observed until very recently.

Within this thesis, the first observation of a polaron in a Bose Einstein condensate—the Bose polaron—is reported. The result is covered in Chapter 6 and was published in parallel with a similar study from JILA [17, 133].

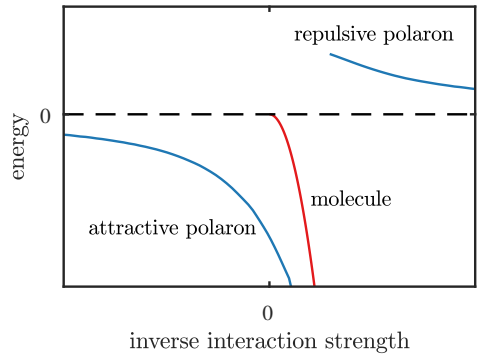

Figure 2.5: Two polaron branches in the vicinity of a Feshbach resonance. At attractive interactions an attractive polaron branch exists, extending across unitarity and approaching the molecular state. At repulsive interactions a repulsive branch exists, which becomes increasingly damped when approaching strong interactions, due to the presence of lower-lying states.

In the remainder of this section, a short introduction to polarons in ultracold gases is given. This includes an overview of the important results from literature. The properties unique to the Bose polaron will be discussed and, finally, various theoretical models for describing the polaron will be introduced.

The typical method to study polarons in ultracold gases is to perform spectroscopy in an ultracold mixture of two components. One component serves as medium and the other as impurities. The impurities must necessarily have a significantly lower relative density. The impurity component is initially prepared in a state which is weakly or non-interacting with the majority component. To perform spectroscopy, a pulse transfers the impurities into a state which interacts strongly with the medium, typically through a Feshbach resonance. The interaction changes the energy of the impurities, which is measured by comparing the transition energy of the spectroscopy with the bare transition. Research on polarons in ultracold gases thus typically revolves around, but is not restricted to, studying the energy of the impurities.

A generic energy diagram of an impurity interacting with a medium through a Feshbach resonance is shown schematically in Fig. 2.5. Two

branches exist: the repulsive polaron at repulsive interactions, and the attractive polaron at attractive interactions.

At weak interactions, the polaron energy is well described by mean-field theory $E = 2\pi\hbar^2 an/m_\mathrm{r}$, where n is the density of the medium, a refers to the impurity-medium scattering length, and m_r is the impurity-medium reduced mass. Near the Feshbach resonance center, a mean-field description is however no longer valid. The strong interaction perturbs the surrounding medium, either repelling or attracting the particles of the medium, depending on the branch. The relation between interaction strength and energy therefore becomes non-trivial and various theoretical methods are used to determine the characteristics of the strongly interacting polaron.

A remarkable feature of the attractive polaron branch is its extension across unitarity where it approaches the molecular branch. This behavior can be understood by a qualitative argument; the extreme case of an impurity attracting the surrounding atoms is indeed a molecule, where one medium atom is bound to the impurity.

The energy of the repulsive polaron branch increases as strong interactions are approached. However, near unitarity the polaron state becomes increasingly unstable, since it can decay to lower-lying states. As a consequence, the repulsive polaron becomes increasingly damped at strong interactions.

Some other interesting properties of the polaron is its effective mass which changes due to the coupling with the medium and its quasiparticle residue Z. The quasiparticle residue is a measure of how much of the non-interacting particle state $|\psi_\mathrm{N\text{-}I}\rangle$ is contained in the polaron state $|\psi_\mathrm{pol}\rangle$, which can be quantified as $\sqrt{Z} = \langle\psi_\mathrm{N\text{-}I}|\psi_\mathrm{pol}\rangle$. The residue can thus take on values between 0 and 1 and can be obtained directly from the Rabi frequency when driving a transition between the two states. The remaining spectral weight lies in excitations of the medium, at higher energies than the polaron.

2.6.1 Studies of Polaron Physics in Ultracold Gases

Fermi polarons have been investigated experimentally in several studies since the first observation in 2009 [11]. Initially, only an attractive po-

laron branch was believed to exist [134–136], which was also the subject of this first observation.

The repulsive polaron was later hypothesized [137–140] and experimentally observed in two parallel studies [13, 14]. Here, the stability and quasiparticle residue of repulsive polarons were measured [13] and the energy-momentum excitation spectrum of polarons in two dimensions was observed [14].

The decoherence of impurities has also been determined using spin-echo [141] and the ultrafast dynamics of the impurities were studied by rapidly tuning interactions [15]. Furthermore, the effective mass of polarons was measured by studying collective excitations of an imbalanced Fermi gas [142] and by utilizing in situ imaging of a Fermi gas of two-components to determine its equation of state [12]. Remarkably, a negative effective mass of repulsive polarons was recently observed [16].

2.6.2 The Bose Polaron

The experimental progress on the Fermi polaron led to an immense theoretical interest in the bosonic counterpart, e. g. see references [143–149]. Several studies of impurities in bosonic gases had been performed, including charged impurities [150–152], fixed impurites [153, 154], and impurities interacting with an uncondensed bosonic medium [155], but no study of the generic polaron in a Bose-Einstein condensate.

The Bose polaron has several remarkable features, compared to the Fermi polaron. The bosonic medium allows the impurity to interact with several medium particles simultaneously, thus introducing three- and higher-body interactions. Intriguingly, the three-body interactions grant Efimov physics to influence the properties of the Bose polaron [10, 144, 148, 156–160]. However, the involvement of three-body interactions represent an obstacle since strongly interacting impurities are expected to be lost rapidly to three-body recombination.

Similarly to the Efimov physics discussed in Sec. (2.5), the Efimov effect is most prominent for polarons when considering a light impurity interacting with two heavy medium particles [148, 158, 159]. However, a very recent theoretical study showed that even for particles of equal mass, the three-body parameter a_- can affect the behavior of the po-

laron, even at densities where no well-defined Efimov states exist. It is furthermore argued that the polaron energy at unitarity is a universal function of $|a_-|n^{1/3}$ [160].

In general the possibility to interact with multiple medium particles simultaneously makes for a stronger parallel with solid-state physics. Like the phonons in a solid, the medium for the Bose polaron is bosonic. Furthermore, the dispersion properties of the media are similar. For low energies, the dispersion relation of Bogoliubov modes in a Bose-Einstein condensate is linear [41], similar to the dispersion relation of phonons in most solids. This establishes an impurity in a Bose-Einstein condensate as a capable quantum simulator of solid-state systems.

Very recent theoretical studies have also revealed an intriguing non-monotonic energy dependence on temperature. The origin is the Bose-Einstein condensate phase transition at T_c, which dramatically changes the density of states of the medium particles, affecting the scattering of the impurity [161, 162].

2.6.3 Theoretical Descriptions of the Bose Polaron

The Bose polaron has been studied through several different theoretical approaches, some of which will be outlined in this section. Typically, a single impurity in a weakly interacting Bose-Einstein condensate is considered. The condensate is weakly interacting in the sense that $na_B^3 \ll 1$, where a_B is the scattering length amongst the bosons of the Bose-Einstein condensate.

To obtain a correct description it is necessary to take into account the quantum nature of excitations in the Bose medium. It is thus useful to describe the system by second-quantized notation. The full Hamiltonian of this system is

$$\begin{aligned}\hat{H} = &\sum_{\mathbf{p}} \Omega_{\mathbf{p}} \hat{c}^{\dagger}_{\mathbf{p}} \hat{c}_{\mathbf{p}} + \sum_{\mathbf{p}} \epsilon_{\mathbf{p}} \hat{b}^{\dagger}_{\mathbf{p}} \hat{b}_{\mathbf{p}} \\ &+ \frac{1}{2V} \sum_{\mathbf{p},\mathbf{p}',\mathbf{q}} V_B(\mathbf{q}) \hat{b}^{\dagger}_{\mathbf{p}+\mathbf{q}} \hat{b}^{\dagger}_{\mathbf{p}'-\mathbf{q}} \hat{b}_{\mathbf{p}'} \hat{b}_{\mathbf{p}} \\ &+ \frac{1}{V} \sum_{\mathbf{p},\mathbf{p}',\mathbf{q}} V_I(\mathbf{q}) \hat{c}^{\dagger}_{\mathbf{p}+\mathbf{q}} \hat{b}^{\dagger}_{\mathbf{p}'-\mathbf{q}} \hat{b}_{\mathbf{p}'} \hat{c}_{\mathbf{p}}. \end{aligned} \tag{2.50}$$

Here $\hat{b}_{\mathbf{p}}$ ($\hat{b}^{\dagger}_{\mathbf{p}}$) and $\hat{c}_{\mathbf{p}}$ ($\hat{c}^{\dagger}_{\mathbf{p}}$) annihilate (create) a boson and an impurity, respectively, with kinetic energies $\epsilon_{\mathbf{p}} = \hbar^2\mathbf{p}^2/2m_{\mathrm{B}}$ and $\Omega_{\mathbf{p}} = \hbar^2\mathbf{p}^2/2m_{\mathrm{I}}$, $\mathbf{p}$ and $\mathbf{q}$ being momenta, and V is the volume of the system. The first row of the equation is the kinetic energy of the impurity with mass m_{I} and bosons with mass m_{B}, the second row is the interaction energy of the bosons, and the third row is the impurity-boson interaction energy. Both interaction potentials are expressed in terms of the Fourier transform of the two-body potentials $V_{\mathrm{B}}(\mathbf{q})$ and $V_{\mathrm{I}}(\mathbf{q})$. As discussed previously, these can be assumed to be short-ranged and can be written as $V_{\mathrm{B}}(\mathbf{q}) = g_{\mathrm{B}} = 4\pi\hbar^2 a_B/m_{\mathrm{B}}$ and $V_{\mathrm{I}}(\mathbf{q}) = g_{\mathrm{I}} = 2\pi\hbar^2 a/m_{\mathrm{r}}$, where m_{B} is the mass of medium bosons.

One approach to evaluate the Hamiltonian is to employ perturbation theory as in reference [147]. Here perturbation theory to third-order of $V_I(\mathbf{q})$ is applied to obtain analytical expressions for energy, residue, and effective mass. The resulting energy of the polaron for $\mathbf{p} = \mathbf{0}$ and $T = 0$ is

$$\frac{E}{E_0} = \frac{a}{\xi} + A(m_{\mathrm{I}}/m_{\mathrm{B}})\frac{a^2}{\xi^2} + B(m_{\mathrm{I}}/m_{\mathrm{B}})\frac{a^3}{\xi^3}\ln(a^*/\xi), \tag{2.51}$$

where $\xi = 1/\sqrt{8\pi n a_{\mathrm{B}}}$ is the condensate healing length, $E_0 = 2\pi n\xi/m_{\mathrm{r}}$, $a^* = \max(a, a_{\mathrm{B}})$, and A and B are functions of the mass ratio. For equal masses $A(1) = 8\sqrt{2}/3\pi$ and $B(1) = 2/3 - \sqrt{3}/\pi$. Similarly, the quasiparticle residue can be expressed as

$$Z^{-1} = 1 + C(m_{\mathrm{I}}/m_{\mathrm{B}})\frac{a^2}{a_{\mathrm{B}}\xi} + D(m_{\mathrm{I}}/m_{\mathrm{B}})\frac{a^3}{a_{\mathrm{B}}\xi^2}, \tag{2.52}$$

where $C(1) = 2\sqrt{2}/3\pi$ and $D(1) \approx 0.64$.

The first term of Eq. (2.51) corresponds to the first order mean-field energy, whereas the next terms are from second and third order diagrams. The pertubation theory works well for weak interactions and outlines well initial deviations from mean-field energies as stronger interactions are approached. Additionally, it is useful as a benchmark for numerical theories, which can be utilized to describe the strongly interacting regime.

One numerical approach to describe polarons at stronger interactions is variational theories [145, 148, 160, 163]. Here a trial wave function is introduced, which is expressed in terms of variational parameters of the form

$$|\Psi_{\mathbf{q}}\rangle \sim \left(\gamma_0^{(\mathbf{q})}\hat{c}_{\mathbf{p}}^{\dagger} + \sum_{\mathbf{p}} \gamma_{\mathbf{p}}^{(\mathbf{q})}\hat{c}_{\mathbf{q}-\mathbf{p}}^{\dagger}\hat{\beta}_{\mathbf{p}}^{\dagger}\right)|\mathrm{BEC}\rangle\,, \tag{2.53}$$

where $\gamma_0^{(\mathbf{q})}$ and $\gamma_{\mathbf{p}}^{(\mathbf{q})}$ are variational parameters, $\hat{\beta}_{\mathbf{p}}^{\dagger}$ creates a Bogoliubov excitation, and $|\mathrm{BEC}\rangle$ is the ground state of the Bose-Einstein condensate. The expression above includes processes with one excitation, but can be expanded to include more [148, 160, 164].

The procedure to determine the wave function and the energy is to numerically vary the variational parameters to fulfill the equation

$$\langle \partial\Psi | \left(\hat{H} - E\right) | \Psi \rangle = 0, \tag{2.54}$$

where the derivative is with respect to the variational parameters. By minimizing the energy E at each momentum $\mathbf{q}$ the dispersion relation of the Bose polaron is obtained. This additionally provides an effective mass through the relation

$$E_{\mathbf{q}} = E_{\mathbf{q}=\mathbf{0}} + \frac{\mathbf{q}^2}{2m_{\mathrm{eff}}} + \mathcal{O}(\mathbf{q}^4), \tag{2.55}$$

where m_{eff} is the effective mass. This variational approach was originally developed for Fermi polarons [163], but was since expanded to Bose polarons [145].

Another numerical approach is quantum Monte-Carlo simulations. Here, a system of a finite number of particles is fully simulated including all interactions and correlations. The method is thus numerically exact, but computationally demanding [146, 157].

In Chapter 6 both pertubation theory, quantum Monte-Carlo simulations, and a numerical method based on variational theory is employed to interpret the experimental findings.

CHAPTER 3

EXPERIMENTAL PROCEDURE AND APPARATUS

In this chapter, the apparatus used for the experimental studies of ultracold atoms within this dissertation is introduced. Since the apparatus has previously been presented in great detail [24, 165, 166] the intention in this chapter is merely to provide a concise overview of the key elements.

The first iteration of the apparatus was designed and constructed in Hannover [167, 168]. The intention was to perform experiments with multiple atomic species. Initial studies were however only performed with ^{87}Rb, which lead to the realization of a gravity compensated atom laser [169] and the observation of spin self-rephasing on the clock transition of ^{87}Rb [170], resulting in an extended coherence time of 21 s. In 2011 the apparatus was disassembled and moved to Aarhus where it was rebuilt with focus on producing ultracold degenerate mixtures of ^{39}K and ^{87}Rb. The first major result was the realization of dual-species Bose-Einstein condensates of ^{39}K and ^{87}Rb with tunable interactions in 2014 (published 2015) [24].

Dual-species Bose-Einstein condensates have previously been studied in a number of different systems [75–77, 171–174], including the ^{41}K-^{87}Rb system [175, 176]. As mentioned in Sec. 1.1, ^{39}K is not usually a good candidate for a constituent in dual-species condensates, since it has a negative background scattering length. However, the remakable Feshbach resonance structure shown in Fig. 1.1 allows the production of dual-species condensates with tunable interactions.

The remainder of this chapter is structured as follows. First, a brief overview of the apparatus is given in Sec. 3.1. In Sec. 3.2, the initial laser trapping and cooling is described, followed by magnetic trapping and cooling in Sec. 3.3, while the optical trapping and state preparation is summarized in Sec. 3.4. Finally, the precision and accuracy of the magnetic field is evaluated and discussed in Sec. 3.5.

3.1 Apparatus Overview

The apparatus presented in this chapter is capable of producing Bose-Einstein condensates of K and ^{87}Rb atoms. The atoms can be prepared in any desired hyperfine state, with precise control of the magnetic field which is used to tune various interactions. For most experimental studies, the isotope ^{39}K is used, but the apparatus can be reconfigured in a matter of hours to capture and cool ^{41}K instead.

A vacuum chamber is required to capture and control neutral atoms. By usage of magnetic fields and lasers, atoms inside the chamber can be addressed. In this experimental setup most of the laser light is prepared on one optical table, and sent via optical fibers to another optical table where the vacuum chamber is placed. Conveniently, the D_2 lines used for cooling and trapping of K and Rb have similar wavelengths, so the same optical elements can in general be used for both species.

The vacuum chamber is divided into two separate glass cells. The first is a custom made magneto-optical trap (MOT) glass cell, where both species are captured and cooled from a background vapor. Evaporative cooling and subsequent experiments are performed in the second cell, denoted the science cell. The two are separated by a differential pumping stage, which ensures a lower pressure in the science cell. Atoms are

transported from the first to the second cell using a translational magnetic quadropole trap.

Generally, K is not particularly well-suited for laser cooling, due to its relatively small excited state hyperfine splitting [177–179]. Therefore relatively few atoms are captured in the MOT phase. To compensate, K is cooled sympathetically, by selectively removing ^{87}Rb atoms during evaporation in a magnetic trap. Before degeneracy is reached, the atoms are loaded into an optical dipole trap, that allows a homogeneous magnetic field to be used for tuning interactions via Feshbach resonances. The atoms are prepared in a desired hyperfine state and any further evaporative cooling is performed by lowering the dipole trap power. The atoms can be cooled to a final temperature, including temperatures below the critical temperature of Bose-Einstein condensation. From this point, the atoms are available for conducting experiments as those presented in Chapters 4, 5, and 6.

The period of a full experimental cycle is approximately 80 s. The main contributions to the cycle time is MOT loading at 25 s, evaporative cooling in the magnetic trap at approximately 33 s, and evaporative cooling in the dipole trap at about 9 s.

3.2 Magneto-Optical Trapping and Cooling of ^{87}Rb and ^{39}K

The dual MOT for K and ^{87}Rb is shown in Fig. 3.1. Both K and ^{87}Rb atoms are released into the cell from commercial dispenser sources (*SAES getters*). Atoms stuck on the glass surfaces are detached by using ultraviolet diodes for light-induced atom desorption [180], which significantly increases the number of captured atoms.

A general problem in dual-species MOTs is light-assisted collisions amongst the species [181]. The relatively small K samples suffer from collisions with ^{87}Rb, which results in similar losses for both species [182]. To avoid this, a dark spontaneous optical force trap (dark-SPOT) has been implemented for ^{87}Rb. The aim of this trap is to accumulate atoms in the dark ground state $|F = 1\rangle$, which hinders light assisted collisions

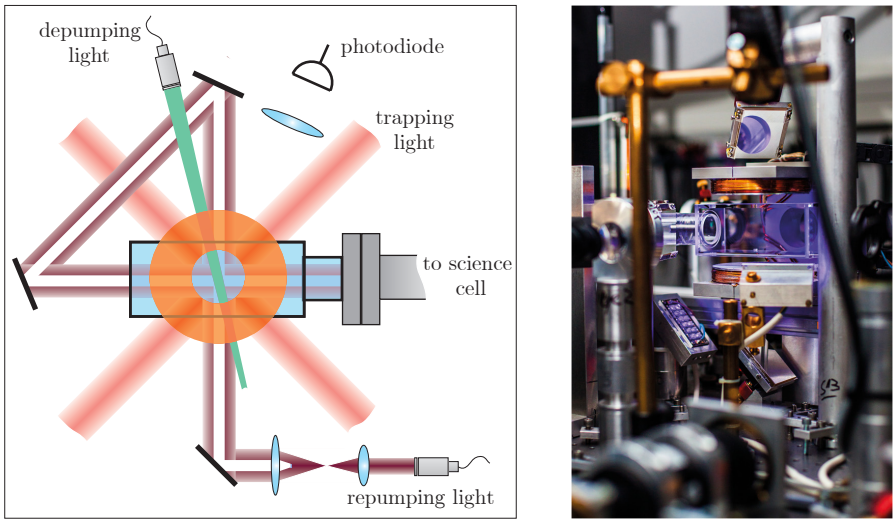

Figure 3.1: Overview of the MOT loading region. Left: Schematic overview of the MOT cell and relevant laser beams. The trapping light consists of K repumping and cooling light, as well as ^{87}Rb cooling light. Two additional trapping beams perpendicular to the figure plane is not shown. A similar figure was published in [24]. Right: Artistic photograph of the MOT loading region. The photograph is from [189].

between the two species. Previously, the dark-SPOT technique has primarily been used to increase the phase-space density of a single atomic species [183–186], but it has also been studied in context of light-assisted collisions in dual-species mixtures [187, 188].

Generally, operating a MOT requires cooling light and repumping light, which is the case for both K and ^{87}Rb. However, a K MOT requires relatively large amounts of repumping light, because of the small excited state hyperfine splitting. For ^{39}K, we use 240 mW of light detuned 24 MHz below the $|F = 2\rangle$ to $|F = 3'\rangle$ transition and 160 mW of light detuned 32 MHz below the $|1\rangle$ to $|2'\rangle$ transition, which is referred to as cooling and repumping light, respectively, even though their roles are not well separated. The light is delivered in a single fiber and sent to the MOT cell in six intersecting beams with a $1/e^2$ diameter of 34 mm.

The ^{87}Rb dark-SPOT additionally requires depumping light, besides the usual cooling and repumping light. Here, 300 mW of cooling light detuned 24 MHz below the $|2\rangle$ to $|3'\rangle$ transition is used and delivered by the same fiber and optics as the K cooling and repumping light. A separate fiber delivers 5 mW of repumping light, which is magnified to a 22 mm diameter in a telescope. Within this telescope, a small opaque disc of 6 mm is placed to realize a dark region of no repumping light by recycling the beam as shown in Fig. 3.1. The width of the dark region can be varied by translating the disk, and the beam propagates without considerable diffraction.

The setup minimizes the amount of repumping light in the center, and any atom in the ground state $|1\rangle$ will remain there until it has traversed the trap center and enters a region with repumping light. However, for ^{87}Rb, the cooling cycle $|2\rangle$ to $|3'\rangle$ is sufficiently robust that atoms rarely enter the ground state. To accelerate the process, approximately 1 mW of depumping light resonant with the $|2\rangle$ to $|2'\rangle$ transition is sent to the trap center. As a result, ^{87}Rb atoms in the dark-SPOT are mainly in the dark state $|1\rangle$ instead of in the bright cooling cycle.

The impact of the dark-SPOT configuration for ^{39}K and ^{87}Rb atom numbers is shown in Fig. 3.2. The number of ^{87}Rb atoms was measured by observing the fluorescence when switching off the depumping light and delivering additional repumping light to the trap center by a separate fiber. The fluorescence of the ^{39}K MOT is weak under normal circumstances, so the number of ^{39}K atoms is determined by quickly tuning the cooling light on resonance and measuring the fluorescence.

When both species are captured simultaneously, a bright ^{87}Rb MOT has a negative effect on the number of ^{39}K atoms. However, when ^{87}Rb is loaded in a dark-SPOT, light-assisted collisions are avoided and ^{39}K is loaded almost as if no ^{87}Rb were present.

The diameter of the dark region was optimized by translating the opaque disc and detecting the number of atoms after 25 s of loading. When the dark region is large, fewer ^{87}Rb atoms are captured and ^{39}K is unaffected by ^{87}Rb. When the dark region is small, the ^{87}Rb MOT becomes brighter, which lowers the number of ^{39}K atoms. Here, the number of ^{87}Rb atoms also decrease. The ^{87}Rb dark-SPOT generally becomes brighter with diameter size of the dark region. Thus the configuration

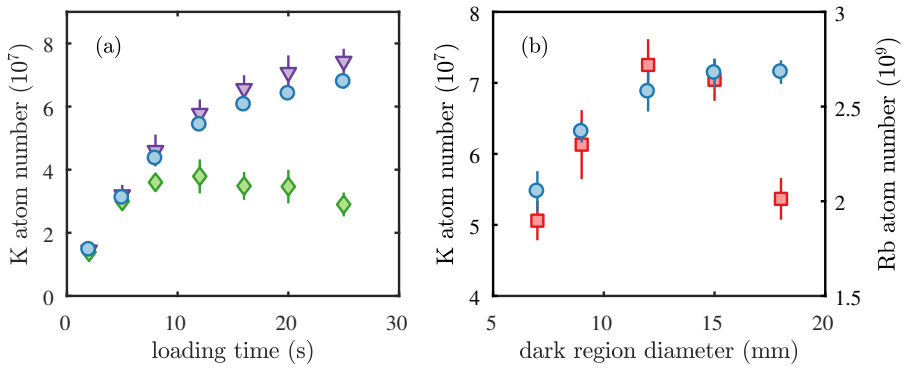

Figure 3.2: Performance of dual species MOT and dark-SPOT. (a) Atom number of ^{39}K at different loading times when loading without ^{87}Rb (purple triangles), with ^{87}Rb MOT (green diamonds) and with ^{87}Rb dark-SPOT (blue circles). (b) Atom numbers of both species versus diameter of the dark region. This figure is based on data from [24].

gradually turns into a bright MOT, but with a depumping beam which has a negative effect on atom numbers. A spot diameter of 12 mm was chosen.

Previous studies of a single-species dark-SPOT have observed a decrease in atom number, but an increase in phase-space density, when compared to a bright MOT [186]. However, the number of ^{87}Rb atoms observed in the dark-SPOT is similar to what was obtained in a bright MOT, which is attributed to the relatively large MOT beams. The phase-space density of the atoms in the MOT cell has not been directly measured, but at the end of a full experimental cycle, including evaporative cooling, the dark-SPOT configuration provides a greater number of ^{87}Rb atoms, indicating an increase in the initial phase-space density.

In the experimental procedure, the relative MOT loading time of the two species is adjusted, depending on what type of experiment is conducted. Typically, ^{87}Rb atoms are loaded for 25 s, whereas the ^{39}K MOT is only loaded in the last 3–10 s of this duration.

After loading, the atoms are cooled below the Doppler limit by applying an optical molasses. For ^{87}Rb, the excited state hyperfine splitting is much larger than the natural linewidth Γ, and the molasses is realized by

tuning the cooling laser 7Γ below the cooling transition $|2\rangle$ to $|3'\rangle$. However, the situation is different for ^{39}K where the excited state hyperfine splitting is on the order of the linewidth. Therefore, a more advanced scheme has to be employed for sub-Doppler cooling [178, 190]. When the molasses phase begins, the repumping light is tuned on resonance and the power is lowered to 5 %. The trapping light is tuned 0.5Γ below resonance, and in the duration of the molasses, the detuning is linearly increased to 2.3Γ. After 8 ms, the molasses is switched off and the ^{87}Rb and ^{39}K atoms have temperatures of 35 μK and 117 μK, respectively.

After the molasses, a pumping phase is initiated to prepare the atoms in the $|F = 2, m_F = 2\rangle$ state, which allows the atoms to be captured in a magnetic trap. A homogeneous magnetic field of 15 G is applied and σ_+ polarized light close to the $|2\rangle$ to $|2'\rangle$ transition is applied in addition with repumping light for both atomic species, in a duration of 3 ms.

3.3 Magnetic Trapping and Evaporation

When the optical trapping, cooling and pumping is completed, the coils which supplied the magnetic field for the MOT captures the atoms in a magnetic quadropole trap. These coils are mounted on a translational stage that mechanically moves the atoms 60 cm through a differential pumping stage in 1.2 s to the science cell shown in Fig. 3.3. Here, the atoms are loaded into a stationary quadropole trap centered to the cell, moving the atoms a distance of 4.5 cm. This chamber provides a significantly lower background pressure than the MOT cell, where a background vapor of atoms is required. As a result, the lifetime of the atoms is on the order of several minutes.

In the quadropole trap, ^{87}Rb atoms are evaporatively cooled selectively, while K atoms are cooled sympathetically as shown in Fig. 3.4. The initial cooling takes place in this quadropole trap, since it has a high thermalization rate [191]. However, in a quadropole trap, atoms are subject to losses from m_F-changing Majorana spin flips at sufficiently low temperatures. To address this, the trap is configured into a quadropole Ioffe-Pritchard configuration (QUIC) trap. This is implemented by adding cur-

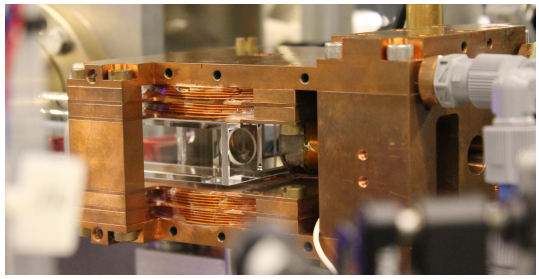

Figure 3.3: A photograph of the science cell. Pairs of coils are mounted in a copper frame around the cell. After transport from the MOT cell, the atoms are transferred through the circular entryway visible in the center of the photograph.

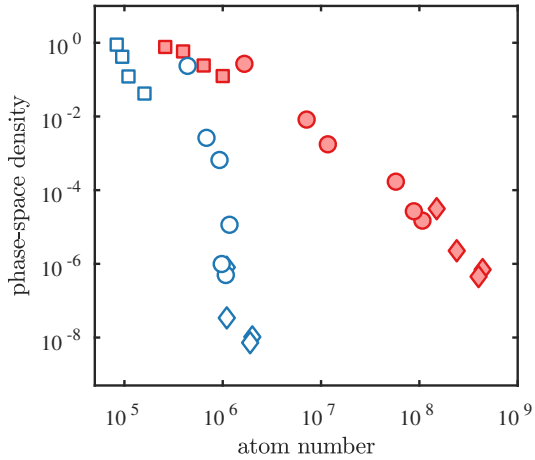

Figure 3.4: The phase-space density and atom number of both species during evaporative and sympathetic cooling. Open blue symbols are ^{39}K and solid red symbols are ^{87}Rb in quadropole (diamonds), QUIC (circles) and crossed dipole trap (squares). This figure is based on data from [24].

rent through an additional coil, creating a trap center with a non-zero magnetic field [165, 166].

To selectively evaporate ^{87}Rb atoms, radio frequency (RF) transitions to untrapped magnetic substates cannot be used, since K and ^{87}Rb have the same linear Zeeman splitting. Instead, microwave radiation close to

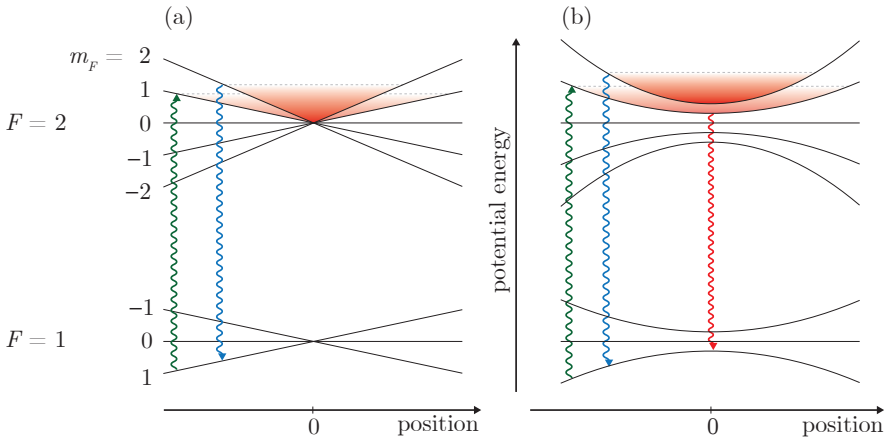

Figure 3.5: Evaporative cooling of ^{87}Rb in a quadropole trap (a) and in a QUIC trap (b) using microwave radiation. Microwave radiation removes energetic atoms in the $|F = 2, m_F = 2\rangle$ state (blue arrow), but as atoms leave the trap in the $|1,1\rangle$ state, the same radiation becomes resonant with the transition to the $|2,1\rangle$ state (green arrow). To remove atoms in this state, additional microwave radiation is added in the QUIC trap, which transfer the atoms back to the $|1,1\rangle$ state (red arrow). This figure is based on images from [165, 166].

6.8 GHz, resonant with the $|2,2\rangle$ to $|1,1\rangle$ transition of ^{87}Rb is employed. The evaporation scheme is shown in Fig. 3.5, which also highlights a problem of using this method. When atoms are transferred to the $|1,1\rangle$ state and subsequently move out of the trap, the microwave radiation becomes resonant with the $|1,1\rangle$ to $|2,1\rangle$ transition. As a result, energetic atoms pile up in the $|2,1\rangle$ state, leading to losses and heating of K atoms [175, 192, 193].

This problem is addressed after the trap is transformed to the QUIC trap configuration. The magnetic substates are no longer degenerate in the trap center and it is thus possible to add additional microwave radiation resonant with the $|2,1\rangle$ to $|1,1\rangle$ transition of ^{87}Rb, which removes atoms in the undesired substate, as shown in Fig. 3.5(b).

If ^{41}K is used, which has a positive background scattering length, it is possible to evaporate all the way to condensation of both species in the

magnetic trap. However, the negative scattering length of ^{39}K, prohibist the creation of large stable condensates, as also explained in Sec 2.4. Therefore, ^{39}K atoms need to be prepared in a magnetic substate which allows a Feshbach resonance to be employed. It is thus necessary to load the atoms into a dipole trap. If an experiment requires both K and ^{87}Rb, the evaporation in the magnetic trap is stopped shortly before condensation, but if only K is needed, all the ^{87}Rb is evaporated.

3.4 State Preparation and Evaporation in the Optical Dipole Trap

An optical dipole trap allows the tunable interactions of our system to be utilized. We use a far-detuned crossed-beam trap at a wavelength of 1064 nm. The beams have similar waists and are perpendicular to gravity. Selective cooling of ^{87}Rb is still desirable at this stage and thermal contact of the two species is thus required all the way to condensation of both species. These criteria add constraints to the trap geometry, which is discussed in the following.

The two species have similar optical transitions, so the force applied from a far red-detuned dipole trap is similar for both. However, the gravitation, proportional to mass, pulls ^{87}Rb downwards with greater force. This allows for selective cooling of ^{87}Rb, but the thermal contact between the different species is reduced as the trap power is lowered. Thus the relative gravitational sag of the two species needs to be small compared to the spacial size of the two clouds.

If trapping beams of narrow waists are chosen, the relative sag is small. The atoms will have an increased tendency to escape the trap by moving out into one of the beams of the dipole trap, instead of leaving the trap in the vertical direction due to gravity. As such, the selective cooling of ^{87}Rb is lost. If, however, beams of large waists are chosen, selective cooling of ^{87}Rb is recovered, but the relative sag between the species is too large for simultaneous condensation of both species.

Remarkably, having both selective cooling and rethermalization can only be met with a narrow range of beam waists. In Fig. 3.6 the respective

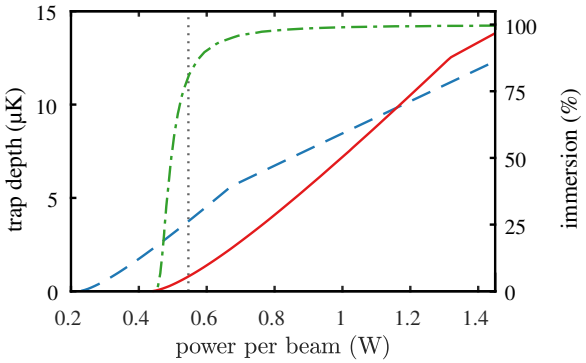

Figure 3.6: The trap depths as a function of the optical dipole trap power. The red line is the depth for ^{87}Rb, the blue dashed line is for ^{39}K, the green dash-dotted line is the immersion of the two species, and the grey dotted line indicate the critical temperature of ^{39}K. This figure is based on calculations from [24].

trap depths of the two species are shown versus the power of two beams with waists of 100 µm. Additionally, the immersion $\int (n_{\mathrm{K}}(\mathbf{r})\, n_{\mathrm{Rb}}(\mathbf{r}))^{1/2}\, \mathrm{d}\mathbf{r}$, which describes the relative overlap of the clouds, is shown. Here, n_i refers to the density of the species, which is calculated assuming Gaussian distributions using temperatures at a fraction $1/\eta$ of the trap depth of ^{87}Rb. It is thus assumed that ^{87}Rb cools evaporatively to a temperature set by the trap depth, and that ^{39}K is thermalized sympathetically. In the calculation shown, η is conservatively set to 3. Each of the two trap depth curves displays a kink. Above these points the trap depth is lower in the horizontal direction, and below the trap depth is lower in the vertical direction. With the chosen waists, selective cooling of ^{87}Rb is achieved below 1.1 W where the two trap depths intersect. Furthermore, the critical temperature of ^{39}K is calculated, assuming 2×10^5 atoms. Using the temperature set by η the critical temperature is met, while the immersion is still large. As such, trap waists of 100 µm meet the criteria outlined above. If trap waists are chosen 10–20 µm larger or smaller, either rethermalization or selective cooling is lost.

The atoms are loaded into the trap by decreasing the magnetic field and increasing the power of both beams simultaneously, usually to powers of approximately 1 W. Before further evaporation and any potential

experiments can be carried out, state preparation is required. The atoms are initially in the $|2,2\rangle$ state, and typically the $|1,-1\rangle$ state is the target. When using both species, we prepare the atoms in three steps. Since both species have the similar Zeeman splittings at low magnetic fields it is possible to transfer them simultaneously to the $|2,-2\rangle$ state, by using a rapid adiabatic sweep across all the substates. This is achieved by sweeping radio frequency radiation in 2 ms at a homogeneous magnetic field of 10 G. Next, the two species are sent to the $|1,-1\rangle$ state one at a time by using a π pulse for ^{87}Rb and an additional rapid adiabatic passage for ^{39}K. The order in which the two species are transferred to the $|1,-1\rangle$ state is crucial. If a ^{39}K atom in the $|1,-1\rangle$ state collides with a ^{87}Rb atom in the $|2,-2\rangle$, they can undergo a hyperfine changing collision, interchanging their states, which releases energy corresponding to 0.3 K [176]. This results in rapid atom loss, reducing the lifetime of the ^{39}K atoms to about 20 µs. If, however, the ^{87}Rb atoms are transferred first, no rapid losses are observed.

After the state preparation, the final evaporative cooling can be carried out. To assure rethermalization between the species, it is beneficial to carry out evaporation near the interspecies Feshbach resonance. The magnetic field is adjusted to a desired value, and the evaporation is commenced by lowering the power of the beams. If evaporation is continued to sufficiently low trap powers, condensation of ^{39}K is observed first, followed by condensation of ^{87}Rb. Typically condensates consist of about 10^4 ^{39}K atoms and 3×10^4 ^{87}Rb atoms.

It is possible to condense ^{39}K alone by evaporating all ^{87}Rb atoms in the magnetic trap. If so, the evaporative cooling of ^{39}K in the dipole trap is carried out near the Feshbach resonance at 34 G and condensates of about 5×10^4 ^{39}K atoms are obtained. This larger number of condensed atoms is attributed to a more efficient rethermalization during the final steps of evaporation.

The atoms are detected by absorption imaging after time-of-flight expansion. The dipole trap is abruptly turned off, and the atoms are allowed to expand freely. If the magnetic field is turned off during the initial expansion, the finite decay time of the field results in losses as one or multiple Feshbach resonances are crossed. Therefore, the magnetic field is kept at a definite value until the atomic clouds have diluted enough

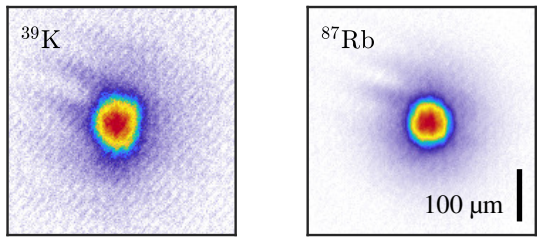

Figure 3.7: Typical images of dual condensates after 15 ms and 17 ms TOF for ^{39}K and ^{87}Rb respectively. These images have also been shown in [24].

to make effects of interactions insignificant. The field is then turned off and the atoms are imaged when the magnetic field has decayed. Both species are imaged using light resonant with the $|2\rangle$ to $|3'\rangle$ transition and repumping light is applied shortly prior to and during the imaging, delivered by an independent fiber. The readout time of the camera limits the minimal time between the images of the two species to 1–2 ms. Typical images of dual condensates are shown in Fig. 3.7.

3.5 Accuracy and Precision of the Magnetic Field

Many types of experiments with ultracold atoms require precise and accurate control of the magnetic fields. Regarding the work in this thesis, this is important to perform spectroscopy and to address specific interaction strengths near Feshbach resonances.

In order to minimize the error that is introduced by the magnetic field, several precautions have been implemented. To create the magnetic field for the atoms in the science chamber, a high stability power supply (*UCS* 65 A/25 V from *High Finesse*) is used to deliver current for the coils. For segments of the experimental procedure which are especially sensitive to the magnetic field, it is possible to switch the current source from this power supply to a home-built power supply based on a set of car batteries. Consequently, the current supply is decoupled from

the 50 Hz AC frequency of the electrical grid, as well as higher harmonics, which are sources of error.

The background magnetic field at the science cell, originating from the surrounding equipment, other laboratories, and the Earth, is subject to drifts over time. Any changes in the background magnetic field are actively canceled as explained in the following. A magnetometer is placed near the cell to measure the background field. It delivers a signal to a proportional-integral-derivative controller programmed onto a field-programmable gate array. The controller regulates a power supply, which supplies current to a large pair of coils surrounding the science cell as well as the magnetometer. This system cancels large long term drifts of the background magnetic field and is sufficiently fast to also cancel some of the 50 Hz noise from the surroundings.

A final technical procedure has been introduced to eliminate any 50 Hz noise from the surroundings. An electrical circuit monitors the 50 Hz signal from the grid directly from a power socket. If desired, it is possible to pause the experimental procedure until the 50 Hz signal reaches a certain phase in its period, and subsequently continue the procedure. It is thus possible to always execute a crucial part of the experimental procedure at the same point in the 50 Hz period. This is mainly important for experimental segments which are much shorter than the 20 ms period of the 50 Hz signal, e. g. spectrocopies.

3.5.1 Spectroscopy of ^{39}K at Large Magnetic Fields

The study of polarons presented in Chapter 6 is based on RF spectroscopy of ultracold atoms. Here, a characterization of the RF spectroscopy capabilities of the apparatus is presented, which also displays the precision and accuracy of the magnetic field.

First, relevant error contributions are discussed. If a single atom is considered, the obtainable precision is determined by the natural linewidth, the properties of the RF pulse, and from perturbations to the relevant transition from external fields. Since the transition is dipole forbidden, the natural linewidth of the transition is extremely narrow, and is thus negligible when compared to other contributions.

The constraint added by the pulse is determined by its length and shape. A pulse of length τ has a frequency width of $\sim 1/\tau$. It is possible to use sophisticated pulse shapes to narrow the precision slightly, but in general it is not possible to obtain a resolution better than the approximate inverse pulse length.

Regarding contributions to the width from external fields, the Zeeman effect is of primary relevance. The spectroscopy in Chapter 6 is performed between two hyperfine states of ^{39}K at a magnetic field of 109–122 G. The transition is sensitive to the magnetic field, which adds a limitation to the accuracy and precision of the spectroscopy. The relative Zeeman splitting of the magnetic substates in the linear regime is approximately 0.70 MHz/G. However, given the relatively small hyperfine splitting between the hyperfine states of ^{39}K, the Zeeman splitting is already far into the nonlinear regime at the relevant magnetic fields. The energies of the substates can here be described by the Breit-Rabi formula which is used to calculate the relative Zeeman splitting at the relevant fields to be 0.5 MHz/G.

To characterize the spectroscopic capabilities and the magnetic field stability of the apparatus, spectroscopies of the $|1,-1\rangle$ to the $|1,0\rangle$ transition of ^{39}K is performed at a field of 118.6 G, as shown in Fig. 3.8. A RF pulse is applied to a thermal cloud of ^{39}K, the atoms are released from the trap, a gradient magnetic field separates the two components, and the number of atoms in each component is recorded. The relative fraction of transferred atoms provides the spectroscopy signal.

For the RF spectroscopy, Gaussian envelope pulses are used with a power proportional to $\exp(-t^2/2\sigma_t^2)$, where t is time and σ_t determines the duration of the pulse. The envelope is truncated at $\pm 2\sigma_t$. The lineshape in frequency space is determined by the Fourier transform of the pulse, which is $\exp(-t^2/2\sigma_f^2)$, where $\sigma_f = 1/2\pi\sigma_t$. A number of different pulse lengths are used, which changes the spectroscopic lineshape accordingly. For each pulse length, a Gaussian fit is performed to determine the width and position of the signal.

The widths of the spectroscopy signals are shown in Fig. 3.8(b), together with a theoretical line $\sigma_f = 1/2\pi\sigma_t$. The expected behavior is followed well until a lower limit is reached. The fitted positions from the

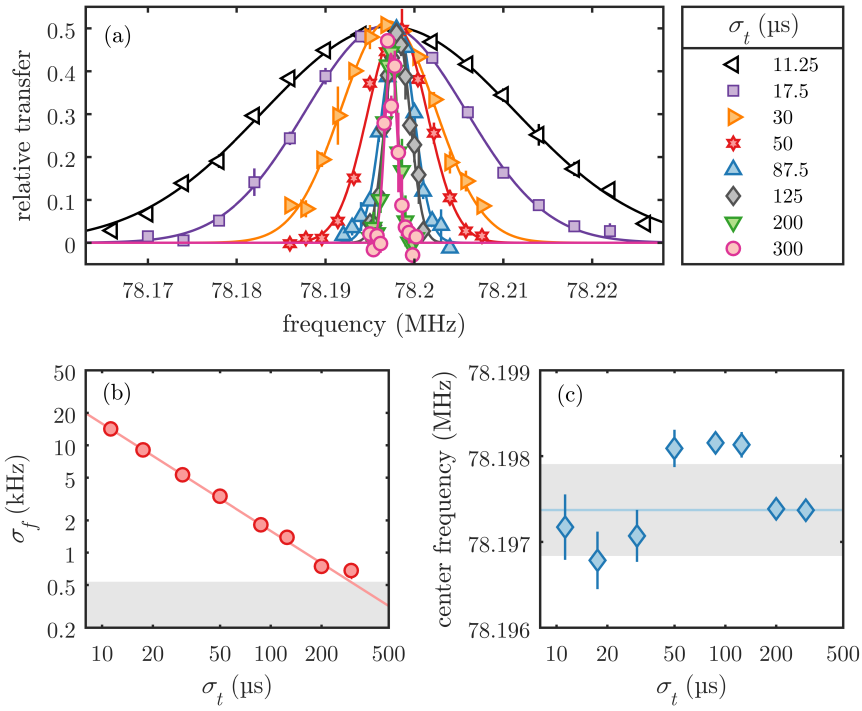

Figure 3.8: Characterization of RF spectroscopy and magnetic field stability. (a) The obtained spectroscopy signal using Gaussian pulses of various durations. The duration of the pulses is set by σ_t, which is shown for the different spectroscopies in the legend. (b) The fitted frequency width of the different spectroscopies. The line is the expected width from theory $\sigma_f = 1/2\pi\sigma_t$. (c) The fitted positions of the spectroscopies, which indicate that the magnetic field is subject to long term drifts on the order of 1 mG. The weighted average of these frequencies is calculated by using the inverse errors as weights, and the result is shown as a line. The gray shaded areas in both (b) and (c) correspond to the standard deviation of the spectroscopy positions.

spectroscopies are shown in Fig. 3.8(c). The data points from the individual spectroscopies are spread over a region of frequencies which is significantly broader than the error bars. Furthermore, the data points are organized in groups, according to the order in which they were acquired (from left to right). This behavior indicates that the background magnetic field has changed between the spectroscopies. This adds a fundamental limit to our precision and accuracy. The standard deviation of the center frequencies is 0.5 kHz, corresponding to 1 mG.

CHAPTER 4

TUNABLE DUAL-SPECIES BOSE-EINSTEIN CONDENSATES

Ultracold gases provide an excellent setting for exploring the properties of interacting quantum fluids. In this chapter, dual-species Bose-Einstein condensates with tunable interactions are studied. The main interest is to investigate the miscibility and phase separation of the two components, as introduced in Sec. 2.4. The results presented here, have been published in references [24–26].

The studies revolve around using the interspecies Feshbach resonance of ^{39}K and ^{87}Rb in the $|F = 1, m_F = -1\rangle$ state [33], introduced in Chapter 1 and shown again in Fig. 4.1(a), to tune the scattering length a_{KRb} between dual-species Bose-Einstein condensates. As discussed in Sec. 2.4, the two components can coexist, collapse, or phase separate, depending on the value of the miscibility parameter $\Delta_{\mathrm{stab}} = g_{11}g_{22}/g_{12}^2 - 1$, where 1 and 2 refer to the two components. In Fig. 4.1(b), Δ_{stab} for ^{39}K and ^{87}Rb near the Feshbach resonance is shown, which exhibits a phase transition. Additionally, examples of absorption images after expansion at different interactions are shown in Fig. 4.1(c-f).

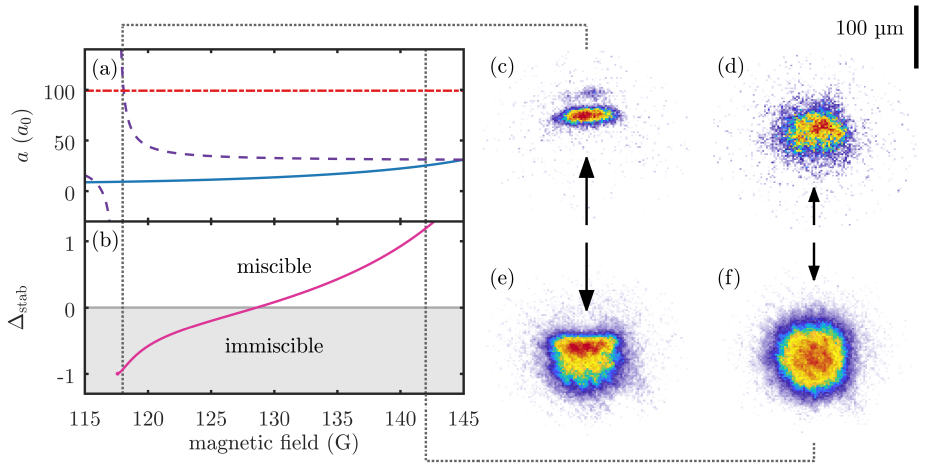

Figure 4.1: Interaction properties of ^{39}K and ^{87}Rb dual-condensates in the $|F = 1, m_F = -1\rangle$ state. (a) Scattering lengths of ^{87}Rb (red dash-dotted), ^{39}K (blue), and between the species (purple dashed). Miscibility parameter of the dual-condensates, indicating a phase transition at ~ 128 G. The two vertical dotted lines in (a-b) refer to respectively strong and weak repulsive interactions. In (c-f), example absorption images after expansion at these interactions are shown. Here, (c-d) is ^{39}K and (e-f) is ^{87}Rb, while (c) and (e) are strongly interacting and (d) and (f) are weakly interacting. At strong interactions, both the column densities and mass centers of the components are modified significantly. A similar figure was presented in reference [26].

In order to acquire precise knowledge on the properties of the Feshbach resonance, it was characterized through three measurements to obtain its position B_0, width Δ_F, and background scattering length a_{bg}, which are presented in in Sec. 4.1. The background scattering length is obtained by locating the miscible to immiscible transition point which depends on the interspecies interaction strength and thus a_{bg}.

Based on the research of the transition, a collaboration was initiated, with the aim to understand dynamics and phase separation of two-component Bose-Einstein condensates in more detail. The collaborators have developed a theoretical model to simulate the behavior of two interacting condensates [71, 194]. The collaboration yielded a theoretical

study of the in-trap phase separation of ^{39}K and ^{87}Rb [25], as well as a detailed analysis of the expansion behaviour of the two components [26].

The results from the theoretical in-trap study are reviewed in Sec. 4.2 and the study of the expansion behavior of two-component condensates is presented in Sec. 4.3.

4.1 Characterization of the Interspecies Feshbach Resonance

The center of the interspecies Feshbach resonance is determined by loss spectroscopy. A sample of ultracold ^{39}K and ^{87}Rb atoms is prepared in an optical dipole trap in the $|1,-1\rangle$ state, following the experimental procedure outlined in Chapter 3. The final evaporation is performed at a magnetic field of 119.6 G, near the Feshbach resonance at 117.6 G, and is stopped slightly before condensation. After the evaporation the trap depth of the dipole trap is increased slightly, and the magnetic field is adjusted to a desired target value. At a given magnetic field, the atoms are held for a variable amount of time, and the number of atoms are recorded.

In Fig. 4.2(a), the three-body recombination rate L_3^{KRbRb} of one ^{39}K atom performing recombination with two ^{87}Rb atoms is shown. To obtain L_3^{KRbRb} from the decaying atom numbers, a numerical fitting procedure was used, which is described in more detail in Chapter 5. On both sides of the resonance, exponential fits are performed to extract the position $B_0 = 117.56(2)$ G. In absence of a detailed model of the loss rate at the resonance center, this region has been excluded in these fits and provides the uncertainty.

The width of a Feshbach resonance determines the position where the scattering length crosses zero as $a(B = B_0 + \Delta_{\mathrm{F}}) = 0$. To obtain this position for the interspecies resonance, the rethermalization rate between the two species is measured in a range of magnetic fields. The two species are prepared in the dipole trap as usual, but directly after the state preparation, the magnetic field is set to a target value where the

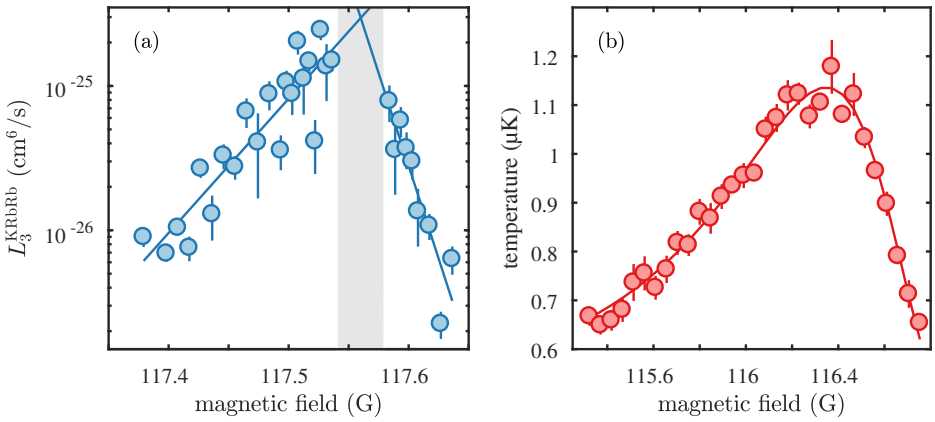

Figure 4.2: Characterization of the interspecies Feshbach resonance. (a) An increase of the three-body recombination coefficient on either side of the resonance determines the resonance position. On both sides, an exponential fit is performed, excluding the center area shaded gray. (b) The temperature of ^{39}K after sympathetic cooling with ^{87}Rb. A fit is performed to locate the zero crossing of the scattering length an thus determine the width of the Feshbach resonance. This figure is based on data from [24].

evaporation is carried out. Since mainly ^{87}Rb is cooled evaporatively, the temperature of ^{39}K will depend strongly on the rethermalization rate.

In Fig. 4.2(b), the temperature of ^{39}K after evaporation is shown versus the magnetic field. To determine the point of least rethermalization, a fit is performed, using the expression

$$T_{\mathrm{K}}(B) = A_1 + A_2 \exp\left((A_3[a_{\mathrm{KRb}}(B)]^2\right). \tag{4.1}$$

where A_1, A_2 and A_3 are fitting parameters which contain information about temperatures and rethemalization rates. [176, 195]. This expression uses the basic expression for the scattering length $a_{\mathrm{KRb}}(B)$ near a Feshbach resonance, Eq. (2.31), and assumes that the difference in temperature between ^{39}K and ^{87}Rb decreases exponentially with time, with a rate proportional to the collisional cross section $\sigma = 4\pi a^2$, given by Eq. (2.25). The fit provides a zero crossing of 116.35(3) G, which determines the the width to be $\Delta_{\mathrm{F}} = 1.21(5)$ G.

The last parameter of the Feshbach resonance a_{bg} is determined by analyzing the miscible to immiscible transition below.

4.1.1 Center-of-Mass after Time-of-Flight Expansion

The tunable interactions of the two species allow the transition from a miscible to an immiscible mixture to be studied. Prior to this study, the transition has been observed in both Bose mixtures [75, 196, 197] and in Bose-Fermi mixtures [195, 198]. In Bose mixtures, the miscibility of the system can be determined by Δ_{stab}.

To study the transition, dual condensates were created in the vicinity of the interspecies Feshbach resonance. Subsequently, the dipole trap power was increased to decrease the relative gravitational sag slightly, resulting in trap frequencies of $(\omega_\rho, \omega_z)/2\pi = (136, 189)$ Hz for ^{39}K and $(96.9, 129)$ Hz for ^{87}Rb, at a temperature of 200 nK and a relative gravitational sag of 6.9(5) µm. The magnetic field was then ramped to a target field in 300 ms, and after additional 10 ms of hold time, the ^{39}K and ^{87}Rb were released from the trap and imaged after 15 ms and 17 ms, respectively. The produced condensates contained approximately 1.2×10^4 ^{39}K and 2×10^4 ^{87}Rb atoms.

The center-of-mass positions after time-of-flight expansion for both condensates was determined, relative to the condensate positions without the other species present, which is shown in Fig. 4.3(a) versus the magnetic field. It is clearly seen that stronger repulsive interactions result in a larger separation. At weak interactions above 130 G, the change in center-of-mass position is vanishing.

Previously, it has been observed that the growth in center-of-mass separation begins at the phase transition point $\Delta_{stab} = 0$ [75]. By assuming this behavior, the measured separation can be used to determine the background scattering length empirically. To do so, the center-of-mass separation is evaluated versus Δ_{stab} for various trial values of a_{bg}. The scattering length between ^{39}K atoms is caclulated using the Feshbach parameters provided in reference [97]. At each trial value of Δ_{stab}, a fit is performed, assuming a constant separation for $\Delta_{stab} > 0$ and a linearly growing separation for $\Delta_{stab} < 0$, as shown in Fig. 4.3(b). For very strong interactions, a non-linear increase in separation is observed, and data at

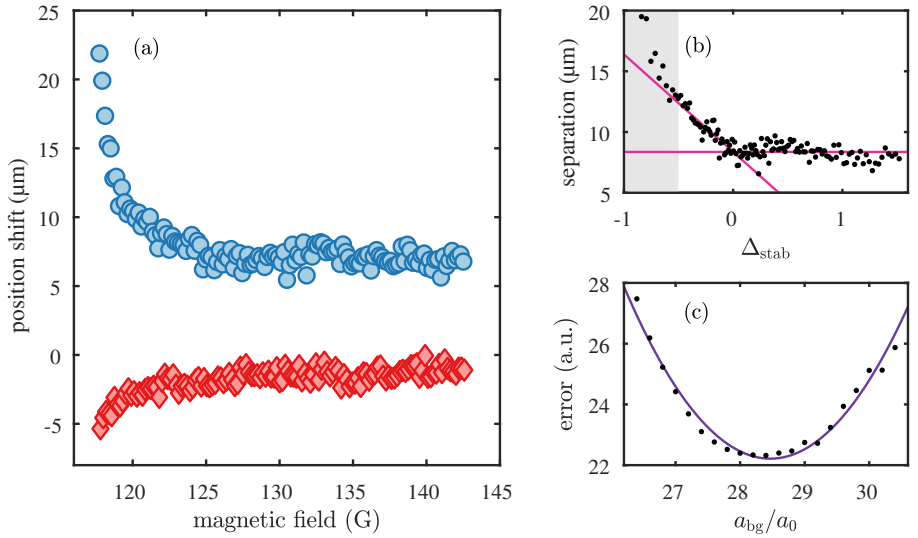

Figure 4.3: The relative positions of dual-species condensates after expansion. (a) The center-of-mass position shift of ^{39}K (blue circles) and ^{87}Rb (red diamonds) condensates after time-of-flight, which shows a clear effect from interactions. The origin of the vertical axis is the position of a freely expanding condensate in absence of the other species. (b) The separation of the condensates versus Δ_{stab}, as well as linear fits, where data in the gray area have been excluded from the fit. (c) The fitting error for different values of a_{bg}. The value of a_{bg} in (b) is $28.5a_0$. This figure is based on data from [24].

$\Delta_{stab} < -0.5$ is excluded in the fit. The fitting error for a number of a_{bg} trial values is shown in Fig. 4.3(c), where a parabola has been fitted to provide an estimate of a_{bg}. This method yields $a_{bg} = 28.5(8)a_0$, comparable to theoretical predictions of the background scattering length in other m_F states [33].

Calculations of the in-situ distributions of the two condensates reveal that the Thomas-Fermi radii of the components hardly overlap, due to the gravitational sag. The observed separation is thus attributed to interactions during the initial time-of-flight after the components have been released.

4.2 Theory of in-Trap Phase Separation and Dynamics

In this section, theoretical results regarding the in-trap phase separation and dynamics are presented [25]. The theoretical model is an extension of the Zaremba-Nikuni-Griffin kinetic model which includes interactions between condensate and non-condensate atoms [71, 194, 199]. Consequently, finite temperature effects are captured.

Several previous studies of two-component Bose-Einstein condensates have examined the density distributions of the condensates while varying a single parameter like interspecies interaction [64, 196] or atom number [61, 76]. Here, a more complete volume of the relevant parameter space is explored, by varying interaction strengths g_{11}/g_{12}, g_{12}/g_{22}, atom numbers, and temperature.

4.2.1 Simulation Parameters

In the simulations, dual-species condensates of ^{39}K and ^{87}Rb are considered, under conditions related to the experimental setup presented in this thesis. The theoretical results are, however, generally applicable to many multi-species experiments.

The harmonic potential $V_i(\mathbf{r}) = m_i/2(\omega_{\rho,i}^2\rho^2 + \omega_{z,i}^2 z^2)$ confines the atoms, where $i = 1,2$ refers to the species. In the remainder of this section, 1 refers to ^{87}Rb and 2 refers to ^{39}K. The radial and axial trap frequencies for ^{87}Rb (^{39}K) are respectively $\omega_\rho/2\pi = 119\,\text{Hz}$ (178 Hz) and $\omega_z/2\pi = 166\,\text{Hz}$ (248 Hz), which fulfill $m_1\omega_{j,1}^2 = m_2\omega_{j,2}^2$, where j refers to the axis.

Simulations are performed for various atom numbers and temperatures. Regarding atomic interactions, both arbitrary values of g_{11}, g_{22} and g_{12}, and values specific to ^{39}K and ^{87}Rb in the $|1,-1\rangle$ state are considered.

The expression for the trapping potential indicates that the case of a negligible gravitational sag is considered. This can be achieved experimentally by employing an optical dipole trap with a carefully selected wavelength [200]. The gravitational sag is g/ω_z^2, where g is the acceleration due to gravity, and $\omega_z/2\pi$ is the trapping frequency in the direction

of gravity. One method to eliminate the relative sag between two species is using a dipole trap which provides identical trap frequencies to the two species. Alternatively, an additional optical potential introducing an upward force proportional to mass can be employed.

Both these approaches require an optical potential of the same wavelength. In the simplified case of a two-level atom, the dipole force is proportional to $\Gamma/\nu_0\delta$, where Γ is the linewidth, ν_0 is the atomic transition frequency and δ is the detuning of the optical field [201]. The same trap frequencies for atoms of species 1 and 2 can be obtained by imposing

$$\frac{m_2}{m_1} = \frac{\Gamma_2 \nu_{0,1}^3 \delta_1}{\Gamma_1 \nu_{0,2}^3 \delta_2}, \tag{4.2}$$

where the relative detunings δ_1/δ_2 determines the wavelength necessary for canceling the gravitational sag. A full calculation for a mixture of ^{39}K and ^{87}Rb including all relevant transitions provides a wavelength of approximately 806 nm [25].

4.2.2 Ground-State Phase Diagram in a Harmonic Trap

In Fig. 4.4, a series of ground state phase diagrams of the mixture is presented for different interactions and for varying atom numbers. The in-trap density distributions are quantified by a new parameter

$$\Delta n_{\mathrm{norm}} = \frac{n_{\mathrm{c},1}(\mathbf{0})}{\max n_{\mathrm{c},1}(\mathbf{r})} - \frac{n_{\mathrm{c},2}(\mathbf{0})}{\max n_{\mathrm{c},2}(\mathbf{r})}, \tag{4.3}$$

which describes to which degree the density maxima of the two condensates are expelled from the center of the trap. If two components overlap, with both having density maxima in the trap center as in Fig. 4.4(g), then $\Delta n_{\mathrm{norm}} = 0$. If one component is fully repelled from the trap center, $\Delta n_{\mathrm{norm}} = \pm 1$ as in Fig. 4.4(f) and (i). If the distributions are asymmetric as in Fig. 4.4(e), then Δn_{norm} does not provide a meaningful description, indicated by white coloring.

The phase diagrams of Fig. 4.4(a-d) are divided into four quadrants by the lines $g_{12}/g_{22} = g_{11}/g_{12} = 1$. These quadrants provide a rough indication of the density distributions. Upper left is asymmetrical immiscible, lower right is miscible, and the last two are symmetrical immiscible

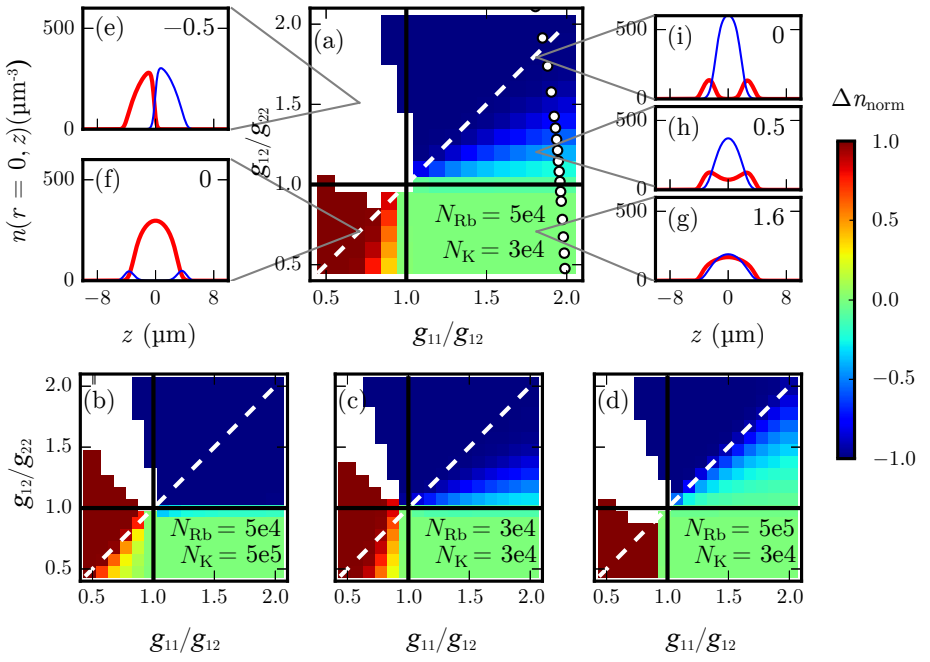

Figure 4.4: Ground state phase diagrams for density distributions of dual condensates of ^{39}K and ^{87}Rb. (a-d) The phase diagrams paramitrized by Δn_{norm} (see text) for different interactions, where species 1 is ^{87}Rb and species 2 is ^{39}K. The white dashed lines show $\Delta_{\mathrm{stab}} = 0$. Atom numbers are indicated in the subfigures and white circles in (a) show interactions relevant for the mixture in the $|F = 1, m_F = -1\rangle$ state. (e-i) Examples of density profiles at different regions of the phase diagrams, where the red line is ^{87}Rb and the blue is ^{39}K. The value of the miscibility parameter Δ_{stab} is shown in the subfigures. This figure is based on data from [25].

distributions. However, the position and width of the boundary between these distributions depend on atom numbers.

This dependence on atom number can be understood by considering the limiting case of $N_1 \gg N_2$. Here, the effect of interactions from species 2 on 1 is negligible. If $g_{12}/g_{22} < 1$ the trapping potential V is stronger than the interspecies repulsion experienced by species 2 and effectively a harmonic trap is felt. If however $g_{12}/g_{22} > 1$, the repulsion

becomes stronger than the trap, and species 2 will form a shell structure around species 1.

These results demonstrate that the actual density distribution depends on many details of the system and is thus poorly described by the miscibility parameter. Even phase separation is not captured well. An alternative parameter to describe the distribution is Δn_{norm}, but it require numerical simulations to calculate. However, it is also possible to acquire information about Δn_{norm}, and thus the miscibility and in-trap distribution, through observations of dipole oscillation frequencies, which is presented in the following section.

Finite temperature effects were studied in context of the ground state and phase separation. By adjusting the atom number such that the number of condensed atoms are similar for different temperatures, varying the temperature had little to no effect on condensate density distributions [25].

4.2.3 Two-Component Dipole Oscillations

Now, the dynamical properties of dual-species condensates are studied. The interactions relevant to ^{39}K and ^{87}Rb in the vicinity of the inter-species Feshbach resonance are considered with the same atom numbers as in Fig. 4.4(a), where these interactions are shown in the phase diagram.

To initiate the oscillations, the trap centers for the two components are increased linearly to 0.2 µm in 5 ms and afterwards back to 0 µm in 1 ms. This initiates dipole oscillations with amplitudes small compared to the Thomas-Fermi radii of the condensates. Simulations are carried out for different interactions and temperatures.

Properties of the resulting dipole oscillations are shown in Fig. 4.5 for different interactions and temperatures. For a given interaction, the two condensates oscillate with the same frequency ω_{dip}, but with opposite phase. For reference, the density distribution quantified by Δn_{norm} is shown in Fig. 4.5(a), which once again highlights that the transition from miscible to immiscible does not happen at $\Delta_{\mathrm{stab}} = 0$, but gradually in the region $\Delta_{\mathrm{stab}} \approx 0.2$–1.

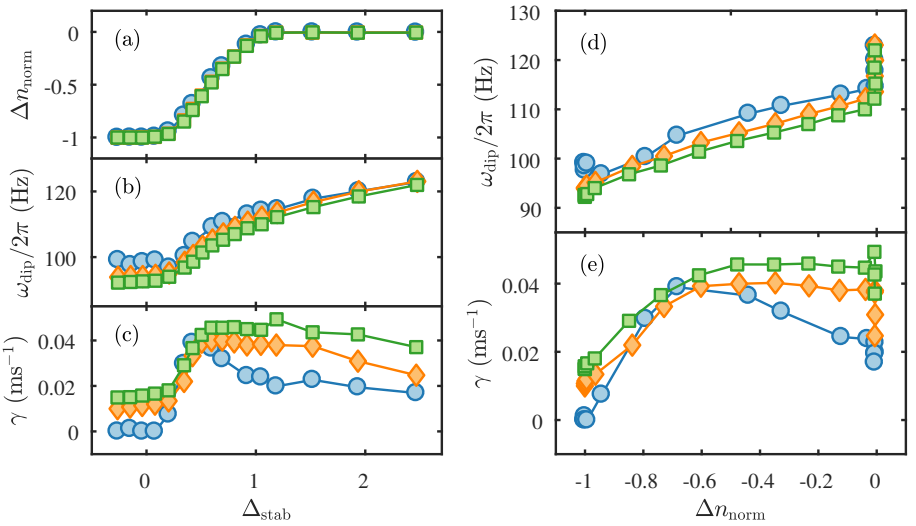

Figure 4.5: Dynamical properties of the dual condensates at different temperatures and interactions. Blue circles are simulations at $T = 0$, orange diamonds are at $T = 100\,\mathrm{nK}$ and green squares are at $T = 150\,\mathrm{nK}$. In (a), Δn_{norm} is shown, the dipole oscillation frequency is shown in (b) and the corresponding damping rate is shown in (c). (d-e) Same data as (b-c), but plotted versus Δn_{norm} of (a). This figure is based on data from [25].

Across the range of interactions, both frequency and damping rate of the oscillations are changed with interaction. The oscillation frequency is similar for different temperatures, but damping rate changes since collisions with thermal atoms introduce damping. In Fig. 4.5(d), the oscillation frequency is shown versus Δn_{norm}, which demonstrates a correlation between ω_{dip} and Δn_{norm}. This correlation was tested and reproduced for various atom numbers [25].

4.2.4 Discussion

To summarize, the miscibility parameter Δ_{stab} provides an incomplete description of the density distributions of two-component condensates. The distributions depend in a more complicated manner on the relative interactions and atom numbers. An alternative parameter Δn_{norm}

was suggested to describe the density distributions, and by simulations it was shown that information about this parameter can be obtained by measuring the dipole oscillation frequency of the two components.

The simulations were performed for components with identical trap centers. For trap center separations on the order of the Thomas-Fermi radii it is likely that the transition from miscible to immiscible is more apparent. Additionally, the phase diagrams depend on the relative trap frequencies of the two components, which were kept constant in the simulations presented here.

Additional details, discussions and results are available in the publication [25].

4.3 Expansion of Finite Temperature Dual-Species Condensates

In this section, the expansion dynamics of dual-species Bose-Einstein condensates are studied, through a detailed comparison between experimental observations and numerical simulations [26].

The miscibility of dual-species condensates is often studied by performing observations after time-of-flight expansion [24, 75–77, 202], because in-situ observations are technically challenging.

Here, a full simulation of the dynamical expansion is presented. The aim is to study how the interspecies interactions manifest in the atomic density distributions after time-of-flight. This is especially interesting, since the role of miscibillity in trapped systems is not fully resolved, as shown in the previous section. The validity of the simulations are confirmed by qualitative comparison with experimental observations.

4.3.1 Simulation and Experimental Parameters

The same theoretical framework as in Sec. 4.2 is used, where finite temperature effects are taken into account [71, 194, 199]. The simulation parameters are based on the measurements presented in Sec. 4.1.1 and shown in Fig. 4.3.

Experimental data was acquired under similar conditions. The expansion time was chosen to be longer, which allowed spacial features to be resolved better. In the measurements, the trap frequencies were $(\omega_\rho, \omega_z)/2\pi = (132, 186)$ Hz for ^{39}K and $(93, 124)$ Hz for ^{87}Rb, and the relative gravitational sag was 7.1(7) µm. The condensates contained approximately 8×10^3 ^{39}K and 5×10^4 ^{87}Rb atoms, at temperatures 150–200 nK. Finally, absorption images are acquired after 23 ms for ^{39}K and 24.7 ms for ^{87}Rb [26].

4.3.2 Center-of-Mass Positions after Expansion

First, a comparison between numerical simulations and the data presented in Sec. 4.1.1 and shown in Fig. 4.3 is performed. In Fig. 4.6(a), the experimentally obtained center-of-mass positions are compared to positions obtained from simulations versus the miscibility parameter Δ_{stab}. The experimental and theoretical results agree qualitatively, but in general, the experimentally obtained positions are further separated from the unperturbed condensate mass centers.

Several sources potentially contribute to this systematic error. This includes an inaccurate evaluation of the center-of-mass condensate position, an inaccurate model for the scattering lengths in the systems, and a lack of knowledge about the relative gravitational sag.

To evaluate whether the transition point $\Delta_{\text{stab}} = 0$ can be obtained from the center-of-mass positions, the derivative of the numerically determined ^{39}K condensate position is calculated and shown in Fig. 4.6(b). Due to conservation of momentum, calculating the derivative from either mass center is equivalent. If a well-defined transition point exists, a similarly well-defined sharp change of the derivative should exist. However, no such sharp increase is observed. The derivative was calculated for simulations with other values for the relative gravitational sag, but the results are similar [26].

4.3.3 Density Distributions after Expansion

Now, the spatial density distributions are examined. From here on, the simulations are compared to the experimental data with long expansion

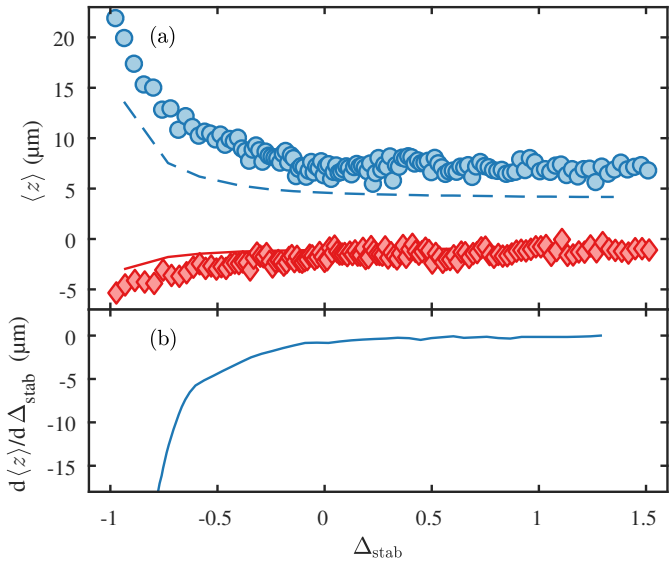

Figure 4.6: (a) Center-of-mass positions $\langle z \rangle$ of dual-species Bose-Einstein condensates 15 ms and 17 ms of expansion for ^{39}K and ^{87}Rb. The blue circles and red diamonds are center-of-mass positions for ^{39}K and ^{87}Rb, respectively. The experimental data is compared to numerically calculated mass centers, shown as a dashed blue curve for ^{39}K and a red solid curve for ^{87}Rb. The origin of the vertical axis is the position of a freely expanding condensate in absence of the other species. (b) The derivative of the ^{39}K condensate mass center, which does not show a well-defined transition. The experimental data is also shown in Fig. 4.3. This figure is based on data from [26].

times. Consequently, the experimentally obtained density distributions are approximately twice as large as the simulated distributions, but this has no influence on main arguments and conclusions.

The simulated density distributions before and after expansion for mixtures in the miscible and immiscible limits are shown, compared to experimental images, as column-integrated distributions in Fig. 4.7 and as doubly-integrated distributions in Fig. 4.8. Before expansion, the miscible and immiscible distributions are similar, since the gravitational sag is on the order of the sum of the Thomas-Fermi radii. After expansion, the experimental and the simulated data yield similar results. The

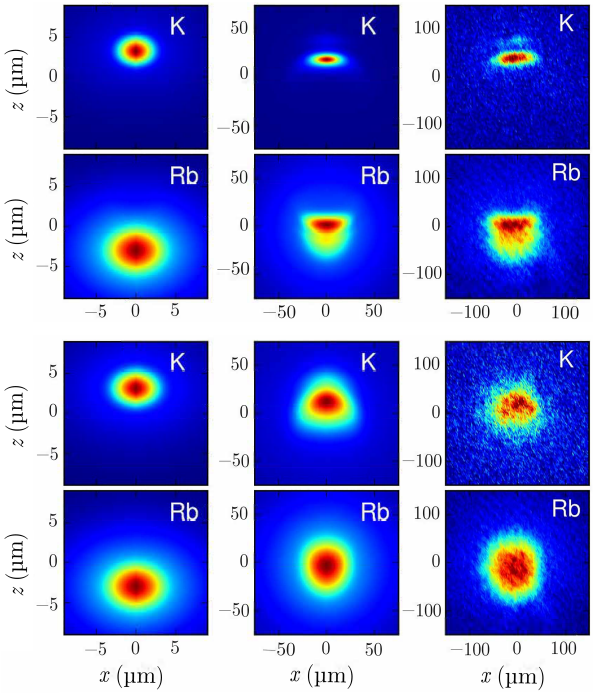

Figure 4.7: Column-integrated density distributions of ^{39}K and ^{87}Rb atoms. Top rows are immiscible interactions $\Delta_{\text{stab}} = -0.93$ (experiment: $\Delta_{\text{stab}} = -0.98$), while bottom rows are miscible interactions $\Delta_{\text{stab}} = 1.2$. The left column is simulated in-situ distributions, the center column is simulated distributions after 14 ms of expansion, and the right column is experimentally obtained distributions after 23 ms and 24.7 ms of expansion. The center of the coordinate system for the simulated results corresponds to a freely falling frame centered between the two trap centers, while the coordinate system for the experimental results is centered to the position of the freely expanding condensate without the presence of the other species. In each panel, the signal is normalized to the peak optical density. This figure is based on data from [26].

miscible and immiscible interactions clearly result in different distributions, with the immiscible interactions providing the greatest modification. However, even in the miscible case, a faint interface has developed between the two components.

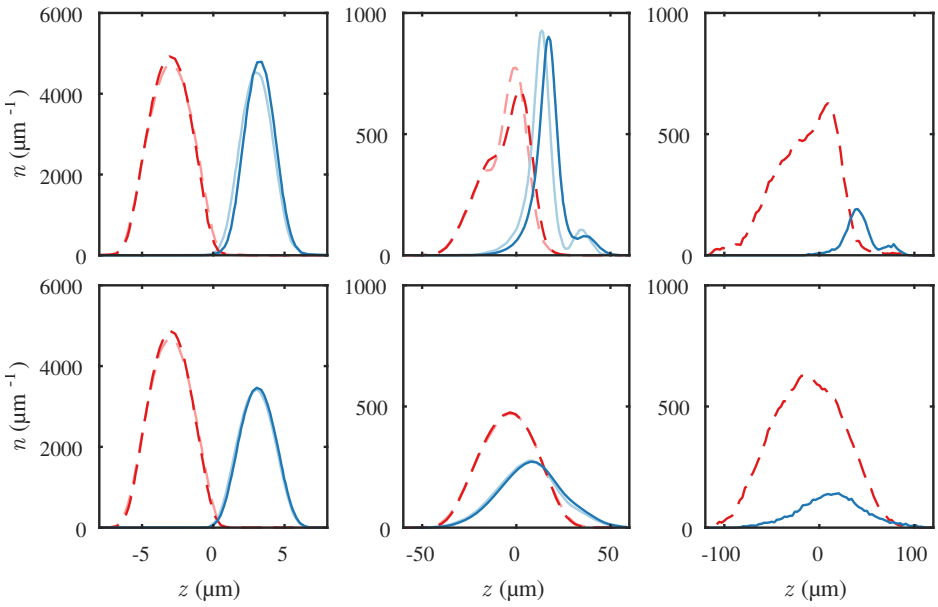

Figure 4.8: Doubly-integrated density distributions of ^{39}K and ^{87}Rb condensate atoms. Blue solid curves are ^{39}K and red dashed curves are ^{87}Rb. Bright colors are $T = 0$ simulations, while dark colors are at finite temperature. Top row is immiscible interactions $\Delta_{\text{stab}} = -0.93$ (experiment: $\Delta_{\text{stab}} = -0.98$), while bottom row is miscible interactions $\Delta_{\text{stab}} = 1.2$. The left column is simulated in-situ distributions, the center column is simulated distributions after 14 ms of expansion, and the right column is experimentally obtained distributions after 23 ms and 24.7 ms of expansion. The center of the coordinate system for the simulated results corresponds to a freely falling frame centered between the two trap centers, while the coordinate system for the experimental results is centered to the position of the freely expanding condensate without the presence the other species. This figure is based on data from [26].

The strong immiscble interactions give rise to interesting features in the density distributions. A sharp interface has developed between the two components, and the ^{39}K condensate has been heavily compressed. Furthermore, in the doubly-integrated profiles of Fig. 4.8, the ^{87}Rb condensate has a steep shoulder structure, located opposite to the ^{39}K condensate, and the ^{39}K condensate exhibits a secondary peak located opposite the ^{87}Rb condensate. These features are caused by the

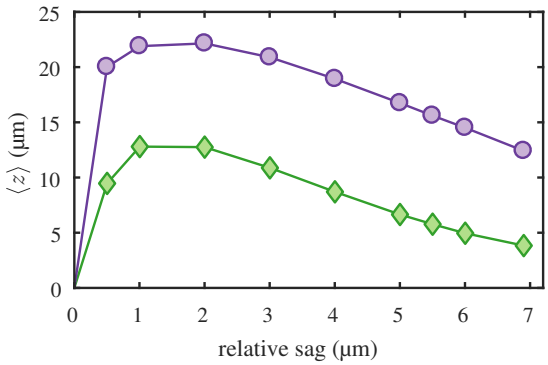

Figure 4.9: Center-of-mass position of ^{39}K condensate atoms after 14 ms of expansion time for different initial relative gravitational sags. Purple circles indicate immiscible interactions $\Delta_{\text{stab}} = -0.93$, and green diamonds are for miscible interactions $\Delta_{\text{stab}} = 1.2$. The origin of the vertical axis is the center position of a freely falling ^{39}K condensate without the presence of ^{87}Rb. This figure is based on data from [26].

initial strong mutual repulsion of the condensates, which forms dispersive shock waves [203, 204].

The full simulations are also compared to simulations based on the Gross-Pitaevskii equation, which neglects finite temperature effects. The presence of thermal clouds suppresses the discussed features slightly, but they remain visible. Note that the experimental observations were carried out under slightly different conditions, but the same features still show, indicating that the effects causing them are not restricted to a narrow region of the parameter space.

4.3.4 Effect of the Gravitational Sag

The effect of varying the relative gravitational sag is now explored theoretically. In Fig. 4.9, the center-of-mass position of the ^{39}K condensate is shown for different sags at miscible and immiscible interactions. It is not surprising that the center-of-mass position approaches zero with an increasing sag. The maximum position shift is obtained at 1–2 μm, where the relative sag is considerably smaller than the Thomas-Fermi radii. At

very small relative sags, the position shift becomes small again. If the two condensates have similar trap centers, the system is symmetric, and the condensates do not repel each other in a preferred spatial direction.

4.3.5 Discussion

Full simulations of expanding dual-species Bose-Einstein condensates at finite temperatures was presented. The results agreed well with experimental observations. The simulations predicted a center-of-mass separation of the two components, as observed in several experiments [24, 75–77, 202]. An analysis however showed that the separation does not necessarily provide a distinct point of the miscible to immiscible transition of two-component Bose-Einstein condensates. This disputes the measurement of the background scattering length performed in Sec. 4.1, which assumed that the mass centers provided a clear transition point.

The density distributions of the condensates before and after expansion were also studied, which revealed interesting spatial features. Both for miscible and immiscible interactions, the repulsive interspecies interaction forms an interface, which is most distinct for immiscible interactions. Additionally, the strong repulsion in this limit generated dispersive shock waves.

In the manuscript [26], additional results, details and discussions are available. This includes an analysis of the miscibility between thermal clouds and condensates.

CHAPTER 5

THREE-BODY PHYSICS IN ^{39}K AND MIXTURES OF KRB

This chapter covers the experimental studies of Efimov physics which were carried out as a part of this dissertation. Efimov physics addresses the properties of three interacting particles. The short-range two-body interactions lead to the formation of an intricate spectrum of three-body states denoted Efimov states. A more detailed introduction of Efimov physics is given in Sec. 2.5.

The studies of Efimov physics presented in this chapter are divided into two works [27, 28]. In the first, a study of the three-body physics of ultracold KRb mixtures was conducted [27]. The first observations heteronuclear Efimov resonances were made in a mixture of ^{41}K and ^{87}Rb [117], but have later been subject to controversy due to inconsistencies with theory and other experimental results. This motivated the study of three-body physics in both ^{39}K^{87}Rb and ^{41}K^{87}Rb mixtures presented in this chapter. In the second work, the properties of a homonuclear Efimov resonance in ^{39}K is studied in detail, and a remarkable dependence on temperature is observed [28].

The chapter is structured as follows. First, in Sec. 5.1, methods for evaluating losses in both ensembles of one and two components are presented, which is central in studying Efimov physics. Then, the controversy of Efimov physics in KRb mixtures is revised in Sec. 5.2. Next, the experimental results for three-body physics in KRb mixtures are presented and discussed in Sec. 5.3. Finally, studies of the temperature dependence of an Efimov resonance in ^{39}K are presented in Sec. 5.4.

5.1 Evaluation of Three-Body Losses

The presence of an Efimov state manifests itself in an increase of the three-body recombination rate at a specific interaction strength a_-. It is therefore important to properly obtain this rate from the time evolution of atom numbers and temperature. In this section, methods for evaluating three-body losses are presented. The case of a homonuclear ensemble is considered first, which applies to the measurements presented in Sec. 5.3. Next, the framework is extended to the case of bosonic mixtures, which applies to studies of three-body physics in KRb mixtures.

The losses and heating can be described through coupled differential equations. These can be solved analytically in the homonuclear case, whereas numerical methods are used for mixtures. By performing fits to the experimental data, the three-body recombination coefficient L_3 is obtained as a fitting parameter.

A single species ensemble undergoing three-body recombination is now considered [49]. The rate at which an atom undergoes three-body recombination at a certain density n is $L_3 n^2$. When atoms are confined in a harmonic potential, the inhomogeneous density distribution has to be taken into account by integration, weighted with density

$$\frac{\mathrm{d}N}{\mathrm{d}t} = -L_3 \int n(\mathbf{r})^3 \mathrm{d}\mathbf{r} = -\beta L_3 \frac{N^3}{T^3}, \qquad \beta = \frac{1}{\sqrt{27}} \left(\frac{m\bar{\omega}^2}{2\pi k_\mathrm{B}} \right)^3, \tag{5.1}$$

where the integral is solved assuming a Gaussian thermal distribution.

Atoms are primarily lost from the high density center of the trap, where the average energy of atoms is lower. Consequently, the average energy per remaining atom increases, which is equivalent to heating. The mean potential energy of lost atoms is

$$\frac{\int n(\mathbf{r})^3 V(\mathbf{r}) \mathrm{d}\mathbf{r}}{\int n(\mathbf{r})^3 \mathrm{d}\mathbf{r}} = \frac{k_\mathrm{B} T}{2}, \tag{5.2}$$

where $V(\mathbf{r})$ is the potential energy from the trap. As the average potential energy of all atoms is $(3/2)k_\mathrm{B}T$, a recombination event leaves an excess energy of $1k_\mathrm{B}T$ in the remaining ensemble. By comparison with the average energy $3k_\mathrm{B}T$, a factor $1/3$ is obtained. This factor relates the relative heating rate $(\mathrm{d}T/\mathrm{d}t)/T$ with the relative loss rate $(\mathrm{d}N/\mathrm{d}t)/N$, which provides

$$\frac{\mathrm{d}T}{\mathrm{d}t} = \frac{T}{3N}\frac{\mathrm{d}N}{\mathrm{d}t} = \frac{\beta L_3}{3}\frac{N^2}{T^2}. \tag{5.3}$$

The two coupled differential equations describing the loss and heating rates have analytical solutions

$$N(t) = N_0 \left(1 + 3\beta \frac{N_0^2}{T_0^3} L_3 t\right)^{-1/3}, \tag{5.4}$$

$$T(t) = T_0 \left(1 + 3\beta \frac{N_0^2}{T_0^3} L_3 t\right)^{1/9}. \tag{5.5}$$

These expressions can thus be used to obtain L_3 from the temperature and atom number evolution of a system undergoing three-body recombination processes [89, 97].

This framework for analyzing losses and heating due to three-body recombination is now extended to mixtures. For a Bose mixture, many different loss channels can be significant, which complicates the differential equations. In a bosonic mixture of particles a and b, four different three-body recombination channels are present; a-a-a, a-a-b, a-b-b, and b-b-b, each with their own recombination coefficient L_3. The re-

sulting differential equation for one component a is

$$\frac{\mathrm{d}N_a}{\mathrm{d}t} = -\frac{2}{3}L_3^{aab}\int n_a^2 n_b \mathrm{d}^3r - \frac{1}{3}L_3^{abb}\int n_a n_b^2 \mathrm{d}^3r - L_3^{aaa}\int n_a^3 \mathrm{d}^3r - \frac{1}{\tau_a}\int n_a \mathrm{d}^3r. \tag{5.6}$$

Here, an additional term accounting for background losses was added, which contains the background lifetime τ_a of species a.

To evaluate heating, the two components are assumed to be rethermalized. First, one loss channel a-a-b is considered. Here, the mean potential energy α_{aab} of atoms undergoing three-body recombination has contributions from both components $\alpha_{aab} = \frac{2}{3}\alpha_a + \frac{1}{3}\alpha_b$ where $\alpha_a = \int n_a^2 n_b V_a \mathrm{d}^3r / \int n_a^2 n_b \mathrm{d}^3r$ and $\alpha_b = \int n_a n_b^2 V_b \mathrm{d}^3r / \int n_a n_b^2 \mathrm{d}^3r$. This leads to an excess energy per lost atom $\frac{3}{2}k_\mathrm{B}T - \alpha_{aab}$. To obtain the heating from the loss channel to the sample of $N_a + N_b$ atoms, this is compared the the average energy $3k_\mathrm{B}T$, which yields

$$\left[\frac{\mathrm{d}T}{\mathrm{d}t}\right]_{aab} = L_3^{aab}\frac{\frac{3}{2}k_\mathrm{B}T - \alpha_{aab}}{3k_\mathrm{B}}\frac{\int n_a^2 n_b \mathrm{d}^3r}{N_a + N_b}. \tag{5.7}$$

The total heating is the sum of heating rates from all channels

$$\frac{\mathrm{d}T}{\mathrm{d}t} = \left[\frac{\mathrm{d}T}{\mathrm{d}t}\right]_{aaa} + \left[\frac{\mathrm{d}T}{\mathrm{d}t}\right]_{aab} + \left[\frac{\mathrm{d}T}{\mathrm{d}t}\right]_{abb} + \left[\frac{\mathrm{d}T}{\mathrm{d}t}\right]_{bbb}. \tag{5.8}$$

The heating and losses of a bosonic mixture is thus described by three differential equations for N_a, N_b, and T, given by Eq. (5.6) and Eq. (5.8). The integrals in these equations can all be solved analytically, incorporating a gravitational sag, by assuming Gaussian thermal distributions. To obtain the three-body recombination coefficients in mixtures, the differential equations can be solved numerically and fitted to experimental data.

In a bosonic mixture, four different recombination coefficients thus have to be determined to properly analyze the losses. In the context of the relevant KRb mixtures, the coefficients for the single species channels have been determined in independent measurements [89, 177, 205]. Regarding the two remaining loss channels, the K-Rb-Rb channel is expected to be significantly stronger, since one light and two heavy atoms are stronger bound, compared to one heavy and two light [81, 116, 206]. To further favor this loss channel, the experiments were performed at approximately twice the number of Rb atoms compared to the number of K atoms. Consequently, the K-K-Rb channel is insignificant and can be neglected in the evaluation. Thus, the three-body recombination coefficient L_3^{KRbRb} for two Rb atoms and one K atom remains the only fitting parameter, besides initial temperature and atom numbers.

5.2 Controversy of Efimov Resonances in KRb Mixtures

The first experimental study of heteronuclear Efimov resonances claims the observation of three different features, detected through loss spectroscopy [117]. The first is from an Efimov state of two ^{87}Rb atoms and one ^{41}K atom, detected at an interspecies scattering length of $-246a_0$. The next is a feature from another Efimov state of one ^{87}Rb atom and two ^{41}K atoms, which is observed at $-22\times10^3 a_0$. Finally, a loss feature is observed at $667a_0$, which is claimed to originate from the presence of an atom-dimer resonance.

These observations turned out to be controversial for a multitude of reasons. The experiments were performed at a temperature of 300 nK, which determines the upper limit of interactions to be $|a|\sim 3200a_0$ [88]. Therefore, the observation of an Efimov resonance at $-22\times10^3 a_0$ should not be possible. Furthermore, the reported position of the Efimov resonances disagreed with later theoretical predictions of the three-body coefficient [116]. Moreover, the position of the atom-dimer resonance at $667a_0$ had an unexpected scaling with the position of the resonance at $-246a_0$ [127]. Additionally, the reported value of the three-body re-

combination coefficient differed significantly from theoretical calculations [127].

After the original observation, several studies were performed in a mixture of ^{40}K and ^{87}Rb [121, 207]. Theoretically, replacing the ^{41}K atom of a KRbRb Efimov trimer with a different isotope should only introduce minor changes to its properties. However, no Efimov resonance was observed [121]. An atom-dimer resonance was observed, but only by associating ^{40}K^{87}Rb dimers before decay measurements, and its position differed significantly from the observed feature at $667a_0$ [121, 207]. By employing universal scaling to the position of the observed atom-dimer resonance, a possible position of an Efimov resonance was predicted, but this position was also inconsistent with the initial observation [121].

A number of experimental studies was later conducted in ^{6}Li-^{133}Cs mixtures [85]. In general, these results were in agreement with theory, in contrast to the results from the ^{41}K-^{87}Rb mixture.

These many disputes were a major motivation for our investigation of three-body physics in ^{39}K^{87}Rb and ^{41}K^{87}Rb mixtures. The experimental apparatus presented in this thesis allows multiple isotopic combinations to be examined, which as an ideal prospect for studying Efimov physics.

5.3 Loss Spectroscopy of KRb Mixtures

The experimental procedure to prepare ultracold mixtures is presented in Chapter 3. For ^{39}K ^{87}Rb, the atoms are prepared in the $|F = 1, m_F = -1\rangle$ state, and the Feshbach resonance at 117.56 G is utilized to tune the scattering length. To measure the atom number and temperature evolution, the atoms are held in the optical dipole trap with trapping frequencies $\omega_\rho/2\pi = 118$ Hz (84 Hz) and $\omega_z/2\pi = 164$ Hz (111 Hz) for ^{39}K (^{87}Rb).

The mixtures of ^{41}K^{87}Rb are prepared similarly, but with both species in the $|1, 1\rangle$ state, where two Feshbach resonances are used. A broad resonance at 38 G is mainly used, but since it does not grant interactions in the range 0–$640a_0$, an additional resonance at 79 G is utilized to address these interactions [208].

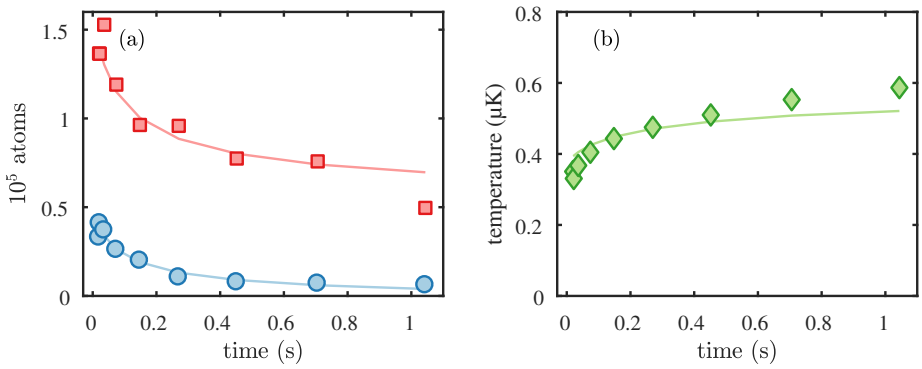

Figure 5.1: Measurement of atom number and temperature evolution of a mixture of ^{39}K and ^{87}Rb with an interspecies interaction of approximately $-880a_0$. (a) Atom number of ^{87}Rb (red squares) and ^{39}K (blue circles). (b) Temperature of the sample. The curves are fits of numerically evaluated coupled differential equations used to extract L_3^{KRbRb}, which are presented in text. The figure is based on data also presented in [27].

In a typical measurement to obtain the three-body recombination coefficient, 1.5×10^5 Rb and 0.5×10^5 K atoms are prepared at approximately 350 nK at weak interactions. The magnetic field is then rapidly changed to obtain a desired interaction strength, and the atoms are held in the trap at this interaction for a variable time. The atoms are then released from the trap, and atom numbers and temperatures are obtained by absorption imaging after 14 and 16 ms time-of-flight for K and Rb, respectively. To match the varying time scale of the decay rate across all interactions, the hold time at each scattering length is adjusted accordingly. During decay, the atoms are held in a trap of frequencies $\omega_\rho/2\pi =$ 124 Hz (89 Hz) and $\omega_z/2\pi = 170$ Hz (119 Hz) for ^{41}K (^{87}Rb).

In Fig. 5.1, a typical measurement series for ^{39}K and ^{87}Rb is shown. The atoms are held at a field corresponding to approximately $-880a_0$, which results in rapid decay of atom numbers and heating. The three data sets are fitted simultaneously by a global fit using Eq. (5.6) and (5.8), which determines the three-body recombination coefficient L_3^{KRbRb}. The fits describe the atom losses well, but do not fully capture the heating. One possible additional source of heating is the kinetic energy gained

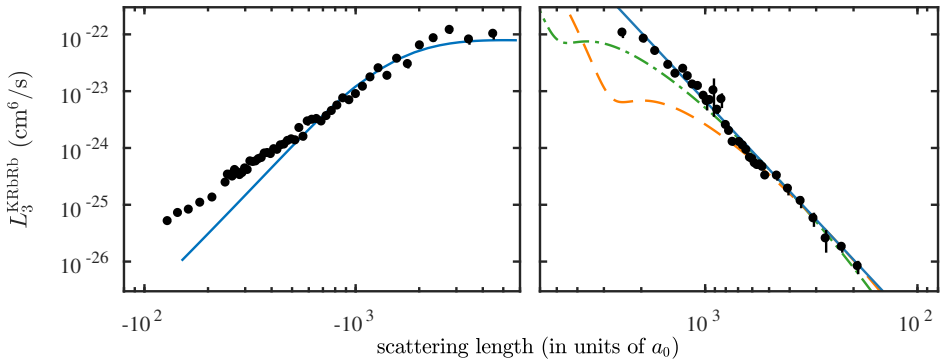

Figure 5.2: Three-body recombination coefficient for a mixture of ^{39}K and ^{87}Rb at different interaction strengths. The solid blue line at negative scattering lengths is from the optical model presented in text, assuming no Efimov resonance. At positive scattering lengths, the blue curve is a a^4 fit, which is used to produce theory curves with trial recombination minima at $2800a_0$ and $5100a_0$, shown in dashed orange and dash-dotted green, respectively. The figure is based on data from [27].

by the atoms undergoing recombination, which can be partially redistributed to the remaining ensemble before they leave the trap.

5.3.1 Three-Body Losses in ^{39}K ^{87}Rb

Decay measurements are performed in a broad range of both positive and negative interspecies interactions for a mixture of ^{39}K and ^{87}Rb. The evaluated three-body recombination coefficients are shown in Fig. 5.2. The scattering length at the different magnetic fields is modeled from RF molecule association spectroscopy which determines the scattering length through the binding energy $E_\mathrm{b} = \hbar^2/2m_\mathrm{r}a^2$, in combination with the characterization performed in Sec. 4.1.

On both sides of the Feshbach resonance, the three-body recombination coefficient increases as $L_3^{\mathrm{KRbRb}} \sim a^4$. At strong interactions, this scaling is limited at $\pm 2000a_0$ by the temperature of the sample, whereas the scaling at weak interactions is limited by the finite range of the two-

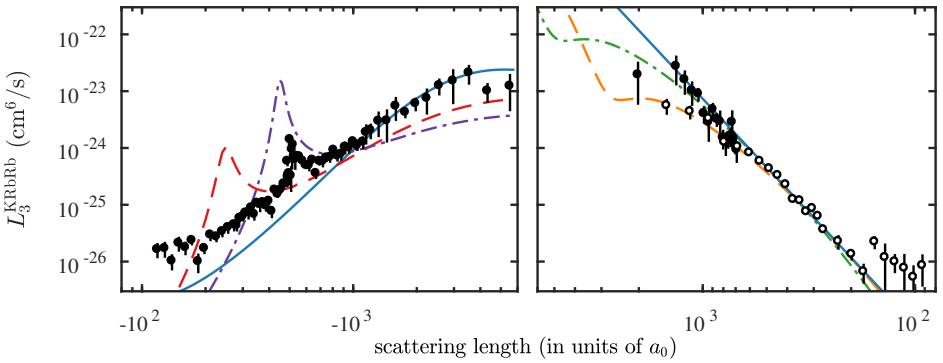

Figure 5.3: Three-body recombination coefficient for a mixture of ^{41}K and ^{87}Rb at different interaction strengths. The open circles are from measurements performed at the Feshbach resonance at 79 G, while the remaining data is from measurements at the Feshbach resonance at 38 G. At negative scattering lengths, theory curves produced by the optical model introduced in text is shown assuming no Efimov resonance in solid blue, a resonance at $-246a_0$ in dashed red, and a resonance at $-500a_0$ in dash-dotted purple. At positive scattering lengths, the blue curve is a a^4 fit, which is used to produce theory curves with trial recombination minima at $2800a_0$ and $5100a_0$, shown in dashed orange and dash-dotted green, respectively. The figure is based on data from [27].

body potential determined by the van der Waals radius R_{vdW} introduced in Sec. 2.2.

Besides the a^4-scaling, no significantly enhanced losses which can be interpreted as an Efimov resonance are observed. Furthermore, no suppression of losses due to a recombination minimum at positive interactions are observed.

5.3.2 Three-Body Losses in ^{41}K^{87}Rb

In a mixture of ^{41}K and ^{87}Rb, similar decay measurements are performed in a similarly broad range of interactions, with the resulting three-body recombination coefficients shown in Fig. 5.3. The scattering length is here obtained from a model for the full molecular potential [209].

As for the ^{39}K ^{87}Rb mixture, the recombination scales with approximately a^4 on both sides of the Feshbach resonance. In this isotopic

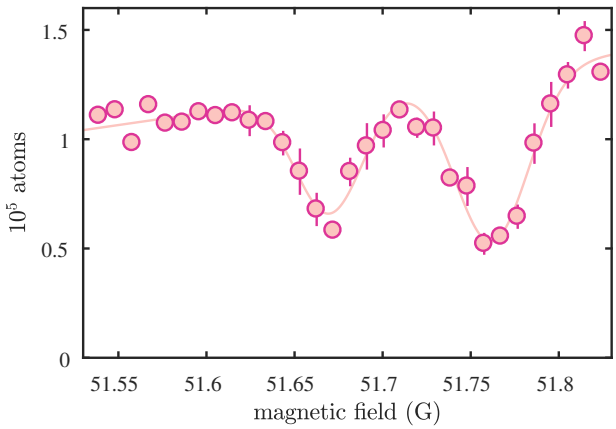

Figure 5.4: Loss spectroscopy of a p-wave Feshbach resonance. The total atom number after a short hold time show a double peak structure. The curve is a fit of two Gaussians and a linear background. This figure is based on data from [27].

mixture, we additionally observe a loss feature at approximately $-500a_0$. To better resolve this feature, additional collisional spectroscopy is performed, which resolves a double peak structure as shown in Fig. 5.4. This is characteristic of a p-wave Feshbach resonance, and, indeed, theoretical calculations predict such a resonance at this position [208]. Besides this, no additional features are observed which can be identified as either an Efimov resonance or a recombination minimum.

5.3.3 Discussion

To evaluate the results, the measurements of L_3^{KRbRb} are compared to theoretical models. At negative scattering lengths, we employ a framework based on an optical model approach, which has an imaginary potential at short distances [206]. To account for the finite temperature, recombination at all energies are considered, and the results are convoluted with a Boltzmann distribution corresponding to the temperature. The model is both used to predict the three-body recombination coefficient with and without assuming the presence of an Efimov resonance. In Fig. 5.2, no Efimov resonance is assumed, and in Fig. 5.3, the-

oretical results are shown, both without a resonance, with a resonance at $-500a_0$, and with a resonance at $-246a_0$. These values correspond to the approximate position of the p-wave resonance, and to the position of the originally claimed observation of a KRbRb resonance [117].

For both isotopic combinations, the optical model matches the experimental data well, when assuming no Efimov resonances. At lower interactions, the agreement lessens, since the model does not take the details of the interatomic potential into account. When assuming the presence of an Efimov resonance, the model is clearly unable to account for the experimental observations.

At positive scattering lengths, a simple a^4 fit is performed for both isotopes. Based on this fit, trial theory curves are plotted, assuming predicted recombination minima at $2800a_0$ [116] and $5100a_0$ [121], using Eq. (2.49) with $\eta_+ = 0.02$. This indicates that recombination minima at large interaction strengths are indeed possible, but an unambiguous observation requires significantly lower temperatures.

In two other studies, atom-dimer resonances were observed at $230a_0$ for ^{40}K^{87}Rb [121] and at $360a_0$ for ^{41}K^{87}Rb [122]. By employing universal scaling, these observations can be used to predict possible positions of Efimov resonances. The observed atom-dimer resonances thus provide positions of -55×10^3a_0 and -91×10^3a_0, which is beyond the range of interactions studied here. The more deeply bound Efimov states are similarly predicted to have resonances at -450×10^3a_0 and -690×10^3a_0. Our data does not show any features near these interactions.

The main uncertainties in this experiment are systematic errors in atom number and scattering length. An uncertainty in atom number propagates into L_3^{KRbRb}. These types of errors do however only slightly shift the spectrum in Fig. 5.2 and 5.3, and cannot change the outcome that no spectroscopic features of Efimov resonances are observed at intermediate scattering lengths.

To summarize, the three-body recombination coefficient was determined over a range of 4 orders of magnitude for positive and negative interactions in mixtures of ^{39}K ^{87}Rb and ^{41}K^{87}Rb. For negative scattering lengths, the observations are in agreement with a theoretical model, and do not indicate the presence of any Efimov resonances. This resolves a

debate regarding three-body physics in ultracold gases and contribute to the understanding of mass-imbalanced few-body systems.

5.4 Temperature Dependence of an Efimov Resonance in ^{39}K

In this section, a study of the temperature dependence of an Efimov resonance in ^{39}K is presented [28]. The results are preliminary, the evaluation is work in progress, and the experimental observations are not yet fully understood.

Efimov resonances have been observed in ^{39}K several times [89, 97]. Motivated by the realization that the observation of the second Efimov resonance was, in theory, within the capability of the experimental apparatus, a series of measurements was initiated. However, when performing measurements at different temperatures, an unexpected behavior of the first Efimov resonance was observed. Since the temperature dependence of an Efimov resonance has only been examined experimentally once [114], and given a remarkable behavior, further measurements and evaluations were conducted, which are presented here.

5.4.1 Experimental Procedure

The Efimov resonance is characterized by performing a series of decay measurements, covering a range of interactions, at different initial temperatures. An inherent technical problem when performing experiments at specific interaction strengths near a Feshbach resonance, is the finite speed at which the magnetic field can be changed. Losses and other dynamical processes can initiate while the magnetic field is approaching its target value. To circumvent this issue, a new preparation procedure was used in this experimental study.

The starting point for a measurement is an ultracold sample of ^{39}K atoms in the $|1,-1\rangle$ state held in the optical dipole trap, prepared as outlined in Chapter 3. The final preparation at the desired temperature and interaction strength is shown schematically in Fig. 5.5(a). The evaporation to a final temperature is performed at positive interactions, near

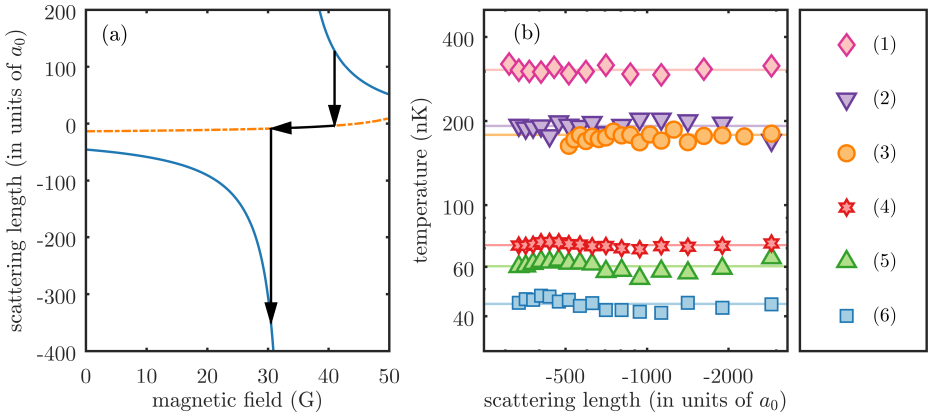

Figure 5.5: (a) Schematic procedure for preparing ^{39}K atoms at a specific temperature and interaction strength. The blue curves describe the interaction strength in the $|F = 1, m_F = -1\rangle$ state, while the dash-dotted orange curve is the interaction strength in the $|1,0\rangle$ state. (b) The resulting initial temperature for the different data series. The labels (1)–(6) in the legend refer to the information provided in Tab. 5.1 and data shown in Fig. 5.6. The initial temperatures at the different interactions are obtained through a fit. The solid lines are the initial temperature $\overline{T}_0$ averaged across all interactions, and shown in Tab. 5.1. This data is also presented in [28].

the Feshbach resonance at 33.6 G. The Efimov resonance is located near the Feshbach resonance at negative interactions. Subsequent to evaporation, the atoms are transferred to the $|1,0\rangle$ state, and the magnetic field is ramped to a target value. To ensure that the field is fully stabilized before initiating a measurement, the atoms are held at 0.5 s at this target field. A decay measurement is then started by transferring the atoms back to the $|1,-1\rangle$ state. The procedure ensures that the atoms are not subjected to strong interactions prior to the measurement, and thus ensures a low initial temperature independent of the interaction strength of the target magnetic field.

A decay measurement is performed by holding the sample for a variable amount of time and recording the temperature and atom number evolution through absorption imaging after 20 ms expansion. When the

Table 5.1: Information of the different data series used to characterize the ^{39}K Efimov resonance. The labels (1)-(6) refer to the data shown in Fig. 5.5(b) and Fig. 5.6. The different columns in the table show: average initial temperature $\overline{T}_0$ obtained from decay fits, the trap frequencies ω_i ($i = x, y, z$) during the decay measurements, average initial atom number $\overline{N}_0$ obtained from decay fits, average initial densities $\overline{n}_0$ obtained from decay fits, and the preparation method for entering the $|1,-1\rangle$ state. This data is also presented in [28].

	$\overline{T}_0$ (nK)	$\omega_i/2\pi$ (Hz)	$\overline{N}_0/10^3$	$\overline{n}_0/10^{12}$ (cm^{-3})	preparation
(1)	304(9)	83, 109, 83	34(5)	0.77(12)	ramp
(2)	192(9)	86, 114, 86	20(3)	1.00(17)	sweep
(3)	178(11)	83, 109, 83	23(2)	1.16(11)	sweep
(4)	71.7(1.3)	90.5, 28, 79	70(2)	3.71(12)	pulse
(5)	60(3)	89, 25, 75	48(7)	2.78(4)	pulse
(6)	44(3)	87, 21, 70	26(2)	1.77(13)	pulse

atoms are released from the trap, the magnetic field is simultaneously turned off.

Each decay measurement is analyzed by synchronously fitting atom number and temperature evolution to Eq. (5.4) and Eq. (5.5). This provides the three-body recombination coefficient L_3^{K}, as well as the initial atom number and temperatures shown in Fig. 5.5(b) and Tab. 5.1. The experimental procedure ensures an initial temperature which is approximately constant across the relevant range of interactions. To obtain the different initial temperatures, traps of different geometries are necessary, and the resulting initial atom numbers and densities vary across the different data sets. To test the influence of the preparation scheme, both π-pulses and rapid adiabatic passages are tried, and for one of the data sets, the magnetic field is ramped directly to its target value while the atoms are in the $|1,-1\rangle$ state. All the relevant information about the individual data series is provided in Tab. 5.1.

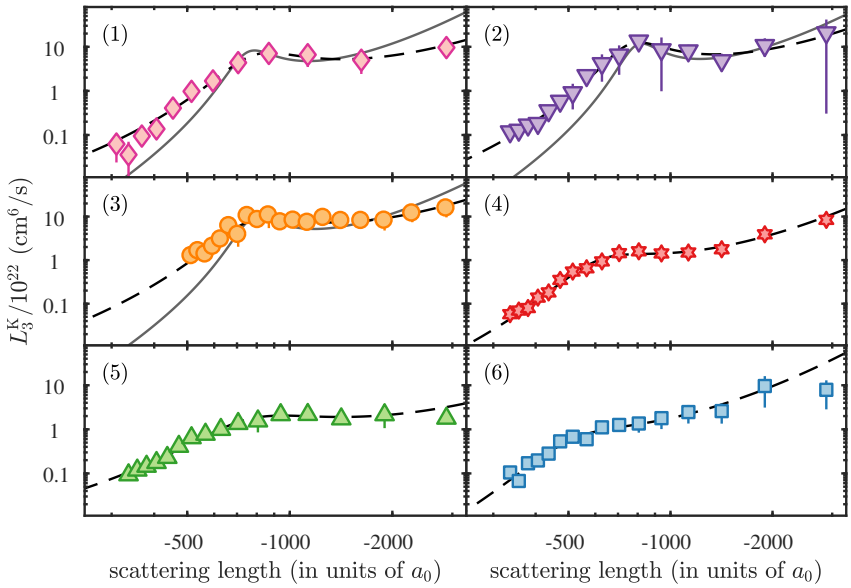

Figure 5.6: Three-body recombination coefficients at different temperatures and interactions. The labels (1)-(6) and symbols shown in the different panels refer to the data shown in Fig. 5.5(b) and in Tab. 5.1. The gray solid lines are fits to Eq. (5.9) and the black dashed lines are fits to Eq. (5.10). This data is also presented in [28].

5.4.2 Temperature Dependence of the Efimov Resonance

The obtained three-body recombination coefficients L_3^K at different interactions are shown in Fig. 5.6 for all the data series. The scattering lengths are obtained through the Feshbach parameters provided in reference [97]. Independent of temperature, the data sets yield approximately the same recombination coefficient at low values of $|a|$, and, as expected, it increases as $|a|$ increases. For high temperatures, a peak structure in the recombination coefficient is observed at approximately $a_- = 800\,a_0$, which is a clear signature of an Efimov resonance. This data also agrees well with a previous observation of an Efimov resonance at this Feshbach resonance [97]. However, for the data acquired at low temperatures, the appearance of the resonance changes, and it clearly becomes less pronounced.

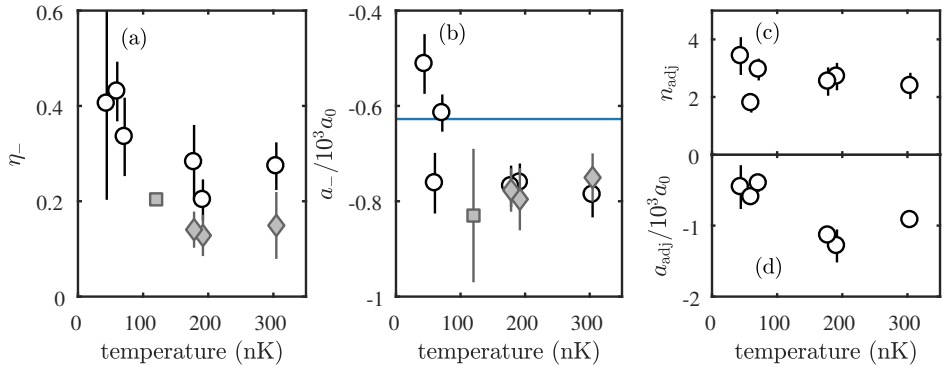

Figure 5.7: Efimov resonance parameters for different temperatures. (a) The decay parameter which describes the Efimov resonance width. (b) The resonance position. (c-d) Parameters obtained from empirical fit. Gray diamonds are from fits to Eq. (5.9) and black circles are from fits to Eq. (5.10), while the gray squares are from reference [97]. This data is also presented in [28].

The shape of the Efimov resonance and its dependence on temperature is quantified by implementing a fit using Eq. (2.49) and Eq. (2.29)

$$L_3^{\mathrm{K}}(a) = 4590\frac{3\hbar a^4}{m}\frac{\sinh(2\eta_-)}{\sin^2\left[s_0\ln\left(a/a_-\right)\right]+\sinh^2\eta_-}. \tag{5.9}$$

The fit is applied for high temperatures and captures the position of the Efimov resonance, but it fails for low temperatures. The fit also fails to describe the three-body recombination coefficient at low $|a|$, which is a trend that has also been observed previously [27, 90, 97].

Therefore, an empirical fit is introduced, based on Eq. (2.49) and Eq. (2.29), but with additional empirical fitting parameters a_{adj} and n_{adj} which infer a more flexible fit

$$L_3^{\mathrm{K}}(a) = 4590\frac{3\hbar a_{\mathrm{adj}}^4}{m}\left(\frac{a}{a_{\mathrm{adj}}}\right)^{n_{\mathrm{adj}}}\frac{\sinh(2\eta_-)}{\sin^2\left[s_0\ln\left(a/a_-\right)\right]+\sinh^2\eta_-}. \tag{5.10}$$

This fit is applied to all the data sets and describes the obtained recombination coefficients well at all interactions.

Through the two different fits, the appearance of the Efimov resonance is quantified through the obtained parameters a_- and η_- which

are shown in Fig. 5.7(a-b). The decay parameter η_-, which describes the lifetime of the trimer and the width of the resonance, increases with decreasing temperature. The position of the resonance a_- also changes with temperature. For low temperatures, the observed positions tend to agree well with the universal prediction $a_- \approx -9.73 R_{\mathrm{vdW}}$ [98, 99], for $R_{\mathrm{vdW}} = 64.49 a_0$ [97]. The result from a previous observation on this resonance [97] is also shown in 5.7(a-b), and is in agreement with the new observations presented.

In Fig. 5.7(c-d), the obtained empirical fitting parameters a_{adj} and n_{adj} are shown. To fit the recombination coefficients at low $|a|$, the exponent n_{adj} tends to deviate from the simple universal a^4 scaling.

The temperature dependence of an Efimov resonance in Cs has previously been studied [114]. Here, a decrease of the apparent position of $|a_-|$ was observed as well, although the analysis was slightly more comprehensive. However, the Efimov resonance becomes more pronounced at low temperatures, which is a behavior opposite to the observations presented in Fig. 5.6 and 5.7.

This disappearance of the resonance at low temperatures is highly surprising and the physical origin is unknown. The results presented here are preliminary and fully understanding them is work in progress.

CHAPTER 6

OBSERVATION OF POLARONS IN A BOSE-EINSTEIN CONDENSATE

A polaron is a quasiparticle, formed by an impurity and its interaction with a surrounding medium. It is an important example of an impurity particle interacting with its environment, which is a scenario found in many areas of physics. It is therefore interesting to study the polaron in the versatile setting offered by ultracold quantum gases. The topic is introduced in more detail in Sec. 2.6.

In this chapter, the first experimental observation of polarons in a Bose-Einstein condensate is presented. The results were published in parallel with a similar study from JILA [17, 133].

This chapter is structured as follows. In Sec. 6.1, the approach used in this experimental study of the Bose polaron is introduced. A characterization of the relevant Feshbach resonance is presented in Sec. 6.2 and the detailed experimental procedure for detecting the polaron is outlined in 6.3. The observed polaron spectrum is shown and discussed in Sec. 6.4, and in Sec. 6.5, the effect of varying the polaron fraction is examined.

For the repulsive polaron branch, a discrepancy between experimental observations and theoretical calculations is found. This discrepancy is accounted for in Sec. 6.6, where various effects not included in the theory and in the experimental evaluation are discussed [18]. A cooling effect observed in the polaron spectrum is presented and explained in Sec. 6.7, and finally, the results of this chapter are summarized in Sec. 6.8.

6.1 Experimental Approach

The ideal generic study of the polaron requires a system of one or few impurities immersed in a homogeneous medium, a setting which is difficult to realize in an ultracold quantum gas. Typically, the experimental atom trap is harmonic, resulting in an inhomogeneous density distribution. The ultracold gas then has to consist of two components; a minority component where the individual particles can be considered as impurities, and a majority component which operates as an interacting medium for the impurities. The two components can be either different species or different spin states of the same species.

In mixtures of ultracold Fermi gases, the Pauli pressure ensures that a minority component can reside entirely within the central region of a majority component and thereby exist in a region of the medium of approximately homogeneous density. This is not the case for the typical condensed bosonic mixtures. As discussed in Chapter 4, the Thomas-Fermi radii of two Bose-Einstein condensates of different species can be on the order of the relative gravitational sag. Even if two condensates have similar trap centers, the shapes of their density profiles are not trivial, as shown in Fig. 4.4.

One approach to study Bose polarons with the experimental setup presented in this thesis would be to use ^{39}K and ^{87}Rb as the two components. But due to the inherent problems of Bose mixtures presented above, another approach was developed. The starting point is a single Bose-Einstein condensate in a state $|1\rangle$. Then, a weak RF pulse transfers a small fraction of atoms into another state $|2\rangle$, which interacts with the condensate in state $|1\rangle$ through a Feshbach resonance. A spectroscopy thus simultaneously creates and probes the impurities. The overlap be-

tween the two components is simple to model through the Thomas-Fermi distribution, and the impurities are prepared with zero momentum, which provides a more straightforward comparison with theory.

The two states $|1\rangle$ and $|2\rangle$ can be depicted by a Bloch sphere, where the RF pulse performs a minor rotation. However, once the rotation is performed, the interaction strengths between $|1\rangle$ and $|2\rangle$ atoms rapidly decohere the system, and the actual spectral function which is probed is equivalent to that of the polaron [17]. Strictly speaking, the Bloch sphere picture is only correct if the two states are non-interacting.

The approach presented here constitutes a new method of studying polarons. In fact, this approach is not even possible in a fermionic system. In a Fermi gas subject to a RF pulse in a similar manner, the Pauli principle suppresses interactions [210].

A requirement is a Feshbach resonance between two different states. Only very narrow single-species Feshbach resonances are available for ^{87}Rb [37]. The same is the case for ^{41}K [32]. Fortunately, a theoretically predicted Feshbach resonance was identified for ^{39}K, which allowed the scattering length between atoms in the states $|F = 1, m_F = -1\rangle$ and $|1, 0\rangle$ to be tuned [36]. As shown in Fig. 1.1(b), the resonance is located in a region where the scattering length between atoms in the $|1, -1\rangle$ state is approximately constant. This allows the initial Bose-Einstein condensate to be produced in this state. Furthermore, the magnetic field can be chosen arbitrarily in the relevant range of interactions, without affecting the internal interactions of the condensate significantly.

The expected energy spectrum of the polaron is shown in Fig. 6.1. The atoms are initially in the hyperfine state $|1\rangle \equiv |1, -1\rangle$. A RF pulse transfers a small fraction of atoms into the state $|2\rangle \equiv |1, 0\rangle$, and the transition frequency is altered by the interaction with the condensate atoms in the initial state. This results in repulsive and attractive polaron states with energies E_r and E_a, respectively. Additionally, a molecular state is present with energy E_m. Towards strong interactions, a many-body continuum appears at higher energies, corresponding to excited polaron states. Furthermore, the repulsive polaron branch is broadened and will eventually become damped, since it can decay to lower-lying states.

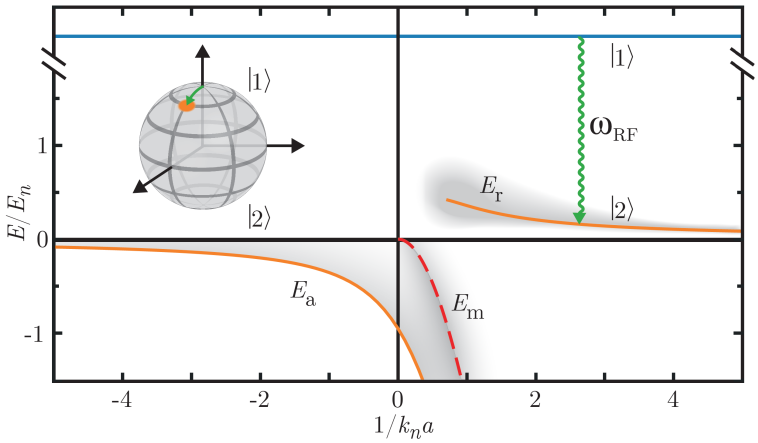

Figure 6.1: Sketch of the expected spectrum of an impurity in a Bose-Einstein condensate and the spectroscopic approach to experimentally obtain this. A RF pulse transfers atoms from the $|1\rangle$ to the $|2\rangle$ state, corresponding to a small rotation on a Bloch sphere. The energies of the attractive and repulsive polaron branches are shown as lines labeled E_a and E_r, respectively. The dashed line labeled E_m is the molecular state. The grey shading denote a broadening of the spectrum due to the many-body continuum and the finite lifetime of the repulsive polaron. More details are given in text. A similar figure was published in [17].

The interaction scale $1/k_n a$ is determined by the impurity-boson scattering length a and the Fermi wave number

$$k_n = (6\pi^2 n)^{1/3}, \tag{6.1}$$

where n is the density of the medium. The corresponding energy scale is

$$E_n = \frac{\hbar^2 k_n^2}{2m}, \tag{6.2}$$

where m is the boson mass, which for this study is the same as the impurity mass.

In the parallel study from JILA a different approach was used. A mixture of bosonic ^{87}Rb and fermionic ^{40}K was utilized, where the fermions were used as impurities. The Pauli pressure of the fermions provided both a low density and a large size of the cloud, which ensured spatial overlap with the Bose-Einstein condensate of ^{87}Rb.

6.2 Charactarization of the Feshbach resonance

In this section, measurements to characterize the Feshbach resonance for the study of Bose polarons are presented. The zero-crossing of the Feshbach resonance is determined through rethermalization measurements of the two magnetic substates. To determine the position and the background scattering length, a molecular spectroscopy is performed.

6.2.1 Detection of Zero-Crossing

A measurement of a scattering length zero-crossing created by a Feshbach resonance was presented in Sec. 4.1, where ^{87}Rb was cooled selectively, and ^{39}K sympathetically. Due to the gravitational sag, ^{87}Rb is preferentially evaporatively cooled when lowering the power of the optical dipole trap.

The same method is not immediately applicable to determine the rethermalization of two spin components of ^{39}K, since they are evaporated similarly when lowering the trap power. As a solution, the Ioffe coil, which is used to form the QUIC trap, is utilized to apply a magnetic field gradient, which the two components react differently to. It is thus possible to selectively cool one component.

The starting point for the measurement is a thermal cloud of ^{39}K in the optical dipole trap in the $|1,-1\rangle$ state. The sample is held in a homogeneous magnetic field in the vicinity of the expected position of the zero crossing. The mixture is prepared by applying a RF pulse, transferring a majority of the atoms to the $|1,0\rangle$ state. Subsequently, a current is sent through the Ioffe coil to create the magnetic field gradient. The current is linearly increased over the duration of some seconds. The gradual increase of the magnetic field gradient results in evaporative cooling of atoms in the $|1,-0\rangle$ state. Naively, one could expect atoms in the $|1,-1\rangle$ state to be primarily removed, since it is the only component sensitive to the linear Zeeman effect. However, the experiment is performed at relatively large magnetic fields, in the regime of the nonlinear Zeeman effect.

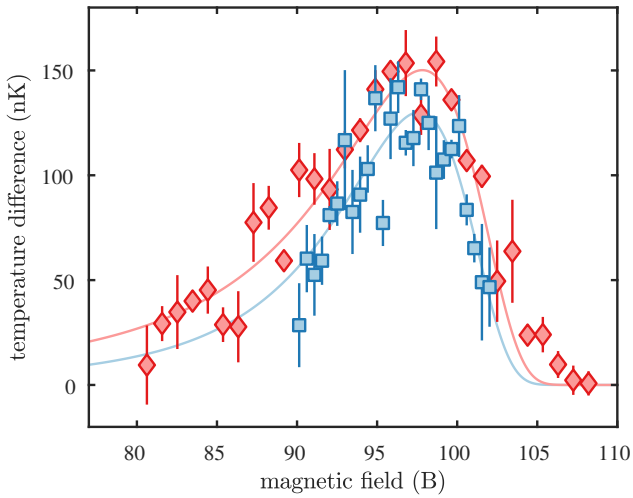

Figure 6.2: Rethermalization of a mixture near zero-crossing of a Feshbach resonance. The temperature difference after 5 sand 10 s is shown as red diamonds and blue squares, respectively. This data was also presented in [211].

Here, the $|1,0\rangle$ atoms react more strongly to the magnetic field gradient and are thus primarily removed from the trap.

After the selective evaporation, the current through the Ioffe coil is ramped down to remove the magnetic field gradient, and the homogeneous magnetic field is adjusted to a desired value, where the two components are held for a set amount of time. Finally, the two components are released from the trap, separated in time-of-flight by a magnetic field gradient, and imaged.

The obtained temperature difference of the two components for two different hold times is shown in Fig. 6.2. For long hold times, the rethermalization signal narrows since the two samples rethermalize more. The rethermalization rate in this specific measurement is however low due to small atom numbers. To determine the position of the zero crossing, Eq. (4.1) is used to fit the two data sets, which yields a position of 97.9(2) G.

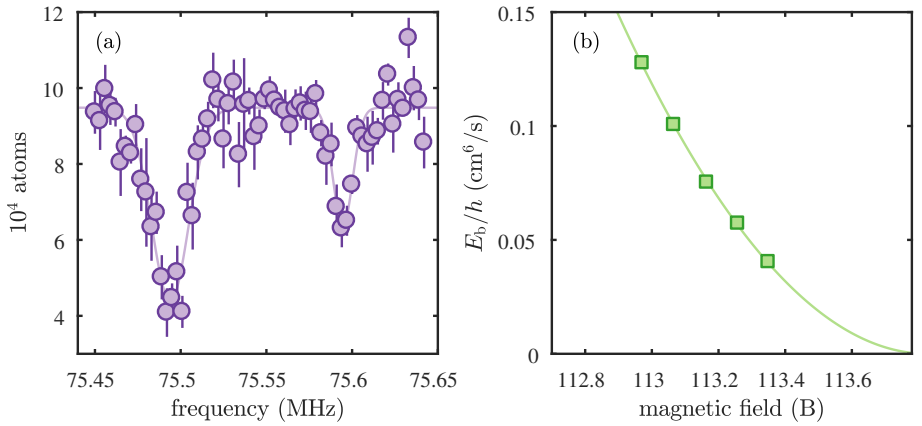

Figure 6.3: Molecular spectroscopy near a Feshbach resonance. (a) Number of remaining atoms in initial state after a RF pulse was applied at a magnetic field of 113.06 G. The left feature is the bare transition, and the right feature is the transition to the molecular state. (b) The obtained binding energy at different magnetic fields and the fit which determines the scattering length. Similar data was also presented in [211].

6.2.2 Molecular Spectroscopy

The scattering length near a Feshbach resonance is determined by the energy of the bound molecular state. A spectroscopy of this state is thus a useful method to determine the scattering length.

To perform the molecular spectroscopy, a thermal sample of ^{39}K is prepared in the optical dipole trap in the $|1,-1\rangle$ state, at a magnetic field near the position of the Feshbach resonance. Then, a RF pulse is radiated for up to several ms, close to the transition from $|1,-1\rangle$ to $|1,0\rangle$. Subsequently, the atoms are released from the trap and the number of atoms remaining in the $|1,-1\rangle$ state is recorded.

An example of a molecule spectroscopy is shown in Fig. 6.3(a), where the number of atoms in the initial state $|1,-1\rangle$ is shown. The signal displays two spectroscopic features. The first is the bare transition to the $|1,0\rangle$ state, whereas the second is the molecular state associated with the Feshbach resonance. The first peak can be used to determine the magnetic field, and the separation between the two peaks corresponds

to the binding energy E_b of the molecule. The positions of the peaks are obtained by performing a fit with two Gaussians.

The binding energy at different fields is shown in Fig. 6.3(b). This energy is related to the scattering length provided by the Feshbach resonance through

$$E_b = \frac{\hbar^2}{4mR^{*2}}\left(\sqrt{1+4R^*/a}-1\right)^2, \tag{6.3}$$

where R^* is associated with the strength of the resonance [8, 17]. This parameter is estimated to be $60a_0$, based on reference [36].

To obtain an expression for the scattering length, the typical relation $a(B) = a_{bg}[1-\Delta_F/(B-B_0)]$ is assumed, and a fit using the expression for the binding energy above is performed, while fixing the zero crossing to be 97.9 G. The resulting fit is shown in Fig. 6.3(b), and yields $B_0 = 113.78$ G, $\Delta_F = -15.88$ G, and $a_{bg} = -45.34a_0$.

6.3 Polaron Spectrocopy Procedure

For a polaron spectroscopy, atoms of ^{39}K are prepared in the optical dipole trap in the $|1,-1\rangle$ state, as outlined in Chapter 3. The state preparation path from $|2,2\rangle$ to $|2,-2\rangle$ to $|1,-1\rangle$ ensures that no atoms are initially in the impurity state $|1,0\rangle$. The atoms are cooled evaporatively to degeneracy by lowering the power of the dipole trap. To enhance the rethermalization during evaporation, the magnetic field is kept in the vicinity of the Feshbach resonance at 33.6 G.

When the evaporative cooling is complete, the magnetic field is adjusted towards a desired value in the vicinity of the Feshbach resonance at 113.78 G. The magnetic field determines the interaction strength of the polarons created later in the procedure. The magnetic field produced by the apparatus takes a finite amount of time to settle. To assure that the magnetic field has stabilized when a spectroscopy is performed, the atoms are held for 0.5 s at the target field. During this waiting time, the power of the dipole trap is ramped up, which increases the density of the condensate. The reasoning behind increasing the density is explained in the following.

Prior to the observation of the Bose polaron, it was an open question whether it would even be well-defined, since three-body recombination with medium atoms was expected to severely limit its lifetime. One criterion in deciding if a polaron state is well-defined is to determine whether the energy of the state is larger than its broadening from its finite lifetime. The decay rate from three-body recombination of a Bose gas of intermediate interactions is proportional to n^2a^4, while the mean-field energy of a polaron is na. A certain polaron mean-field energy can be obtained either by increasing n or by increasing a, but increasing a has much greater impact on the decay rate. However, the density cannot be arbitrarily chosen like the scattering length, so it is still necessary to tune interactions via the Feshbach resonance. Note that perturbation theory predicts that n and a are not equivalent, as seen from Eq. (2.51). Based on these arguments, a condensate of high density was chosen for all interaction strengths.

Before the spectroscopy, the Bose-Einstein condensate consists of 2×10^4 atoms in the $|1\rangle$ state, at a temperature of approximately 160 nK corresponding to $T/T_c = 0.6$ in a trap of frequencies $(\omega_x,\omega_y,\omega_z)/2\pi = (158, 167, 228)$ Hz. The scattering length between the atoms of the condensate is $a_B \approx 9a_0$ [97], resulting in an average density of $2.3\times10^{14}\,\mathrm{cm}^{-3}$, a condensate interaction strength $k_n a_B \approx 0.01$, and an energy scale for the polaron of $E_n/h = 73$ kHz.

To create the polarons and perform the spectroscopy, a square RF pulse of frequency ω_{RF} with a duration of 100 µs is applied. Compared to the characterization described in Sec. 3.5, this corresponds to a Gaussian pulse of $\sigma_t \approx 50$ µs. This pulse does not provide the best possible resolution that the apparatus can currently provide. However, when the measurements presented in this chapter were performed, the magnetic field had not been stabilized to the same level of precision. The 100 µs pulse corresponds to the precision provided by the apparatus at the time. The relevant spectral width of the pulse at half maximum is $0.15E_n$.

After the pulse has been applied, the sample is held in the trap for a variable amount of time before the atoms are released to expand. During the initial expansion, the magnetic field is held at a constant value to avoid crossing a Feshbach resonance while the condensate has not yet diluted. After 5 ms, a magnetic field gradient is applied to spatially sep-

arate the two states for imaging. Finally, the magnetic field is turned off, and after a total expansion time of 23 ms, the atoms are imaged through absorption imaging.

No atoms are observed in the $|2\rangle$ state, except at weak interactions and short hold times, and the hold time was therefore set to 0 for most of the measurements. The interpretation is that the atoms undergo three-body recombination involving one $|2\rangle$ and two $|1\rangle$ atoms during the initial expansion, due to strong interactions. A bimodal fit is performed to atoms in the $|1\rangle$ state to obtain the number of remaining atoms in the Bose-Einstein condensate.

For an interaction strength $k_n a$, polaron spectroscopy is performed by measuring the number of condensate atoms remaining in the $|1\rangle$ state versus the detuning of the RF pulse $\Delta = \omega_0 - \omega_{\mathrm{RF}}$, where ω_0 is the unperturbed transition frequency. The power of the RF pulse is adjusted to yield a condensate atom loss which does not exceed approximately 30 %. Given that every impurity atom recombines with two medium atoms, this corresponds to an impurity fraction of 10 %. The bare transition ω_0 is recorded by performing spectroscopy of thermal clouds in the same range of magnetic fields as the polaron spectroscopy. Furthermore, the number of thermal atoms recorded from the polaron spectroscopy provides a signal which reproduces the measured position of ω_0.

An example of a polaron spectroscopy, and the corresponding reference spectroscopy of a thermal sample, is shown in Fig. 6.4. The signal in the polaron spectroscopy is clearly shifted and broadened compared to the bare transition.

The theoretically expected lineshape of the polaron spectroscopy is unique at every interaction strength and the theory does therefore not provide a general fitting function for the experimental data. Hence, a Gaussian fit is applied, which captures the lineshape well throughout the spectrum. This fit is used to obtain the number of atoms in the condensate before the pulse, the maximum loss, the width of the spectrum, and the average energy of the spectrum.

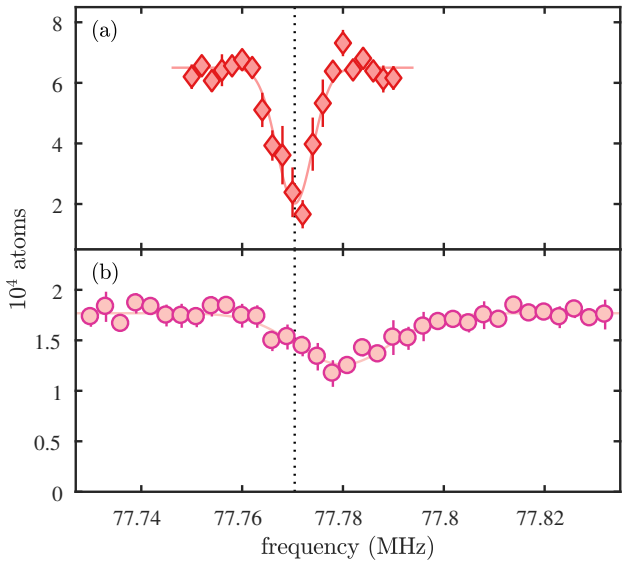

Figure 6.4: Polaron spectroscopy at $1/k_n a = -1.6$. (a) Reference spectroscopy with thermal atoms. (b) Polaron spectroscopy with a Bose-Einstein condensate, clearly displaying a shift in signal position. This figure is based on data presented in [17].

6.4 Spectrum of the Bose Polaron

The obtained polaron spectroscopy signal is shown in Fig. 6.5(a) which displays the normalized number of lost condensate atoms, and a theoretically obtained spectrum is shown in Fig. 6.5(b) for comparison. The theory is briefly outlined in the following, and subsequently the results are discussed in detail.

The theoretical spectrum is obtained from a numerical method that calculates the spectral function for a zero-momentum impurity, including three-body correlations. The relevant Hilbert space in the system consists of the wave function of the impurity and of the Bose-Einstein condensate perturbed by the impurity. The theoretical method applied here restricts this space to wave functions containing the impurity, the unperturbed Bose-Einstein condensate, and two Bogoliubov excitations of the condensate. This truncated basis method is similar to a variational

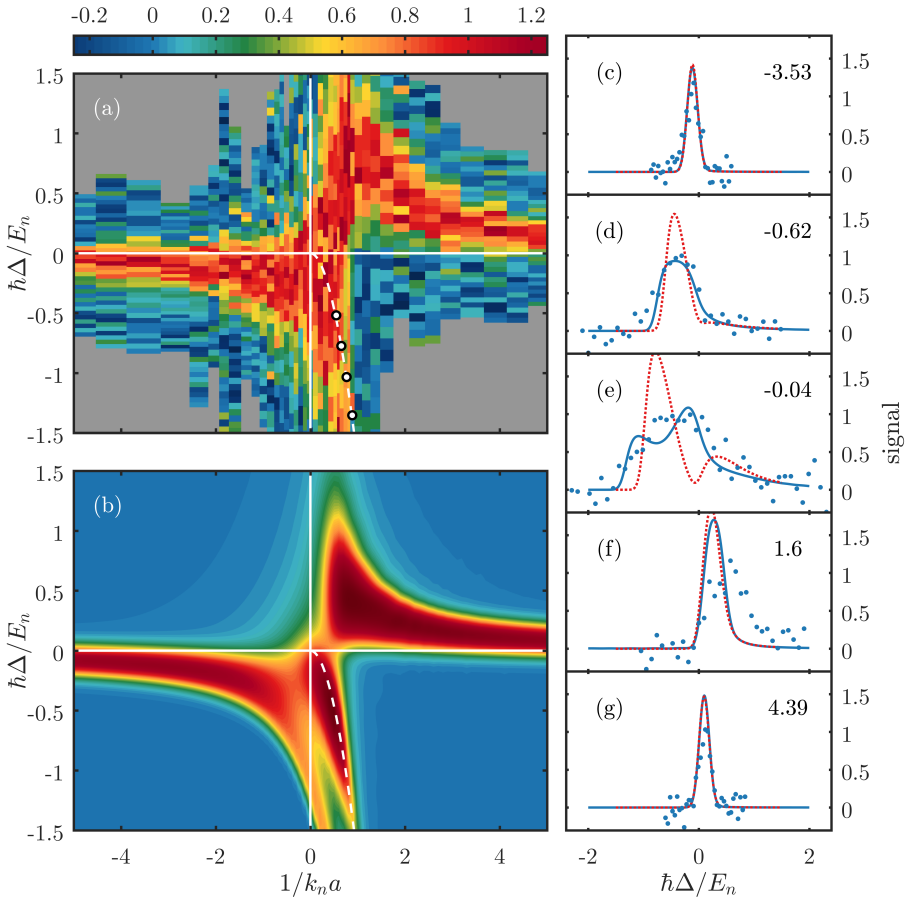

Figure 6.5: Spectrum of impurities in a Bose-Einstein condensate for different detunings and interactions. (a) Experimental signal, which is the normalized fraction of lost condensate atoms. White data points are independent measurements of the molecule energy, also shown in Fig. 6.3, compared to the energy used in the theory, shown as a white dashed line. (b) Theoretical spectrum obtained from the truncated basis method introduced in text, normalized to have the same frequency integrated weight as the experimental spectrum. (c-g) Signals at specific values of $1/k_n a$, indicated in each panel. The experimental data is shown as blue points, theoretical spectra including one excitation are shown as red dotted lines, and two excitations are shown as blue lines. This figure is based on data presented in [17].

theory including two Bogoliubov excitations [148], but it furthermore calculates a spectrum of excited states located above the ground state energy of the polaron [15, 17, 212]. These states are referred to as the many-body continuum and corresponds to polaron states with higher excitations of the medium. The truncated basis method thus calculates the entire spectral function of the impurity. Additionally, the theoretical spectrum in Fig. 6.5(b) includes the broadening from the RF pulse and the inhomogeneous density distribution of the Bose-Einstein condensate by using a local density approximation.

Since the truncated basis method includes three-body correlations, it includes any influence from the Efimov effect [148]. However, since the system is mass balanced, the size of the first Efimov trimer state is estimated to be approximately 100 times larger than the interparticle spacing, and does thus not affect the system [17, 18].

The experimental and theoretical spectrum compares remarkably well. For both attractive and repulsive interactions, a clear shift of spectral weight is observed, indicating the presence of attractive and repulsive polaron branches. As the interaction strength is increased, the shift becomes greater, and for the attractive branch, the signal clearly extends across unitarity $1/k_n a = 0$.

In Fig. 6.5(c-g), a detailed comparison between theoretical and experimental spectra at specific interactions are shown. This highlights the excellent agreement across most interactions, except at strong attractive interactions, where the agreement is only qualitative. A similar theoretical calculation only including one Bogoliubov excitation is shown as well, which clearly highlights the importance of including two excitations for strong attractive interactions in Fig. 6.5(d-e). At unitarity, the theory exhibits a double peak structure, not reproduced by experimental data. This structure is possibly an artifact arising from the limited number medium excitations [17, 164].

6.4.1 Average Energy and Width of the Spectrum

To perform a more quantitative comparison, the average width and energy of the experimental and theoretical spectra are shown in Fig. 6.6. Here, a prediction from pertubation theory as shown as well. To allow a

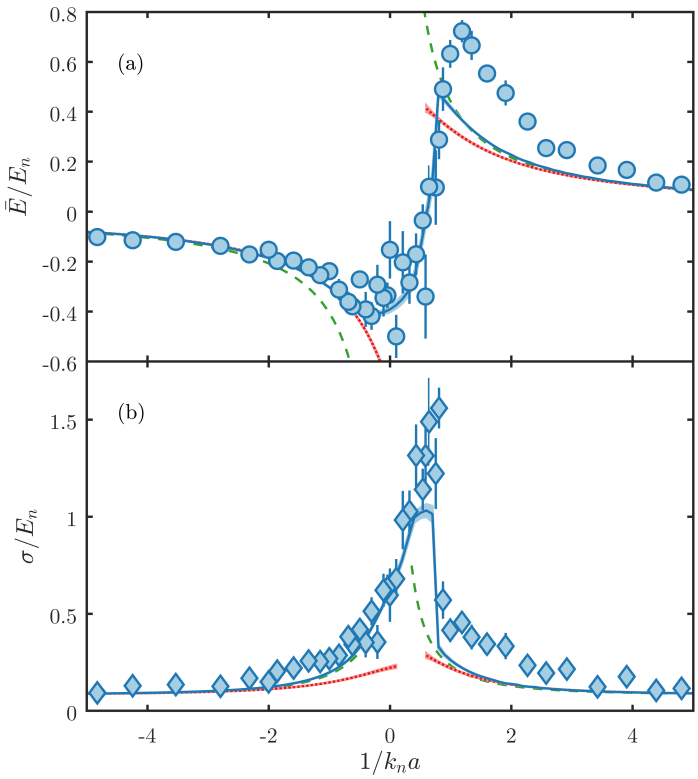

Figure 6.6: Average energy (a) and width (b) of the polaron spectrum. Blue circles and diamonds are experimental data, the blue solid and red dotted lines are theoretically obtained from the truncated basis method including respectively one and two excitations, and the green dashed lines are obtained from perturbation theory. This figure is based on data presented in [17].

proper comparison with experimental results, a Gaussian fit is applied to the various theoretical spectra, which provides the average energy $\bar{E}$ and width σ. This approach fails at strong interactions for the truncated basis method only including one excitation, and the theory is therefore excluded in this interaction regime.

For weak attractive interactions, the experimentally obtained energy agrees well with theory. As strong interactions are approached, the per-

turbation theory diverges, which is expected since it is only valid for weak interactions. The theory from the truncated basis method agrees with experimental energies until unitarity is reached, both when including one and two excitations. In the region of unitary interactions, the spectrum is composed of polaron branches, a molecular branch, and a significant many-body continuum. Consequently, the average energy of the spectrum is shifted towards positive energies. Even in this non-trivial regime the theory and experiment agrees remarkably well.

For weak repulsive interactions, the experimental energy agrees with theory as well. However, when approaching stronger interactions, the experimental results deviate significantly from all the theoretical predictions. This suggests that there are important aspects in either the theory or the experiment which have not been taken into account. This is discussed in more detail in Sec. 6.6.

The experimentally and theoretically obtained widths are shown in Fig. 6.6(b). For weak interactions, the width of the spectrum originates mainly from the finite length of the RF pulse. As intermediate interactions are approached, the inhomogeneous density becomes important. Finally, at strong interactions, the many-body continuum becomes the main contribution to the width, as seen by the clear difference between the theories including one and two excitations.

The theoretically calculated width agrees well with the one experimentally obtained, across all interactions. A minor deviation is observed for strong repulsive interactions, but as discussed, the theory is not able to account for the observed energy in this regime either.

Prior to these observations, it was an open question whether a well-defined Bose polaron exists, due to the presence of rapid three-body recombination. A short lifetime would manifest as a strong broadening of the spectrum. The theoretical spectrum does not include such broadening effects, yet it is able to account for the width of the experimentally obtained spectrum. Crucially, this demonstrates that losses occur on a time scale significantly longer than those associated with polaron physics.

To summarize, a spectroscopy which creates impurities in a Bose-Einstein condensate has revealed the existence of two polaron branches,

accounted for by theoretical calculations. The decay rate was shown to be insignificant, affirming the existence of a well-defined quasiparticle.

6.5 Transferred Fraction

It is possible that the fraction of transferred polarons has an effect on the observed spectrum. For instance, the interaction between polarons can change their energy. Furthermore, when using the spectroscopy approach presented in this study, the medium is depleted of atoms as polarons are created. Therefore, it is important to investigate how the transferred fraction of atoms affect the spectrum.

Polaron spectroscopies are performed at $1/k_n a = -0.84$ and $1/k_n a = 1.6$ for various RF powers. The number of remaining condensate atoms are shown in Fig. 6.7(a-b). With increasing power the number of remaining atoms clearly decrease. In accordance with the previous evaluation, Gaussian curves are fitted to the obtained spectroscopy signals. The obtained average energies and widths are shown in Fig. 6.7(c-d) versus the transferred fraction of atoms. This fraction is obtained from the amplitude of the fitted Gaussian curves, divided by 3, based on the assumption that impurities undergo three-body recombination.

The average energy obtained from the spectra is approximately constant with an increasing fraction of transferred atoms, while the width increases slightly. Additionally, a distortion of the lineshape is observed when applying high powers, especially for $1/k_n a = 1.6$.

These results should not be interpreted as a direct measurement of the properties of polarons at various concentrations. The formation of polarons is a dynamical process happening throughout the duration of the RF pulse. As an increasing number of polarons are created, the surrounding medium is depleted of particles at a similar rate. The last impurities created thus see a significantly lower density than the first. The full loss signal therefore contains contributions from impurities created at densities ranging from the initial density of the condensate to a final lower density. Furthermore, at strong powers the spectrum can be subject to power broadening and a non-linear response of the many-body continuum [17].

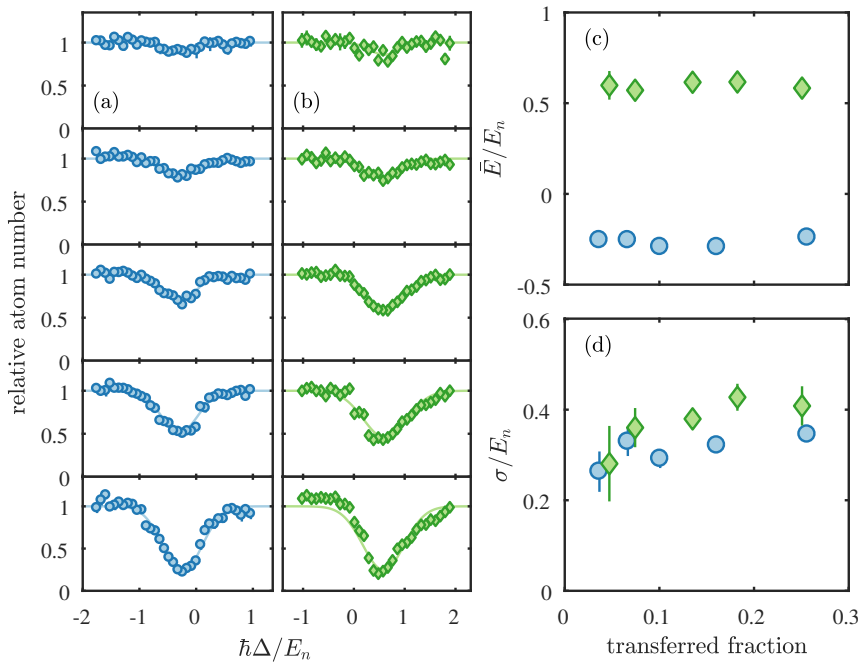

Figure 6.7: Polaron signal at various fractions of transferred atoms. Columns (a) and (b) show polaron spectroscopies of increasing RF power at $1/k_n a = -0.84$ and $1/k_n a = 1.6$, respectively. Panels (c) and (d) respectively show the evaluated average energy and width of the spectrum, where the blue circles are for attractive interactions and green diamonds for repulsive interactions. This figure is based on data presented in [17].

The observations presented in Fig. 6.7 nevertheless show that the observed average energy does not depend crucially on the RF power or the transferred fraction of atoms, which confirms that the observations presented in Sec. 6.4 are a valid characterization of the polaron. A slight broadening with increasing power is observed in Fig. 6.7(d). A better estimate of the true width of the polaron spectrum would be obtained by extrapolating the evaluated spectrum width to a transferred fraction of 0. The experimental spectrum thus overestimates the width of the spectrum, which is consistent with the observations presented in Fig. 6.6, where the experimental width is systematically slightly greater than the theoretical.

6.6 The Repulsive Branch Discrepancy

In this section, the discrepancy between experiment and theory of the repulsive polaron branch is evaluated further. Several different aspects are discussed.

First, an alternative theoretical approach is used to calculate the polaron energy. Monte-Carlo techniques are employed, which are in principle exact [146, 157]. This reveals that the truncated basis method is insufficient at fully describing strong repulsive interactions [18].

Next, a simple classical model for impurity dynamics in a repulsive Bose-Einstein condensate is introduced. Such an impurity has a probability of leaving the condensate before undergoing three-body recombination. This probability depends on the density at which the impurity is created. As the experimentally obtained signal depends on losses, the obtained spectrum is affected by this variable probability [18].

Finally, the validity of the local density approximation is tested by introducing a simple quantum-mechanical model which treats the probability for a particle of the condensate to enter various target states in an effective potential of a repulsive condensate combined with a trap. This test finds that the local density approximation is valid, and it does thus not contribute to the observed discrepancy.

6.6.1 Quantum Monte-Carlo Simulations

The experimental and theoretical data shown previously is now compared to results from quantum Monte-Carlo simulations. In Fig. 6.8, the average experimental polaron energy also presented in Fig. 6.6 is shown, along with the theoretical prediction from the truncated basis method. Additionally, results from variational theory calculations including two- and three-body correlations, but without the many-body continuum, are shown. Finally, energies obtained from Monte-Carlo calculations are shown. For the variational theories and the Monte-Carlo calculations, the average condensate density is used, and not the distribution of densities as previously.

This comparison between several different theories and the experimental data reveals interesting aspects. The variational calculations, in-

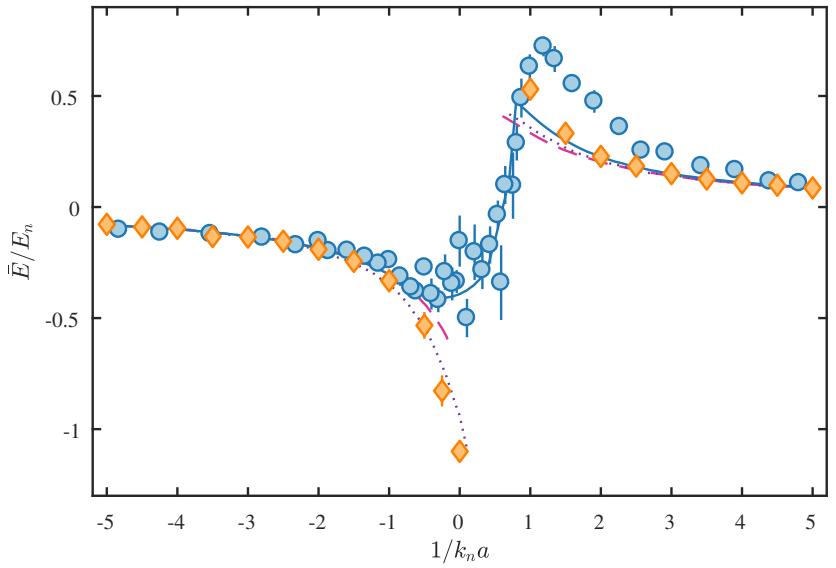

Figure 6.8: Average energy of the polaron spectrum and comparison of different theories. As in Fig. 6.6, the experimentally obtained energy is shown as blue circles, and the blue solid dotted line is theoretically obtained from the truncated basis method including two excitations. The dashed magenta and the dotted purple curves are obtained from variational theories including one and two excitations, respectively. The orange diamonds are theoretical predictions obtained through quantum Monte-Carlo simulations. This figure is based on data presented in [18].

cluding two- and three-body correlation, and the Monte-Carlo data, including all correlations, show the impact of including additional terms in the calculations.

At weak attractive interactions the theories predict the same polaron energy. When approaching strong interactions, the two variational theories start to deviate from each other because three-body correlations become important. Similarly, at unitarity, the variational theory with three-body correlations predicts a slightly different energy than the Monte-Carlo calculation, and thus higher-body correlations have an influence in this regime. These predictions are however far from the experimental data. To reproduce the average energy of the experimental spectrum, it

is crucial to include the many-body continuum which has a large spectral weight due to a small quasiparticle residue. This can be seen from Eq. (2.52) which shows that the residue is smaller for small values of a_B.

At weak repulsive interactions, the different theories predict similar polaron energies again. As strong repulsive interactions are approached, the variational theories and the Monte-Carlo calculations deviate from each other since higher-body terms become important, similar to the attractive case. However, for repulsive interactions, the higher-body terms become important already at $1/k_n a \sim 1.5$, where the Monte-Carlo calculations deviate significantly from the variational theories. The Monte-Carlo predictions do still not reproduce the experimental energies, but the truncated basis method has demonstrated the importance of the many body continuum for both attractive and repulsive interactions.

A correct prediction for the energy of the repulsive polaron branch thus needs to include both the many-body continuum and terms higher than three-body correlations, which is not done by any theory. This partially explains the discrepancy between theoretical predictions and experimental observations.

6.6.2 Simple Model for Dynamics and Decay of Impurities

In the evaluation of the experimental spectrum, it was assumed that every impurity particle undergoes three-body recombination. However, strong repulsive interactions with the condensate will accelerate an impurity outwards as sketched in Fig. 6.9(a). Generally, impurities created near the center have a large probability of undergoing three-body recombination before leaving the condensate, whereas impurities created near the boundary of the condensate, has a large probability of escaping without recombination. In practice, the repulsive polaron signal obtained from the number of lost atoms will be distorted, with the spectral weight being shifted towards higher energies.

To evaluate this effect more quantitatively, a simple model treating a classical particle interacting with the mean-field potential of a repulsive Bose-Einstein condensate is considered. For simplicity, a spherically

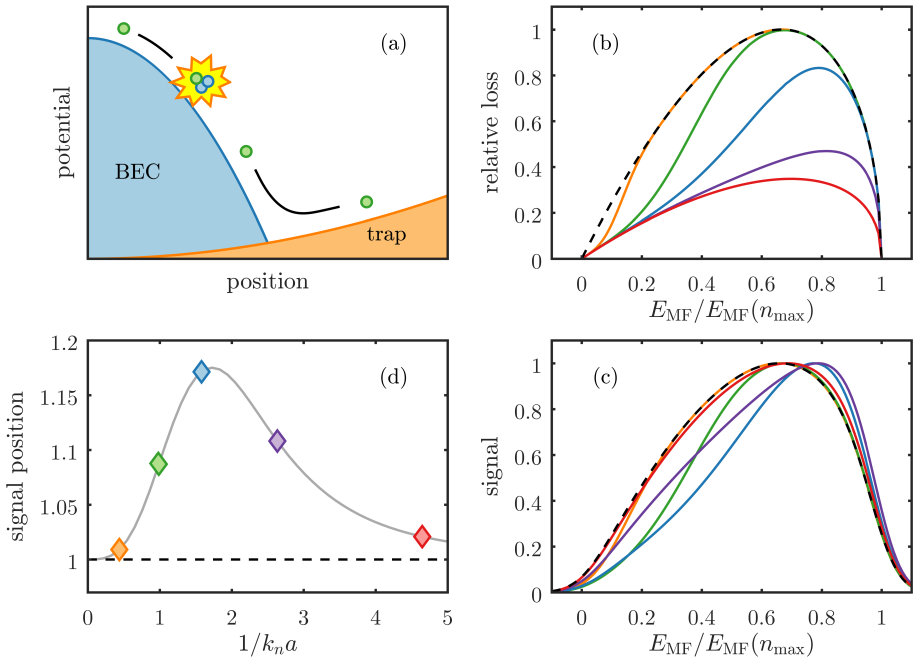

Figure 6.9: Simple mean-field model of impurity dynamics and decay, which predicts a shift in the experimentally obtained repulsive polaron signal based on atom loss. (a) Sketch showing the principle of the model. Impurities created near the center of the condensate undergo three-body recombination often, compared to impurities created close to the boundary of the condensate. (b) The black dashed curve is the expected loss distribution across different mean-field energies, assuming that all impurities undergo recombination. The predictions from the model are shown as colored curves for different interaction strengths a ($1/k_n a$). From bottom to top, the red curve is for $170a_0$ (4.6), the purple curve is for $300a_0$ (2.6), the blue curve is for $500a_0$ (1.6), the green curve is for $800a_0$ (1.0), and the orange curve is for $1800a_0$ (0.4). (c) Curves of (b) convoluted with a Gaussian and normalized to the same amplitude. (d) Signal shift predictions of the model at different interaction strengths, relative to the signal position when assuming that all particles undergo three-body recombination. The diamonds correspond to interaction strengths from the predictions shown in (b) and (c). These results are also presented in [18].

symmetric trap is assumed, of frequency $\omega = (\omega_x\omega_y\omega_z)^{1/3} = 2\pi \times 182\,\mathrm{Hz}$ and mean density $2.3 \times 10^{14}\,\mathrm{cm}^{-3}$, similar to the conditions of the experiment. The impurity interacts with the condensate by a mean-field potential

$$E_{\mathrm{MF}}(a, n(r)) = \frac{4\pi\hbar^2 a}{m} n(r), \qquad n(r) = n_{\max}\left(1 - \frac{r^2}{R^2}\right), \tag{6.4}$$

where R is the Thomas-Fermi radius, $n_{\max}$ is the peak density, and r is the radial coordinate. The resulting acceleration of the particle is determined by the gradient of the potential, which provides a classical equation of motion $\mathrm{d}^2 r(t)/dt^2 = Ar(t)/m$, where $A = 8\pi\hbar^2 a n_{\max}/mR^2$. This is the equation of a harmonic oscillator, but with an opposite sign. For starting conditions $\mathrm{d}r/\mathrm{d}t = 0$ and $r(0) = r_0$, this equation has the solution

$$r(t) = r_0 \cosh\left(\sqrt{\frac{A}{m}}t\right). \tag{6.5}$$

By setting $r = R$, a direct expression for the time it takes for a particle to escape the condensate is obtained $t_{\mathrm{out}} = \sqrt{m/A}\cosh^{-1}(R/r_0)$.

The probability of an impurity undergoing three-body recombination is obtained by investigating the recombination rate in the duration it takes the impurity to leave the condensate. The local three-body recombination rate for the impurity is calculated using $L_3(a)n^2(r)$, where $L_3(a)$ is the three-body recombination coefficient. This can be calculated from Eq. (2.49), but in this model it is assumed that no Efimov resonances exists in the relevant range of interactions by setting the $\sin^2$-terms to 1. The recombination rate integrated in time provides a quantity which is the average number of decay events the impurity will undergo before leaving the condensate. This can be converted to a probability by an exponential function

$$P_{\mathrm{3BR}} = \exp\left[-\int_0^{t_{\mathrm{out}}} L_3(a)n^2(r)\mathrm{d}t\right], \tag{6.6}$$

which can be calculated for any given a and r_0.

This model for impurity dynamics and decay only includes mean-field effects, which is certainly incorrect at strong interactions. A simple way of refining the model is to replace the interaction strength a with an effective interaction $a_{\text{eff}}^{-1} = a^{-1} + n^{1/3}$, which reflects the transition to the unitary interaction regime $1/a = 0$, where the interparticle spacing $n^{-1/3}$ is the relevant length scale of interactions [213, 214]. This complicates solving the equation of motion analytically, but a numerical approach is straightforward.

The effect that the variable impurity loss has on the obtained polaron spectrum is now evaluated. The initial assumption was that every particle undergoes three-body recombination. In the mean-field limit, the fraction of transferred atoms is homogeneous across all densities. The atom loss resulting from impurities created at a certain mean-field energy is thus given by the density distribution of atoms. In Fig. 6.9(b), the corresponding loss distribution across different energies is shown, assuming all impurities undergo recombination. A recombination event yields a threefold atom loss in comparison with the impurity leaving the condensate. The modification to the atom loss at a given energy and scattering length is thus $(1 + 2P_{\text{3BR}})/3$. This modification is calculated across all condensate densities for different scattering lengths using the effective interaction strength a_{eff}, and the resulting signal is shown in Fig. 6.9(b). The lineshape is clearly modified due to impurities leaving before recombination.

To provide a comparison with the experimental signal, the curves in Fig. 6.9(b) are convoluted with a Gaussian of width $\sigma = E_{\text{MF}}(n_{\text{max}})/15$ and normalized to an amplitude of 1, which is shown in Fig. 6.9(c). Finally, the signal shift is evaluated by fitting a Gaussian to the curves in Fig. 6.9(c). The obtained signal position is shown in Fig. 6.9(d), relative to the position when assuming that all impurities undergo three-body recombination. The signal position is clearly shifted towards higher energies at strong interactions and the relative deviation is remarkably similar to the discrepancy shown in Fig. 6.6(a) and Fig. 6.8. It is also worth noting that the apparent lack of polaron signal in Fig. 6.5(a) in the region of $1/k_n a$ between 1 and 3 and Δ close to 0, can be explained by impurities leaving the condensate.

The results presented above are based on very simple expressions for energy, dynamics, and recombination, and a more correct calculation requires complicated models. Nevertheless, the results clearly display the impact that impurity dynamics have to the polaron signal, which was obtained through loss observations, and the model provides an estimate of the magnitude of the effect.

Similar calculations were performed with different values of L_3, without the refinement using the effective interaction a_{eff}, with different convolution widths σ, and with a signal evaluation based on the first moment of the distribution instead of a Gaussian fit. All these variations provide qualitatively similar results as the curve in Fig. 6.9, with minor shifts to the amplitude and peak position of the curve.

To obtain the experimental polaron spectrum, the power of the RF pulse was adjusted to provide a loss of approximately 30 %, which was based on the assumption that all impurities undergo recombination. However, for weak repulsive interactions very few impurities undergo recombination, as shown in Fig. 6.9(b). To obtain a loss of 30 %, the transfer fraction in this interaction regime was possibly significantly larger than intended. As shown in Sec. 6.5, this has a vanishing effect on the average energy of the obtained spectrum, but increases the spectrum width.

It is clear that the impurity dynamics result in a distortion of the detected spectrum for repulsive interactions, since impurities leave the condensate region. For attractive interactions, the impurities do not accelerate outwards away from the condensate, and will thus always recombine. The effect presented here does thus not influence the attractive branch.

6.6.3 Wave Function Overlap of Initial and Final States

For the truncated basis method calculation, a local density approximation was used to take the density distribution of the Bose-Einstein condensate into account. In other words, when a condensate atom is transferred into the impurity state, its polaron energy is calculated based on the density at the position where it is created. The full spectrum at a given value of $1/k_n a$ is then calculated by using the entire density distribution of the condensate and weighting with the relative number of

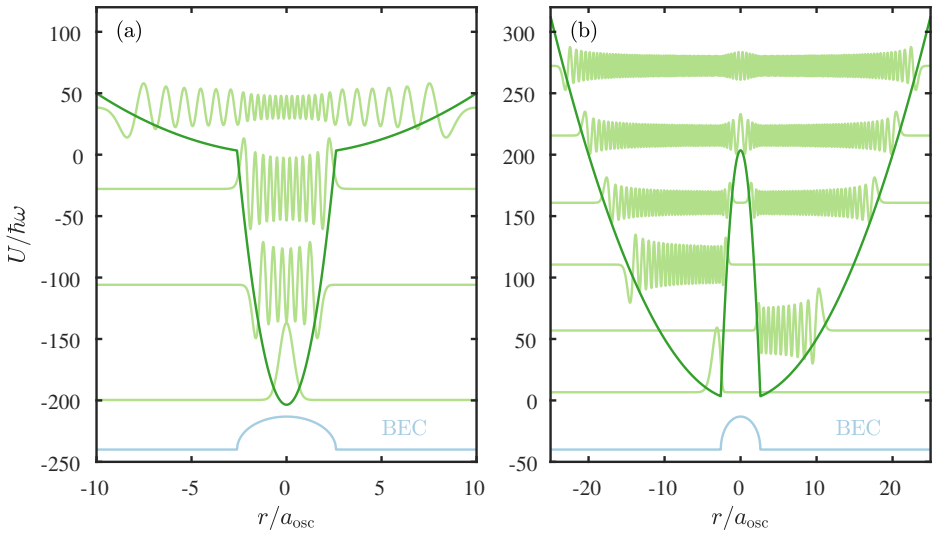

Figure 6.10: Effective potentials felt by impurities and corresponding eigenstates for (a) attractive and (b) repulsive interactions, for interaction strengths $a = \pm 540 a_0$ corresponding to $1/k_n a = \pm 1.5$. In each panel, exemplary eigenstates are shown, compared to the condensate wave function (BEC).

atoms located at different densities. However, in a quantum system, the weighting is not determined by the local density but by the overlap between wave functions of initial and final states.

Here, one-dimensional calculations of wave function overlaps are presented and discussed. The impurity state $|2\rangle$ experiences a mean-field potential from the condensate and a trapping potential. The resulting potential U for the impurity is shown in Fig. 6.10 for strong attractive and strong repulsive interactions with the Bose-Einstein condensate. Again, the parameters are chosen similarly to the experimental conditions with trap frequnecy $\omega = (\omega_x \omega_y \omega_z)^{1/3} = 2\pi \times 182\,\mathrm{Hz}$ and mean density $2.3 \times 10^{14}\,\mathrm{cm}^{-3}$. In Fig. 6.10, the interaction strengths are $a = \pm 540 a_0$ corresponding to $1/k_n a = \pm 1.5$.

The Schrödinger equation of the effective potential U is solved for a given value of the interaction strength a using the numerical finite difference method. Here, the spatial axis is discretized into a finite number of points, and the potential and kinetic energy terms are written as di-

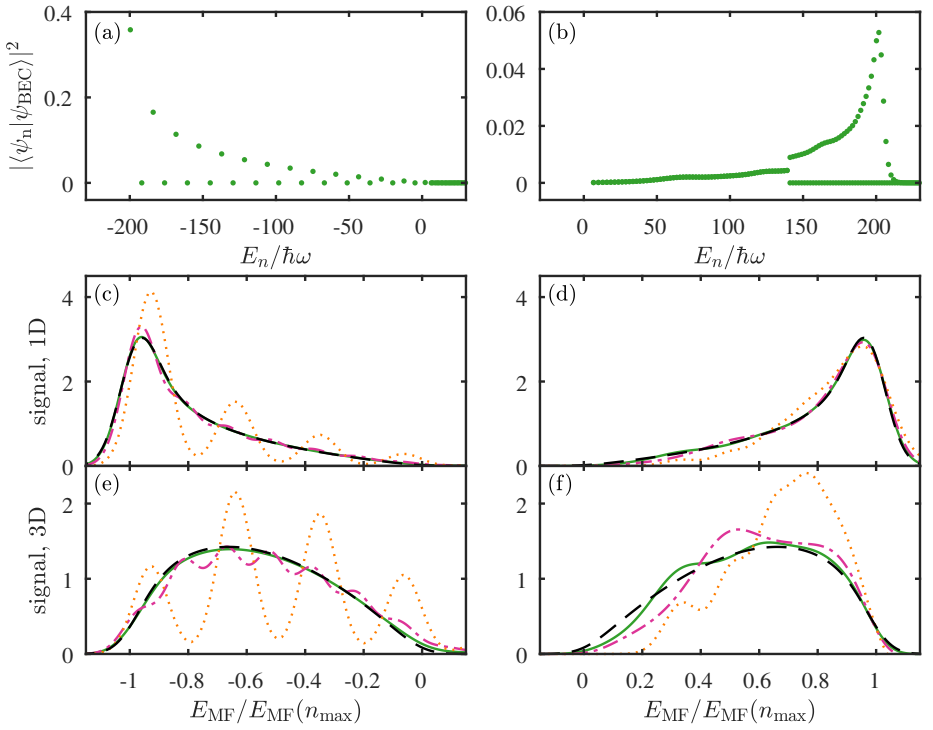

Figure 6.11: Wave function overlaps and corresponding polaron signal in different dimensions. The overlaps $|\langle\psi_n|\psi_{\mathrm{BEC}}\rangle|^2$ calculated using the potentials of Fig. 6.10 are shown for (a) attractive and (b) repulsive interactions. The resulting signal is shown for calculations in one dimension (c-d) and in three dimensions (e-f), for attractive (c, e) and repulsive (d, f) interactions, at different interaction strengths a ($1/k_n a$). The orange dotted curves are for $\pm 45 a_0$ (± 18), the magenta dash-dotted curves are for $\pm 153 a_0$ (± 5.2), and the green curves are for $\pm 540 a_0$ (± 1.5). For comparison, black dashed curves based on the local density approximation are shown.

agonal matrices. The Laplacian of the kinetic energy is locally approximated by Taylor polynomials. The Hamiltonian is then solved, yielding the eigenstates ψ_n and corresponding energies E_n. A few exemplary wave functions are shown in Fig. 6.10 at a height corresponding to their energy and compared to the wave function of the Bose-Einstein condensate ψ_{BEC}.

The overlap between eigenstates and the condensate wave function $|\langle\psi_n|\psi_{\mathrm{BEC}}\rangle|^2$ is calculated and shown in Fig. 6.11(a-b) for the potentials shown in Fig. 6.10. For attractive interactions, with increasing principal quantum number n, the overlap alternates between a finite value and zero, because the eigenstates alternate between being even and odd functions. Moreover, the overlap of the eigenstates decrease as zero energy is approached. For repulsive interactions, the alternating behavior is only present for large energies. At low energies, the eigenstates alternate between being located on either side of the repulsive condensate potential as shown in Fig. 6.10(b), and these eigenfunctions all have a finite overlap with the condensate wave function. At a sufficiently large energy, the eigenstates are located on both sides of the condensate potential simultaneously. At this point, the alternating overlap behavior starts and continues until the overlap vanishes at large energies.

The two distributions in Fig. 6.11(a-b) are similar in shape, with opposite energies. The magnitude of the individual overlaps are generally larger for attractive potentials, but the density of states is smaller.

The calculated overlaps are now compared to the local density approximation, which is shown in Fig. 6.11(c-d). The overlap distributions are first normalized in energy to the amplitude of the effective potential of the condensate $E_{\mathrm{MF}}(n_{\mathrm{max}})$. Then, a convolution with a Gaussian is performed and the resulting signal is normalized to the same integrated energy. This procedure is performed for three different values of $\pm a$. The results are compared to a curve obtained by a similar procedure, but using the local density approximation. Without convolution, this curve thus reflects the number of atoms located at various densities $\sim (n/n_{\mathrm{max}})/\sqrt{1-n/n_{\mathrm{max}}}$, as opposed to an overlap between initial and final states. Note that the distribution of atoms at different densities in one dimension is significantly different to that found in three dimensions.

For large values of $|a|$, the distribution of overlaps agrees remarkably well with the local density approximation, for both attractive and repulsive interactions. For weak attractive interactions, the individual eigenstates are clearly visible in the signal, but these disappear as $|a|$ is increased. For weak repulsive interactions, the individual eigenstates are

not visible in the spectrum, but they do alter the signal slightly, compared to that obtained by the local density approximation.

A primitive comparison with the relevant case of three dimensions is now performed. The three-dimensional distribution of atoms is proportional to $(n/n_{\max})\sqrt{1-n/n_{\max}}$ and can be obtained from the one-dimensional one by multiplication of $(1-n/n_{\max})$, ignoring front factors. To convert the overlap distribution from one to three dimensions, it is naively assumed that the density of states undergo a conversion similar to the density distribution when changing dimensions. The conversion from one to three dimensions is therefore performed by multiplying the overlap magnitudes with $(1-E_n/E_{\mathrm{MF}}(n_{\max}))$. The resulting signals are shown in Fig. 6.11(e-f). For strong interactions, the obtained curves are again similar to those obtained from the local density approximation. The deviation for weak interactions is however larger. This is possibly a result of the naive conversion from one to three dimensions. Yet, no significant shift of signal weight is observed, except for very weak interactions.

It is astounding that the complicated overlaps of eigenstates shown in Fig. 6.10 exactly reproduce the local density approximation. An explanation is given in the following. For attractive interactions, the integration of the oscillating part of the eigenfunctions average out and provide a vanishing overlap with the condensate wave function. Mainly the outermost peaks of the eigenstates provide a significant contribution to the overlap integral. The contribution these peaks add is largely determined by the amplitude of condensate wave function exactly at the positions of the peaks. The eigenstates thus probe the local density of the condensate at the classical turning points of the potential, which reproduce the local density approximation. A similar argument can be made for repulsive interactions.

This result can also be interpreted as an example of Bohr's correspondence principle which states that the behavior of quantum systems reproduce classical physics in the limit of large quantum numbers.

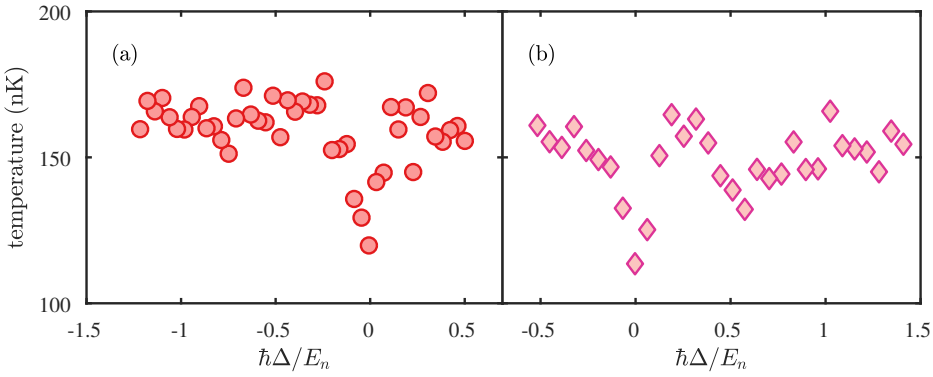

Figure 6.12: Temperature of the ensemble after the polaron spectroscopy. Throughout most of the spectrum the temperature is approximately constant, but near the bare transition $\Delta = 0$, a remarkable decrease in temperature is observed. The interaction strengths for the data shown here is $1/k_n a = -2.3$ in (a) and $1/k_n a = 1.9$ in (b).

6.7 Cooling Near Interstate Feshbach Resonance

In this section, a cooling effect which was observed while acquiring the polaron data is discussed. To acquire polaron data, a Bose-Einstein condensate is prepared at a finite temperature and imaged using absorption spectroscopy after expansion. Both information of the condensate and thermal fraction is obtained.

In Fig. 6.12, the temperature obtained from a Gaussian fit to the thermal component of the expanded cloud is shown for two values of $1/k_n a$. For the majority of detunings, the evaluated temperature of the thermal cloud is approximately 160 nK. However, near the bare transition a lower temperature is observed. Similarly, a lower number of thermal atoms is observed (not shown). The effect is observed throughout most of the spectrum shown in Fig. 6.5. This remarkable decrease of temperature is explained by a selective depletion of thermal atoms leading to a lower average energy of the ensemble, which is discussed in detail in the following.

In the evaluation of the polaron signal, the condensate and thermal fraction were assumed to be independent components, where the large dilute thermal cloud has an insignificant contribution to the density relevant for the polaron energy. Within this assumption, a RF pulse near the bare transition will mainly perform a transfer of thermal atoms. Any three-body recombination with these transferred atoms will also mainly involve thermal atoms. Atoms removed from the $|1\rangle$ state will no longer contribute to determine the critical temperature for Bose-Einstein condensation. The critical temperature will decrease, and the condensate fraction will increase. Since Eq. (2.13) is not fulfilled, the ensemble is out of thermodynamic equilibrium and atoms will redistribute from the condensate to the thermal cloud. Every atom moving from the condensate to the thermal cloud will lower the average energy of thermal atoms due to energy preservation. Consequently, the temperature is lower after rethermalization.

A simple model is introduced to analyze this phenomenon quantitatively, which is shown schematically in Fig. 6.13. The condensate and thermal cloud are treated as separate components and the process is divided into three stages: (1) initial equilibrium, (2) thermal atoms have been removed and the two components are out of equilibrium, and (3) new equilibrium after rethermalization.

Initially, the two components are in equilibrium, fulfilling Eq. (2.13) at temperature $T^{(1)}/T_c^{(1)}$ and with a fraction of atoms in the condensate $N_0^{(1)}/N^{(1)}$, with total atom number $N^{(1)} = N_t^{(1)} + N_0^{(1)}$, where $N_t^{(1)}$ is the number of thermal atoms. Then, a certain fraction of the thermal atoms is removed, resulting in $N_t^{(2)} = \eta_t N_t^{(1)}$, where $0 \leq \eta_t \leq 1$. Consequently, the condensate fraction is changed and the critical temperature is increased to $T_c^{(2)}$.

It is assumed that thermal atoms are removed homogeneously from the sample and consequently the average energy of the thermal atoms is unchanged $T^{(2)} = T^{(1)}$. It is not strictly correct to assign a temperature at this point, since the ensemble is not in thermal equilibrium. Therefore, $T^{(2)}$ describes the average energy of the thermal component, and not the actual temperature of the full ensemble.

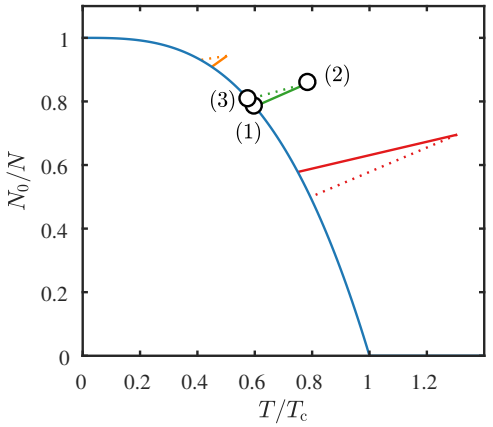

Figure 6.13: Scheme for cooling at an interstate Feshbach resonance. The blue curve is Eq. (2.13). (1) Initially, a finite temperature ensemble composed of a thermal cloud and a Bose-Einstein condensate is in thermal equilibrium. (2) Thermal atoms are selectively removed, which decreases the critical temperature and increases the fraction of condensate atoms, but the system is out of equilibrium (solid curves). (3) The ensemble reaches thermal equilibrium again (dotted curves). Initial temperatures of $T^{(1)}/T_c^{(1)} = 0.75$ (red curves), $T^{(1)}/T_c^{(1)} = 0.6$ (green curves), and $T^{(1)}/T_c^{(1)} = 0.45$ (orange curves) are shown, and the fraction of remaining thermal atoms is $\eta_t = 0.6$. Note that the condensate fraction decreases for $T^{(1)}/T_c^{(1)} = 0.75$, while it increases for the two other initial temperatures shown.

By using Eq. 2.11, the new critical temperature can be expressed in terms of the initial critical temperature as

$$\frac{T_c^{(1)}}{T_c^{(2)}} = \left(1 - \left[\frac{T^{(1)}}{T_c^{(1)}}\right]^3 \left(1-\eta_t\right)\right)^{-3}, \tag{6.7}$$

and the out-of-equilibrium condensate fraction is

$$\frac{N_0^{(2)}}{N^{(2)}} = \left[1 + \eta_t \left(\left[\frac{T^{(1)}}{T_c^{(1)}}\right]^3 - 1\right)\right]^{-1}. \tag{6.8}$$

Next, the ensemble will rethermalize until Eq. (2.13) is fulfilled by means of condensate atoms becoming thermal. The average energy of the $N_{\mathrm{t}}^{(2)}$ thermal atoms before rethermalization is $3k_{\mathrm{B}}T^{(2)}$. The energy of condensate atoms is negligible compared to that of thermal atoms. After rethermalization, $N_{\mathrm{t}}^{(3)}$ atoms have the average energy $3k_{\mathrm{B}}T^{(3)}$, and due to the conservation of energy the total energies are equal, which yields $T^{(2)}N_{\mathrm{t}}^{(2)} = T^{(3)}N_{\mathrm{t}}^{(3)}$. From this expression, the condensate fraction after equilibrium can be calculated

$$\frac{N_0^{(3)}}{N^{(3)}} = 1 - \left[\left(1 - \frac{N_0^{(2)}}{N^{(2)}}\right)\frac{T^{(2)}}{T_{\mathrm{c}}^{(2)}}\right]^{\frac{3}{4}}, \tag{6.9}$$

from which the final temperature can be expressed through Eq. (2.13), or related to the initial temperature as

$$\frac{T^{(3)}}{T^{(1)}} = \frac{T_{\mathrm{c}}^{(3)}}{T_{\mathrm{c}}^{(1)}}\left[\frac{1 - \frac{N_0^{(3)}}{N^{(3)}}}{1 - \frac{N_0^{(1)}}{N^{(1)}}}\right]^{\frac{1}{3}}. \tag{6.10}$$

The final condensate fraction and temperature for different values of η_{t} are shown in Fig. 6.14. The model clearly predicts a decrease in temperature as thermal atoms are selectively removed, and does thus explain the temperature behavior of the data shown in Fig. 6.12.

It is relevant to consider what happens when condensate atoms are selectively removed, which is the case for the majority of the data in Fig. 6.12. If atoms are selectively removed from a condensate of $N_0^{(1)}$ atoms such that $N_0^{(2)} = \eta_{\mathrm{c}}N_0^{(1)}$ $(0 \leq \eta_{\mathrm{c}} \leq 1)$ atoms remain, the condensate fraction will decrease and the critical temperature of the ensemble will increase, similarly to when thermal atoms are removed. It turns out that the increase in critical temperature exactly corresponds to the decrease in condensate fraction, such that Eq. (2.13) stays fulfilled for any η_{c}. Selective removal of condensate atoms does thus not affect the temperature. This is consistent with the results shown in Fig. 6.12, where the temperature is approximately constant for all detunings but 0. The data does however indicate a minor decrease in temperature at $\hbar\Delta/E_{\mathrm{n}} \approx 0.5$ for $1/k_n a = 1.9$.

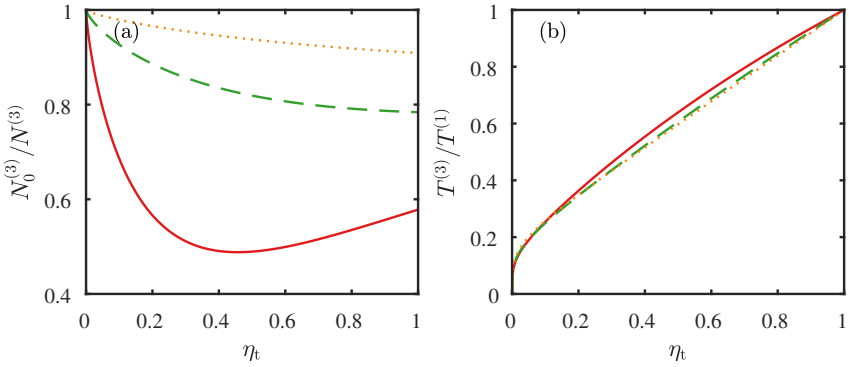

Figure 6.14: Increase in condensate fraction (a) and decrease in temperature (b) after rethermalization for $T^{(1)}/T_c^{(1)} = 0.75$ (solid red lines), $T^{(1)}/T_c^{(1)} = 0.6$ (dashed green lines), and $T^{(1)}/T_c^{(1)} = 0.45$ (dotted orange lines).

Two relevant effects have been neglected in this simple model. First, a RF pulse of finite length is not able to selectively remove only thermal atoms. Some condensate atoms from low-density regions of the condensate will typically be removed as well, which makes the cooling less efficient. Second, a RF pulse might not remove atoms fully homogeneously from the thermal component. Any thermal atoms which spatially overlap with the condensate will not be transferred, since interactions perturb the bare transition. Consequently, thermal atoms will mainly be transferred from outer regions of the trap. As these atoms are more energetic, the process corresponds to evaporative cooling, and thus the cooling is more efficient. To predict the magnitude of these effects requires more comprehensive calculations. They do however counteract each other, and the presented model qualitatively explains the data in Fig. 6.12 well.

The cooling effect is similar to the cooling obtained through RF evaporation. In regular evaporative cooling, energetic atoms are selectively removed due to their interaction with a magnetic field. Here, atoms are selectively removed due to a strong interaction with other atoms.

6.8 Summary

To summarize this chapter, a repulsive and an attractive polaron branch was observed by applying RF spectroscopy to a Bose-Einstein condensate of ^{39}K atoms. The experimental observations were compared to a theoretical spectrum obtained from comprehensive numerical calculations. The two spectra agreed remarkably well across most interaction strengths, except for strong repulsive interactions. Based on the comparison, the existence of a long-lived well-defined Bose polaron was confirmed.

The repulsive branch discrepancy between theory and experiment was accounted for. It was demonstrated that the theoretical model is insufficient at strong repulsive interactions, and a model for the dynamics and the decay of impurities in a repulsive mean-field potential was introduced to show that the experimental evaluation misjudges the polaron signal.

Other interesting effects were also considered. The overlap of wave functions, relevant for the transfer of atoms into the impurity state, was calculated, which verified that the local density approximation was adequate. Finally, a peculiar cooling effect observed in the polaron spectrum was discussed and explained by a simple model.

CHAPTER 7

THESIS CONCLUSIONS

Within this thesis, a series of studies were presented, based on the tunable interactions offered by quantum gases. This allowed a broad range of physical phenomena to be studied, ranging from few- to many-body physics, and from balanced mixtures to impurity physics.

In Chapter 4, the properties of dual-species Bose-Einstein condensates with tunable interactions were studied. The main aim was to clarify the role of the miscibility in the system. By a combined theoretical and experimental effort it was shown that the miscibility parameter Δ_{stab} does not always provide a clear description of neither the in-trap density distributions or center-of-mass condensate positions after expansion.

These investigations shed new light on multi-component systems in general and will serve to guide future studies of dual-species Bose-Einstein condensates. The results show that the use of the miscibility parameter Δ_{stab} does typically not provide a meaningful description of these systems. This encourages future research on the properties and dynamics of dual-species Bose-Einstein condensates.

In Chapter 5, the three-body physics of KRb mixtures and of single-component ^{39}K ensembles was explored. The search for Efimov reso-

nances in KRb mixtures concluded a long-standing debate regarding observations of Efimov physics in heteronuclear mixtures.

Additionally, preliminary observations on the temperature dependence of an Efimov resonance in ^{39}K was presented, displaying a remarkable behavior. These intriguing results show that there are still open questions in the field of few-body physics.

In Chapter 6, the primary result of this thesis was presented, which was the observation of the polaron quasiparticle in a Bose-Einstein condensate. The experimental results were successfully compared with a detailed theory, which showed that indeed a well-defined quasiparticle was created and detected.

A discrepancy was observed for repulsive interactions. This was accounted for by comparison with a more complete theory, and by considering the dynamics and recombination of the impurities.

7.1 Outlook

The creation and observation of polarons in a Bose-Einstein condensate opens up many interesting research opportunities. The scenario of an impurity interacting with its surroundings continues to be studied experimentally [16, 215–217] and theoretically [158–162, 164, 218–225] in quantum gases. The strong interest of polarons in ultracold gases has even inspired studies of impurities in solid-state physics [226].

A current interest is the question of how the properties of the polaron changes when the condensate melts. Recently, an intriguing behavior at finite temperatures was predicted. In the limit of weak interactions, the energy of the polaron is predicted to increase dramatically with temperature [161]. This is due to the Bose-Einstein condensate phase transition at T_c which changes the density of states for the medium particles significantly, changing the scattering of the impurity. For strong interactions, the formation of multiple polaron states at finite temperatures was recently predicted, which has parallels with the quark-gluon plasma [162, 227].

Another intriguing topic is the universality of the Bose polaron. Universal behavior is often found in systems with unitary interactions. However, for the Bose polaron, the characteristic length scale associated with Efimov trimers can influence the properties of the polaron, and the system is non-universal. Nevertheless, a recent theoretical study suggests that the Bose polaron energy is a universal function of the Efimov three-body parameter [160]. This hypothesis does not only establish universal properties for the polaron, but it also forms a connection with Efimov physics.

Within the scope of this dissertation, other research projects were initiated, but not completed. A great interest is quantum fluctuations in Bose mixtures. The impact of quantum fluctuations is captured by the Lee-Huang-Yang correction to the mean field energy [228] (similar to the second term of Eq. (2.51). It was recently pointed out that quantum fluctuations can stabilize a bosonic mixture, which would otherwise collapse due to mean-field attraction [229]. This was recently observed, using two-component ^{39}K condensates in the $|F = 1, m_F = 0\rangle$ and $|1, 0\rangle$ hyperfine states near the Feshbach resonances at 60 G shown in Fig. 1.1 [230–232]. Additionally, the same principle has been used to explain a recent series of experiments with dipolar condensates [233–236]. Common for all of these systems is that attractive mean-field contributions dominate the Lee-Huang-Yang correction to achieve stabilization.

A current research project considers a bosonic mixture where mean-field interactions are canceled entirely. Consequently, the Lee-Huang-Yang correction remains as the only relevant interaction, which allows the system to be treated analytically. This system thus provides an excellent setting for studying quantum fluctuations.

To summarize, the results presented within this thesis open up for intriguing opportunities to study quantum physics and quantum impurities in regimes never realized before.

APPENDIX A

ADDITIONAL PUBLICATIONS

This appendix presents two studies not included in the main text. The research of the thesis primarily concerns ultracold mixtures with tunable interactions, whereas the two studies shown here does not. They are, however, still relevant for the field of quatum gases.

The first study is theoretical. Single atoms are simulated in superimposed optical lattice potentials, used to implement one- and two-qubit quantum gates [30]. This study was initiated in a bachelor's thesis [237], but the results were later extended and reported in a paper which was finished and published within the time frame of this dissertation.

The second study is technical and presents a simple approach to stabilize the frequency of a laser by utilizing a field-programmable gate array to implement laser lock electronics [31, 238].

The published manuscripts are found in the following sections of this appendix, along with brief introductions.

Both manuscripts are reprinted with permission.

A.1 One- and Two-Qubit Quantum Gates Using Superimposed Optical Lattice Potentials

Atoms isolated in the single sites of a optical lattice are viable candidates of qubits in a quantum computer. In this theoretical study, a superimposed optical lattice potential is utilized to create both one- and two-qubit quantum gates. The one-qubit gate exploits the differential hyperfine shift, which allows single atoms to be addressed. The two-qubit gate is implemented by merging two otherwise isolated sites, which allows the two atoms to collide. Both gate types are found to be robust with small error probabilities and gate times of a few hundred microseconds.

Single- and two-qubit quantum gates using superimposed optical lattice potentials

Nils B. Jørgensen, Mark G. Bason, and Jacob F. Sherson*
Department of Physics and Astronomy, Aarhus University, DK-8000 Aarhus C, Denmark
(Dated: February 10, 2014)

Steps towards implementing a collision based two-qubit gate in optical lattices have previously been realized by the parallel merging all pairs of atoms in a periodicity two superlattice. In contrast, we propose an architecture which allows for the merger of a selected qubit pair in a novel long-periodicity superlattice structure consisting of two optical lattices with close-lying periodicity. We numerically optimize the gate time and fidelity, including the effects on neighboring atoms, and in the presence of experimental sources of error. Furthermore, the superlattice architecture induces a differential hyperfine shift, allowing for single-qubit gates. The fastest possible single-qubit gate times, given a maximal tolerable rotation error on the remaining atoms at various values of the lattice wavelengths, are identified. We find that robust single- and two-qubit gates with gate times of a few 100 μs and with error probabilities $\sim 10^{-3}$ are possible.

PACS numbers: 03.67.Lx,37.10.Jk,67.85.-d

I. INTRODUCTION

The ability to prepare and manipulate ultracold atoms in optical lattices has led to many breakthroughs in the last decade. From demonstrating the superfluid to Mott-insulator transition [1], to strongly interacting Fermi gases [2, 3], the purity and controllability of ultracold atoms has greatly benefited many-body physics [4]. Due to the inherent, repeating pattern of an optical lattice and the long-coherence times of neutral atoms arranged in such systems, they are also viable candidates for quantum computing [5, 6]. Ultracold atoms in optical lattices are scalable and offer parallelism due to their geometry [7]. Implementing the two-qubit gates necessary for quantum computation is a long-standing problem using this approach. In optical lattices, two-qubit gates have been proposed [8] and conducted on many pairs of atoms in parallel [9, 10], by making use of ground state collisions [6]. Alternatively, one may make use of dipole-dipole interactions between Rydberg states [11–13], as indicated by recent experiments on pairs of atoms in dipole traps [14, 15], or by means of hybrid atom-molecule schemes in optical lattices [16].

The challenge of implementing a two-qubit gate on a selected pair of atoms in a large array has yet to be fulfilled largely due to the experimental difficulty in obtaining an imaging resolution comparable to the lattice spacing. Initially this lead to proposals to achieve single site addressing using sub-diffraction optical techniques [17–19] and an experimental demonstration using magnetic gradients [20]. Recently, however, single site imaging [21, 22] and single site addressing using a strongly focussed optical tweezer [23] were achieved. This paves the way for the realization of the two-qubit gates proposed for controllable micropotentials [24–30], triple-wells [31, 32], and in optical lattices [33–35]. As demonstrated in Ref. [35], a high fidelity realization of gates using an optical tweezer imposes rather strict demands on the pointing stability of the addressing laser. One solution to the problem may involve the use of superlattices involving two optical lattices of separate optical frequencies. Such an arrangement has already been used to investigate double-well dynamics [9, 36] and demonstrate patterned loading [37] in a triple-well superlattice. Recently, an additional long-

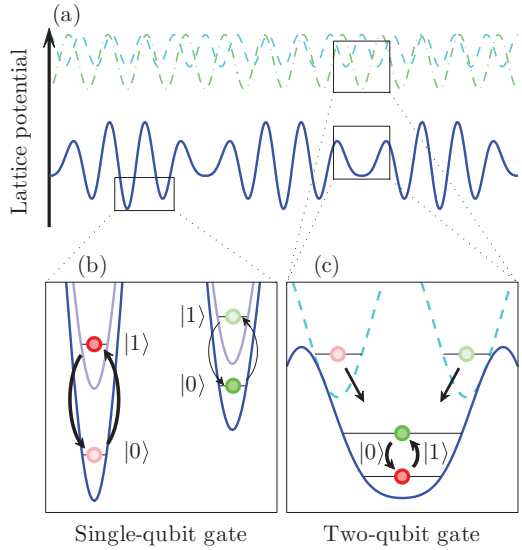

FIG. 1. (Color online) Overview of the superlattice and the single- and two-qubit spin-state gates. (a) Two optical lattice potentials are superimposed to to create a long-period superlattice. (b) The varying well depth throughout the superlattice results in a varying spin transition frequency for each atom. A microwave tuned to the transition of one atom (red), only partially switches another atom (green). If the partially switched population is kept sufficiently low, a single-qubit gate is realized. (c) When a lattice potential of longer wavelength is added to a lattice potential of shorter wavelength, two wells, each holding an atom, can be merged. Through control of phase and well depth, atoms are sent into the vibrational ground and first excited state, where they interact for an arbitrary amount of time, before reversing the process. The interaction causes a spin state exchange resulting in a two-qubit gate.

* sherson@phys.au.dk

period addressing lattice, superimposed on a conventional short-period lattice with an atomic filling of roughly one percent, has allowed the demonstration of unitary single-qubit gates with a fidelity of around 96% [38]. Similar techniques have also been used in optical cavities with multiple wavelength lattices [39, 40].

We propose a superlattice architecture in which both single- and two-qubit gates can be performed. The large period nature of our superimposed potentials allows selective addressing of individual lattice sites periodically spaced throughout the lattice as seen in Fig. 1(b) in analogy with the architecture presented in Ref. [38]. Here we present detailed calculations of the achievable gate speed versus lattice frequency and in particular focus on the optimum trade-off between speed and the detrimental effect of spontaneous emission. Two-qubit gates are facilitated by the merger and interaction of two initially separated atoms via spin-exchange as seen in Fig. 1(c). For both single- and two-qubit gates we demonstrate errors below 10^{-3} including experimental sources of error.

This paper is organized along the following lines. The combination of two optical lattice potentials to form a superlattice is introduced in section II. The ability to perform single-qubit gates by exploiting the differential ac-Stark shift is discussed in section III. The two-qubit gate using local collisional interactions is the subject of section IV, where numerical optimization is applied to determine minimum gate time and maximal fidelity. Section V summarises the paper's conclusions and highlights perspectives for the future.

II. LONG PERIOD SUPERLATTICE POTENTIAL

The dipole potential experienced by a ground-state alkali atom in an optical field with wavelength λ is [41],

$$\begin{aligned} &U(I(\mathbf{r}),\lambda,\mathcal{P}) \\ =&\frac{\pi c^2\Gamma}{2\omega_0^3}\left(\frac{2+\mathcal{P}g_F m_F}{\Delta_{2,F}(\lambda)}+\frac{1-\mathcal{P}g_F m_F}{\Delta_{1,F}(\lambda)}\right)I(\mathbf{r}). \end{aligned} \tag{1}$$

Here the optical polarization $\mathcal{P}=0,\pm1$ for linearly and circularly $\sigma^{\pm}$ polarized light respectively, g_F is the Landé factor and m_F the magnetic quantum number. $\Delta_{i,F}(\lambda)$ is the laser detuning given by $\Delta_{i,F}(\lambda)=\omega_{\text{laser}}(\lambda)-\omega_{i,F}$ where $i=1,2$ refers to the D_1 and D_2 lines. This equation is valid for large detunings such that $\Delta_{i,F}(\lambda)>\Delta_{\text{HFS}}$, the excited-state hyperfine splitting. In the case of two counter-propagating fields an optical lattice with a lattice spacing $a_{\text{lat}}=\lambda/2$ is formed.

Adding two optical lattice potentials of similar wavelength light creates a 1D long-period superlattice with potential wells of varying depth, as seen in Fig. 1(a). The length of one superlattice period (SLP) is $a_{\text{SLP}}=(\lambda_2^{-1}-\lambda_1^{-1})^{-1}/2$, three SLPs are seen in Fig. 1(a). In this work, we consider a SLP in which the longer period lattice passes through one less cycle than the shorter period lattice, leading to the relation $\lambda_1/\lambda_2=(n-1)/n$, where n is the number of cycles in a SLP with $\lambda_2<\lambda_1$.

III. SINGLE-QUBIT GATE

Throughout this work, we treat an array of single ^{87}Rb atoms confined to lattice sites as our starting point. Such a situation is readily realized through use of the superfluid to Mott-insulator transistion [1]. The different spin states $|0\rangle\equiv|F=1,1\rangle$ and $|1\rangle\equiv|F=2,2\rangle$ experience different potentials when using $\sigma^{\pm}$ polarized light, as shown in Eq. (1). The varying intensity of each well in a SLP, causes the hyperfine transition $\Delta U_i=U_i(|1\rangle)-U_i(|0\rangle)$ to differ for different atoms in lattice sites i. If a microwave π–pulse tuned to switch a target atom j is applied throughout the superlattice, the population P_i of all the atoms will oscillate $P_i=\frac{1}{2}\left(\frac{\chi_i}{\Omega_i}\right)^2[1-\cos^2(\Omega_i t)]$, where χ_i is the Rabi frequency, the generalized Rabi frequency $\Omega_i=\left(\chi_i^2+{\Delta_{\text{R}}^{ij}}^2\right)^{1/2}$ and $\Delta_{\text{R}}^{ij}=(\Delta U_i-\Delta U_j)/\hbar$ is the detuning of the transition of atom i compared to the transition of target atom j. Atoms in the selected wells are switched through a π–pulse, while each of the other atoms of the SLP are kept beneath a threshold population $P_{\text{t}}=(\chi_k/\Omega_k)^2$ where k denotes the site with minimal detuning. The detuning can be expressed through the threshold population $|\Delta_{\text{R}}^{ij}|=\chi_i[(1-P_{\text{t}})/P_{\text{t}}]^{1/2}\approx\chi_i P_{\text{t}}^{-1/2}$, with the approximation being valid for $P_{\text{t}}\ll1$. For a given threshold population, the π–pulse duration used to address the target atom can then be calculated $t_{\text{a}}=\pi/\sqrt{P_{\text{t}}}|\Delta_{\text{R}}^{ij}|$. Finding the fastest possible gate time thus reduces to calculating the detunings Δ_{R}^{ij} for all atoms $i\neq j$ in a SLP. We note that this is of course a conservative approach: with the detailed knowledge of all detunings in a SLP one may also engineer pulse durations that produce less residual excitation than P_{t}.

The one dimensional potential for atoms in the field of the two standing waves comes through Eq. (1) . The primary laser potential depth is one unit of recoil energy $E_{\text{r}}(\lambda)=h^2/2m\lambda^2$, while the wavelength and relative intensity of the secondary laser is varied through a scaling parameter A. The total potential is thus given by

$$\begin{aligned} &\frac{U_{\text{SL}}(x,\eta,A,\lambda_2,\mathcal{P}_1,\mathcal{P}_2)}{E_{\text{r}}(\lambda_1)} \\ =&-\eta\left[\cos^2(k_1x)+A\frac{U(\lambda_2,\mathcal{P}_2)}{U(\lambda_1,\mathcal{P}_1)}\cos^2(k_2x)\right], \end{aligned} \tag{2}$$

where $k_{1,2}$ are the wave numbers of the two lattice beams and η is an additional scaling factor. The minus sign arises from the fact that only red detuned light is taken into consideration.

The potential in a SLP is calculated for both hyperfine levels, and the difference $-|\Delta U(x)|$ is plotted in Fig. 2(a). This difference is similar in form to the SLP itself. To calculate the site dependent detunings, the potential minima of all wells within a SLP are found, as in Fig. 2(b). For all atoms, ΔU_i can then be found and the detuning $\hbar\Delta_{\text{R}}^{ij}/\eta E_{\text{r}}$ is given as the difference in hyperfine splitting as seen in Fig. 2(c). The smallest of all Δ_{R}^{ij} sets the threshold, and thus only that detuning is considered. Note that the potential minima of the superlattice do not exactly match the corresponding minima of $-|\Delta U(x)|$, which tends to increase the detunings. Additionally, the min-

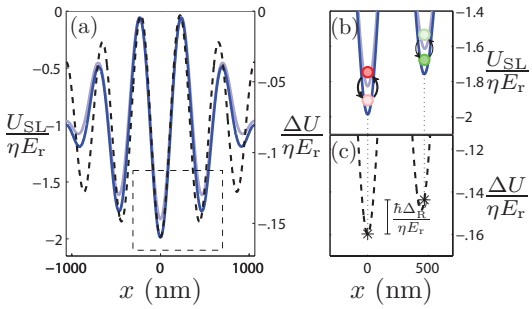

FIG. 2. (Color online) A schematic overview of the mechanism of the single-qubit gate and how the detuning $|\Delta_{\mathrm{R}}^{ij}|$ is calculated. (a) A plot of an entire SLP, with both hyperfine levels as the blue line and the light blue line (left axis) and an enlargement of the hyperfine splitting as the dashed black line (right axis). The section marked by the thin black dashed line is enlarged in (b) and (c). The values used to plot are $A = 0.28$, $\lambda_1 = 1064\,\mathrm{nm}$, $\lambda_2 = 4/5\lambda_1 = 851.2\,\mathrm{nm}$ and $\mathcal{P}_1 = \mathcal{P}_2 = 1$. (b) When exposed to precisely controlled microwave radiation the target atom is switched while keeping the switched population of neighbouring atoms under a threshold P_{t}. The positions of the atoms are calculated by taking the potential minima. (c) The positions of the atoms are used to calculate the hyperfine splitting of both atoms, and the detuning is the difference in this splitting, which in this example is $\hbar|\Delta_{\mathrm{R}}^{ij}|/\eta E_{\mathrm{r}} = 0.016$.

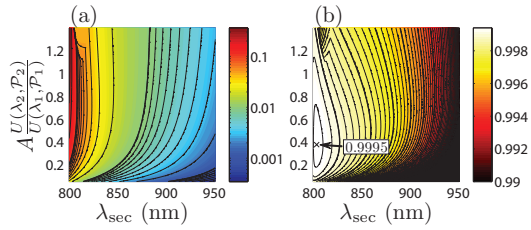

FIG. 3. (Color online) Results for single-qubit gate calculations. (a) The absolute detuning $\hbar|\Delta_{\mathrm{R}}^{ij}|/\eta E_{\mathrm{r}}$ calculated for an array of different wavelengths and secondary lattice depths. The contour lines represent logarithmic scaling. The addressing time can be calculated through the detuning via $t_{\mathrm{a}} = \pi/\sqrt{P_{\mathrm{t}}}|\Delta_{\mathrm{R}}^{ij}|$ with $E_{\mathrm{r}}/h \approx 2\,\mathrm{kHz}$. (b) The corresponding probabilities of an operation without scattering the target atom. There is a maximum of high probability 0.9995 and the thick and thin contour lines represent steps of 0.001 and 0.0002. The black area represent probabilities beneath 0.99. Calculated with $\lambda_1 = 1064\,\mathrm{nm}$ and $\mathcal{P}_1 = \mathcal{P}_2 = 1$.

ima of the different hyperfine levels do not match either, although, for the red detunings considered here, this position shift is typically several orders of magnitude smaller than the laser wavelengths. Since there is no position shift for the deepest well any neighboring well shifts only serve to restrict the transition of non–target atoms even further.

The detuning for a range of secondary lattice wavelengths and lattice depths is seen in Fig. 3(a). Using $E_{\mathrm{r}}/h \approx 2\,\mathrm{kHz}$ the largest shifts of Fig. 3 (a) result in gate time $\sim 100\mathrm{ms}/\eta$. Since lattices of 100-1000E_{r} can be realized routinely using high power lasers, gate times $0.1 - 1$ ms should be feasible. The largest detunings are seen close to the D_1 line and are generally larger when the lattice depths are similar. This seems to suggest that the single qubit gate should be performed at the lowest possible detuning. This conclusion changes when the probability of scattering a photon $p_{sc} = \exp(-\gamma_{\mathrm{sc}} t_{\mathrm{a}})$, during a gate operation is included. The scattering rate is calculated using [41]:

$$\gamma_{\mathrm{sc}}(\mathbf{r}) = \frac{\pi c^2 \Gamma^2}{2\hbar\omega_0^3}\left(\frac{2}{\Delta_{2,\mathrm{F}}^2} + \frac{1}{\Delta_{1,\mathrm{F}}^2}\right) I(\mathbf{r}), \tag{3}$$

and rewriting the expression similarly to Eq. (2) into $\gamma_{\mathrm{sc}}/E_{\mathrm{r}}$, including A and η. In calculating the scattering rate, three fixed retro–reflected lasers with equal intensities and wavelengths, one for each dimension, are included plus the secondary laser in a single dimension. When calculating p_{sc} only the target atom is taken into consideration. As both the detuning Δ_{R}^{ij} and scattering rate scale linearly with lattice depth, the gate–time scattering probability is independent of the depth and the scaling factor η.

The probabilities of a successful operation $1 - p_{\mathrm{sc}}$ are mapped in Fig. 3(b) for the detunings calculated in Fig. 3(a). At the optimum the maximum–probability of $1-p_{\mathrm{sc}} = 0.9995$ is reached. Increasing the primary wavelength increases the probability slightly, however, we have chosen to represent the results corresponding to $\lambda_1 = 1064$nm due to the high availability of such a laser system. Other polarizations have been tested, and the detunings Δ_{R}^{ij} were examined for j not being the atom in the deepest well; both yielding similar or worse results than those presented above. When scaling up to a longer period SL a naive estimate of the total probability of not scattering an atom for N atoms is the N^{th} power of the probability of not scattering the target atom. The result would scale poorly with hundreds of atoms as $0.9995^{100} \sim 0.95$. As can be seen in Fig. 2(a), however, the intensity will decrease away from the maximum one resulting in a reduced error probability at larger distances.

IV. TWO-QUBIT GATE

Having initialized an array of atoms in specific lattice sites, a two-qubit gate on a selected pair of neighboring atoms can be performed by exploiting the spin-exchange interaction. To achieve such a gate in this architecture requires the merging of two atoms in the same lattice site such that their wave functions overlap, as sketched in Fig. 1(c). The optimization of this non-trivial merger process is the subject of section IV B. In this section, we describe the gate mechanism and identify the requirements of performing such a gate in an optical superlattice. To minimize the gate time, we also numerically optimize the lattice depth and phase throughout the merging process and consider the detrimental effects of experimental preparation errors.

A. Gate description

The mechanism driving the two-qubit gate is the mutual interaction between two overlapping atoms which leads to spin exchange [9, 35, 42]. Two initially separated qubits are combined in the same well in the ground and first excited vibrational levels of the well

$$\begin{aligned} \alpha\,|1\rangle_{\rm L} + \beta\,|0\rangle_{\rm L} &\rightarrow \alpha\,|1\rangle_{\rm g} + \beta\,|0\rangle_{\rm g}\,, \\ \tilde{\alpha}\,|1\rangle_{\rm R} + \tilde{\beta}\,|0\rangle_{\rm R} &\rightarrow \tilde{\alpha}\,|1\rangle_{\rm e} + \tilde{\beta}\,|0\rangle_{\rm e}\,, \end{aligned} \tag{4}$$

where $|1\rangle$ and $|0\rangle$ denote the spin based qubit states, α, β, $\tilde{\alpha}$ and $\tilde{\beta}$ are the amplitudes, $|\cdot\rangle_{\rm L}$ and $|\cdot\rangle_{\rm R}$ denote the wave functions of the atoms in the left and right well, and $|\cdot\rangle_{\rm g}$ and $|\cdot\rangle_{\rm e}$ denote the wave functions of the atoms in the ground and excited vibrational levels of the merged well.

The two atoms in the merged well are identical bosons, so the two-particle wave function is symmetric under particle exchange. The new eigenenergy basis of the system is formed by the singlet and triplet states

$$\begin{aligned} |s\rangle &= \frac{1}{\sqrt{2}}\left(|1\rangle_{\rm g}\,|0\rangle_{\rm e} - |0\rangle_{\rm g}\,|1\rangle_{\rm e}\right), \\ |t_{-1}\rangle &= |0\rangle_{\rm g}\,|0\rangle_{\rm e}\,, \\ |t_0\rangle &= \frac{1}{\sqrt{2}}\left(|1\rangle_{\rm g}\,|0\rangle_{\rm e} + |0\rangle_{\rm g}\,|1\rangle_{\rm e}\right), \\ |t_{+1}\rangle &= |1\rangle_{\rm g}\,|1\rangle_{\rm e}\,. \end{aligned} \tag{5}$$

The two-qubit state of the atoms can now be expressed via the basis of singlet/triplet states as $|1\rangle_{\rm g}\,|0\rangle_{\rm e} = (|t_0\rangle + |s\rangle)/\sqrt{2}$ and $|0\rangle_{\rm g}\,|1\rangle_{\rm e} = (|t_0\rangle - |s\rangle)/\sqrt{2}$.

The singlet spin state $|s\rangle$ is antisymmetric, and hence its spatial wave function must be antisymmetric as well. In this wave function there is no density overlap between the two particles. The ultracold atoms primarily interact by contact, which means that there is negligible interaction in the state $|s\rangle$. However, the wave function of the symmetric spin state $|t_0\rangle$ must be symmetric, which leads to an interaction between the atoms and hence a change in energy $U_{\rm int}$ when compared to the state $|s\rangle$.

As the two-qubit state Ψ evolve in time, the energy shift between the two states $|s\rangle$ and $|t_0\rangle$ will induce a phase shift

$$\Psi(t) = \frac{1}{\sqrt{2}}(e^{iU_{\rm int}t/\hbar}\,|t_0\rangle + |s\rangle), \tag{6}$$

which will induce periodic oscillations between $|1\rangle_{\rm g}\,|0\rangle_{\rm e}$ and $|0\rangle_{\rm g}\,|1\rangle_{\rm e}$. At time $T_{\rm SWAP} = \pi\hbar/U_{\rm int}$ the spin states are swapped and at time $T_{\sqrt{\rm SWAP}} = \pi\hbar/2U_{\rm int}$ the entangling $\sqrt{\rm SWAP}$ gate is implemented, which is universal for quantum computation. The qubits can subsequently be separated by reversing the merging operation.

The gate time is set by the interaction between two ^{87}Rb atoms and can be modelled by an effective 1D contact potential [43, 44]

$$V_{\rm int}\,(|x_1 - x_2|) = g_{\rm 1D}\delta(x_1 - x_2)\,, \tag{7}$$

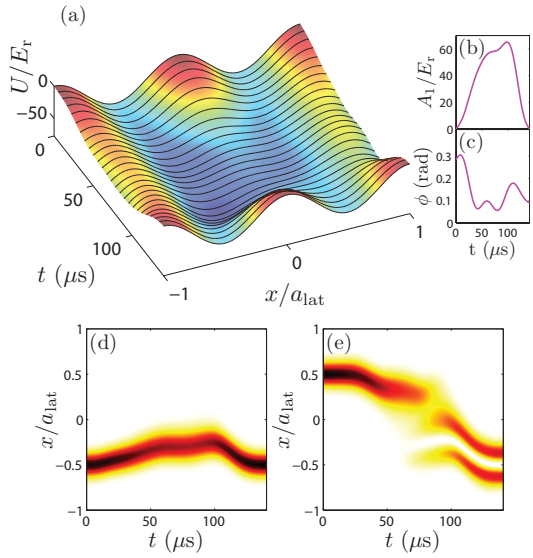

FIG. 4. (Color online) An example of the operation required to realize a two-qubit gate. (a) The time–evolution of the potential leading to two atoms being sent in to one well. (b)-(c) Optimal control pulses for the amplitude and phase of the primary lattice leading to the potential deformation seen in (a). Density profiles of the two atoms as a function of time illustrating the mapping of one atom into the excited state of a neighboring well (e), while the other atom ends in the ground state (d).

where x_1 and x_2 are the coordinates of the two atoms, δ is the Dirac delta function and $g_{\rm 1D}$ is the effective 1D coupling strength. This strength is given by $g_{\rm 1D} = 2a_{\rm s}h\sqrt{\nu_y\nu_z}$ where $a_{\rm s}$ is the scattering length of the atoms, h is the Planck constant and ν_y and ν_z are the trap frequencies in the y– and z–directions. For ^{87}Rb, the scattering length $a_{\rm s} = 110a_0$, where a_0 is the Bohr radius [45].

B. Lattice site merging

In this section we will show how, by controlling the phase and depth of an optical superlattice, one can merge pairs of interacting atoms into a single lattice site in which they can perform the SWAP gate described above. An illustration of the superlattice potential during the merging process is seen in Fig. 4(a) with the corresponding values of amplitude and phase of the added lattice seen in (b) and (c). The potential minimum of the right well is shifted towards the $-x$ direction so that both atoms move into the well at $x = -0.5a_{\rm lat}$. This is shown in Fig. 4(d) and (e) where the density profiles of the two atoms are seen as a function of time. After being initially separate, one atom is promoted to the first excited vibrational state while the other remains in the ground state. Starting from

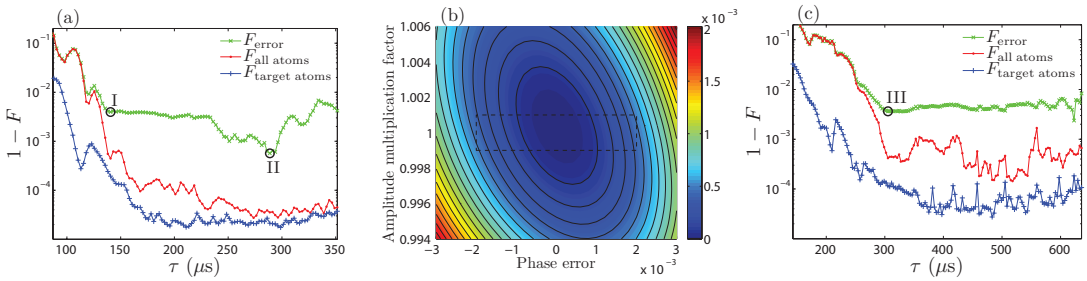

FIG. 5. (Color online) Fidelity, F for the simulations of the superlattice two-qubit gate. (a) Different fidelities obtained at different operation times with $n = 5$, with two results of interest highlighted as I and II. The optimized merging scheme at II corresponds to the example shown in Fig. 4. (b) The change in fidelity for II as a function of error also illustrating how F_{error} is calculated, i.e. by including all fidelities within the dashed lines and assuming the worst. The contour lines represent steps of 10^{-4}. (c) Results for the lattice configuration $n = 10$ with one more point of interest highlighted as III. The lattice beam wavelength, λ_2 is fixed at 1064 nm. Further results for I, II and III are seen in Table I.

the total optical lattice potential:

$$\frac{U(x)}{E_{\text{r}}(\lambda_2)} = -A_1 \cos^2(k_1 x + \phi) - A_2 \cos^2(k_2 x + \pi/2), \quad (8)$$

we search for the optimum values of phase and depth that merges atoms with the highest fidelity. This is achieved by using the split-step method to simulate the time-evolution of the atoms and optimizing using a simplex algorithm. During an operation, the primary laser phase, ϕ and depth A_1 are varied while the secondary laser phase and depth are fixed at $\pi/2$ and 1 $E_{\text{r}}(\lambda_2)$. A primary phase of $\phi = 0$ merges the wells at $x \approx 0$. Note that when combining atoms into a single well, merging is more easily achieved when a longer wavelength lattice is added to an initially populated short-wavelength lattice.

Precise experimental control of the lattice phases can be achieved in a retro-reflected optical lattice geometry by varying the primary beam frequency, $\Delta\nu$ to give a phase change $\Delta\phi = 2\pi d\Delta\nu/c$, where d is the distance to the retro–reflector mirror. To achieve $\Delta\phi = \pi$ with $\lambda = 1064$ nm and $d = 1$ m, a change in frequency $\Delta\nu = 150$ MHz is required. The fact that the dynamics is controlled using the laser frequency - one of the most well controlled quantities in physics - illustrates one of the appealing features of our proposal.

We choose to independently optimize the merger for three different fidelity classifications. The first, $F_{\text{target atoms}} = P_g P_e$, is the population of the two target atoms in the ground and excited states. To reflect the effects of the merger sequence on non-target atoms, we optimize a second fidelity, $F_{\text{all atoms}} = P_g P_e \prod_i P_{g,i}$ where i are the atoms in each SLP which are not involved in the gate. For each simulation, experimental sources of errors are added to the time dependent amplitude and phase of the added lattice corresponding to error in intensity and frequency. The sources of noise are assumed to be of a sufficiently low frequency to be considered constant during the operation and are therefore incorporated by adding a global shift to the obtained control pulses. Based on this, a third fidelity, F_{error}, is optimized which takes the worst obtained fidelity within the array of errors used, also including all atoms in the SLP.

The existence of several local maxima in the optimizational landscape neccessitated optimization starting from long times moving towards shorter times and vice-versa. At each point in time, the highest fidelity was selected.

Two secondary lattices wavelengths $\lambda_2 = 851.2$ nm and 957.6 nm and a primary lattice wavelength of $\lambda_1 = 1064$ nm are studied. These wavelengths correspond to $n = 5$ and $n = 10$ superlattices. The error boundaries used to optimize F_{error} are set to 0.1% for amplitude and a phase offset of 0.2%, as shown by the box in Fig. 5(b). As can be seen, with appropriate control of the phase (i.e. the relative frequency difference) one can tolerate power fluctuations of the order of 1%, while still remaining below 10^{-3} infidelity.

The total gate times for the SWAP and $\sqrt{\text{SWAP}}$ gates are set by calculating the interaction during the merging operation. For the SWAP ($\sqrt{\text{SWAP}}$) gate, the interaction induced phase shift is required to be $n_i\pi$ ($\frac{n_i\pi}{2}$), where n_i is an integer. The total phase shift picked up during the merging operation will also be picked up when reversing the merging operation to split up the atoms into separate wells again. When requiring a certain phase shift, a total gate time is then given by twice the operation time τ plus a time given by the stationary interaction. From the total gate times, the probabilities of scattering an atom in the SLP during a gate is calculated including spatially varying intensity and 1064 nm lattice in the y- and z-dimension with a depth of $32E_{\text{r}}$.

The resulting fidelities at different operation times τ are seen in Fig. 5(a) and (c). Three points of interest are I, II and III, and total gate times and scattering rates for these operations are shown in Table I.

Merging sequence II is also depicted in Fig. 4. In this case the operation is plotted without errors included. The change in fidelity when including various errors for II is seen in Fig. 5(b) where the area marked by the dashed line represent the errors included to optimize F_{error}. This high fidelity result is achieved at a modest operation time of less than 300 μs. Even choosing a larger SLP corresponding to $n = 10$, the operation time is comparable at a slightly reduced fidelity. This

TABLE I. Further results for the three highlighted merging processes I, II and III from Fig. 5. The total gate times T_{SWAP} and $T_{\sqrt{\text{SWAP}}}$ are calculated by requiring the total interaction to cause a fixed phase shift. From the the merging process, the probabilities $P_{\text{sc, SWAP}}$ and $P_{\text{sc, }\sqrt{\text{SWAP}}}$ of scattering an atom within the SLP during a gate are also calculated.

	$\tau(\mu s)$	F_{error}	$T_{\sqrt{\text{SWAP}}}(\mu s)$	$T_{\text{SWAP}}(\mu s)$	$P_{\text{sc, }\sqrt{\text{SWAP}}}$	$P_{\text{sc, SWAP}}$
I	141	0.9960	460	366	4.0×10^{-4}	3.2×10^{-4}
II	289	0.9994	634	728	5.5×10^{-4}	6.3×10^{-4}
III	305	0.9964	769	638	8.3×10^{-4}	7.0×10^{-4}

illustrates that larger qubit registers are feasible.

V. CONCLUSION

We have presented a novel architecture for quantum computing using the spatially dependent potential of neutral atoms in long periodicity optical superlattices implemented by superposing two optical lattices with close-lying periodicity. We have identified the fastest possible single-qubit gate times given a maximum tolerable rotation error on the remaining atoms at various different values of the lattice wavelengths. Including the detrimental effect of spontaneous emission, we show that gates in the sub-millisecond regime can be realized with less than 10^{-3} total error probability. The proposed two-qubit gate takes advantage of the fact that at the node of the superlattice period there is an isolated double well system in which merger can be realized by controlling the relative intensity and frequency of the two lattices. Controlling the relative phase of the two lattices the node can be positioned at an arbitrary pair of wells. We numerically optimize the merger to implement an entangling $\sqrt{\text{SWAP}}$ two-qubit gate. Including realistic sources of error and the accumulated errors of atoms not participating in the merger we still obtain total gate error probabilities of the order of 10^{-3} with periodicities up to $n = 10$. Future work will focus on extending the merging scheme to fractional n superlattices to achieve selectivity across even larger qubit registers and the optimization of custom pulse protocols [38] to increase the single qubit gate robustness. Finally, we would like to point out that although this work has focussed on the manipulation of individual atoms the method could also be used to select a single plane in a one dimensional lattices as an alternative to current techniques relying on magnetic field addressing [20, 22].

ACKNOWLEDGMENTS

The authors acknowledge support from the Danish Council for Independent Research, Natural Sciences, the Lundbeck Foundation and a Marie Curie IEF in FP7.

[1] M. Greiner, O. Mandel, T. Esslinger, T. W. Hänsch, and I. Bloch, Nature **415**, 39 (2002).
[2] C. Chin, M. Bartenstein, A. Altmeyer, S. Riedl, S. Jochim, J. H. Denschlag, and R. Grimm, Science (New York, N.Y.) **305**, 1128 (2004).
[3] M. W. Zwierlein, J. R. Abo-Shaeer, A. Schirotzek, C. H. Schunck, and W. Ketterle, Nature **435**, 1047 (2005).
[4] I. Bloch, J. Dalibard, and S. Nascimbène, Nature Physics **8**, 267 (2012).
[5] G. Brennen, C. Caves, P. Jessen, and I. Deutsch, Physical Review Letters **82**, 1060 (1999).
[6] D. Jaksch, H.-J. Briegel, J. I. Cirac, C. W. Gardiner, and P. Zoller, Physical Review Letters **82**, 1975 (1999).
[7] K. D. Nelson, X. Li, and D. S. Weiss, Nature Physics **3**, 556 (2007).
[8] E. Charron, E. Tiesinga, F. Mies, and C. Williams, Physical Review Letters **88**, 077901 (2002).
[9] M. Anderlini, P. J. Lee, B. L. Brown, J. Sebby-Strabley, W. D. Phillips, and J. V. Porto, Nature **448**, 452 (2007).
[10] O. Mandel, M. Greiner, A. Widera, T. Rom, T. W. Hänsch, and I. Bloch, Nature **425**, 937 (2003).
[11] D. Jaksch, J. Cirac, P. Zoller, S. Rolston, R. Côté, and M. Lukin, Physical Review Letters **85**, 2208 (2000).
[12] M. Müller, I. Lesanovsky, H. Weimer, H. Büchler, and P. Zoller, Physical Review Letters **102**, 170502 (2009).
[13] D. Mø ller, L. Madsen, and K. Mø lmer, Physical Review Letters **100**, 170504 (2008).
[14] L. Isenhower, E. Urban, X. L. Zhang, A. T. Gill, T. Henage, T. A. Johnson, T. G. Walker, and M. Saffman, Physical Review Letters **104** (2010), 10.1103/PhysRevLett.104.010503.
[15] T. Wilk, A. Gaëtan, C. Evellin, J. Wolters, Y. Miroshnychenko, P. Grangier, and A. Browaeys, Physical Review Letters **104**, 010502 (2010).
[16] E. Kuznetsova, M. Gacesa, S. F. Yelin, and R. Côté, Physical Review A **81**, 030301 (2010).
[17] M. Saffman, Optics Letters **29**, 1016 (2004).
[18] J. Cho, Physical Review Letters **99**, 020502 (2007).
[19] A. V. Gorshkov, L. Jiang, M. Greiner, P. Zoller, and M. D. Lukin, Physical Review Letters **100**, 093005 (2008).
[20] D. Schrader, I. Dotsenko, M. Khudaverdyan, Y. Miroshnychenko, A. Rauschenbeutel, and D. Meschede, Physical Review Letters **93**, 150501 (2004).
[21] W. S. Bakr, J. I. Gillen, A. Peng, S. Fölling, and M. Greiner, Nature **462**, 74 (2009).
[22] J. F. Sherson, C. Weitenberg, M. Endres, M. Cheneau, I. Bloch, and S. Kuhr, Nature **467**, 68 (2010).
[23] C. Weitenberg, M. Endres, J. F. Sherson, M. Cheneau, P. Schauß, T. Fukuhara, I. Bloch, and S. Kuhr, Nature **471**, 319 (2011).
[24] T. Calarco, E. Hinds, D. Jaksch, J. Schmiedmayer, J. Cirac, and P. Zoller, Physical Review A **61**, 022304 (2000).
[25] H.-J. Briegel, T. Calarco, D. Jaksch, J. I. Cirac, and P. Zoller, Journal of Modern Optics **47**, 415 (2000).
[26] A. Negretti, T. Calarco, M. A. Cirone, and A. Recati, Eur. Phys. J. D **32**, 119 (2005).
[27] U. Dorner, T. Calarco, P. Zoller, A. Browaeys, and P. Grangier, Journal of Optics B: Quantum and Semiclassical Optics **7**, S341 (2005).
[28] M. A. Cirone, A. Negretti, T. Calarco, P. Krüger, and J. Schmiedmayer, The European Physical Journal D **35**, 165

(2005).
[29] E. Charron, M. Cirone, A. Negretti, J. Schmiedmayer, and T. Calarco, Physical Review A **74**, 012308 (2006).
[30] A. Negretti, A. Benseny, J. Mompart, and T. Calarco, Quantum Information Processing **12**, 1439 (2012).
[31] M. C. Tichy, M. K. Pedersen, K. Mø lmer, and J. F. Sherson, Physical Review A **87**, 063422 (2013).
[32] M. Gajdacz, T. Opatrný, and K. K. Das, arXiv:1207.3108 (2012).
[33] L. You and M. Chapman, Physical Review A **62**, 052302 (2000).
[34] T. Calarco, U. Dorner, P. Julienne, C. Williams, and P. Zoller, Physical Review A **70**, 012306 (2004).
[35] C. Weitenberg, S. Kuhr, K. Mø lmer, and J. Sherson, Physical Review A **84**, 032322 (2011).
[36] S. Fölling, S. Trotzky, P. Cheinet, M. Feld, R. Saers, A. Widera, T. Müller, and I. Bloch, Nature **448**, 1029 (2007).
[37] S. Peil, J. Porto, B. Tolra, J. Obrecht, B. King, M. Subbotin, S. Rolston, and W. Phillips, Physical Review A **67** (2003).
[38] J. H. Lee, E. Montano, I. H. Deutsch, and P. S. Jessen, Nature communications **4**, 2027 (2013).
[39] N. Brahms, T. P. Purdy, D. W. C. Brooks, T. Botter, and D. M. Stamper-Kurn, Nature Physics **7**, 604 (2011).
[40] T. Botter, D. W. C. Brooks, S. Schreppler, N. Brahms, and D. M. Stamper-Kurn, Physical Review Letters **110**, 153001 (2013).
[41] R. Grimm and M. Weidemüller, Advances in Atomic, Molecular and Optical Physics **42**, 95 (2000).
[42] D. Hayes, P. Julienne, and I. Deutsch, Physical Review Letters **98**, 070501 (2007).
[43] M. Olshanii, Physical Review Letters **81**, 938 (1998).
[44] G. De Chiara, T. Calarco, M. Anderlini, S. Montangero, P. Lee, B. Brown, W. Phillips, and J. Porto, Physical Review A **77**, 052333 (2008).
[45] H. M. J. M. Boesten, C. C. Tsai, J. R. Gardner, D. J. Heinzen, and B. J. Verhaar, Physical Review A **55**, 636 (1997).

A.2 A Simple Laser Locking System Based on a Field-Programmable Gate Array

It is highly necessary to have laser sources with stable frequencies to perform experimental physics with ultracold gases. Here, a simple laser locking system based on a field-programmable gate array is presented. Technological advances allows analog electronics to be replaced by a digital field-programmable gate array, which permits rapid reconfiguration. The system is able to stabilize a laser sufficiently for atom trapping and cooling applications.

A simple laser locking system based on a field-programmable gate array

N. B. Jørgensen,[1] D. Birkmose,[1] K. Trelborg,[1] L. Wacker,[1] N. Winter,[1] A. J. Hilliard,[1] M. G. Bason,[1,2] and J. J. Arlt[1]

[1)] *Department of Physics and Astronomy, Aarhus University, Ny Munkegade 120, 8000 Aarhus C, Denmark*

[2)] *School of Physics & Astronomy, University of Nottingham, Nottingham NG7 2RD, United Kingdom*

(Dated: 11 July 2016)

Frequency stabilization of laser light is crucial in both scientific and industrial applications. Technological developments now allow analog laser stabilization systems to be replaced with digital electronics such as field-programmable gate arrays, which have recently been utilized to develop such locking systems. We have developed a frequency stabilization system based on a field-programmable gate array, with emphasis on hardware simplicity, which offers a user-friendly alternative to commercial and previous home-built solutions. Frequency modulation, lock-in detection and a proportional-integral-derivative controller are programmed on the field-programmable gate array and only minimal additional components are required to frequency stabilize a laser. The locking system is administered from a host-computer which provides comprehensive, long-distance control through a versatile interface. Various measurements were performed to characterize the system. The linewidth of the locked laser was measured to be $0.7 \pm 0.1\,\mathrm{MHz}$ with a settling time of 10 ms. The system can thus fully match laser systems currently in use for atom trapping and cooling applications.

I. INTRODUCTION

Lasers are an essential technology in industry and scientific research. The frequency of the emitted light is usually determined by the laser gain profile and the length of the resonator cavity. Due to external perturbations such as temperature drifts or acoustic noise, the laser frequency drifts. For many applications, these drifts are not critical, but scientific and some advanced industrial applications often require precise frequency stabilization. Feedback circuits that stabilize the laser frequency have therefore been in use for decades. These circuits typically compare the laser frequency to a stable reference, e.g. by performing spectroscopy, and use a proportional-integral-derivative (PID) controller to provide a correction signal to control elements in the laser.

The field of atomic and molecular physics sets particularly strict demands on the laser frequency stability. To cool and trap atoms, lasers are typically frequency stabilized using an atomic transition or a high finesse cavity. Several different strategies have been developed to obtain a locking signal from a spectroscopic measurement[1–5]. Often, the technique of saturated absorption spectroscopy combined with lock-in detection is used to produce a locking signal which is insensitive to non-frequency fluctuations of the laser[5–7].

Laser cooling and trapping experiments have become widespread in modern research laboratories and commercial products for the implementation of the required laser systems are available. The necessary components for such a system can, however, also be constructed in-house. Such an approach can be used to build low-cost setups to generate cold and ultracold atomic samples in undergraduate level laboratories[7–12]. A significant hurdle in such a setup is the construction of a laser frequency stabilization system which typically requires extensive analog electronics.

In this article, we present a laser locking system for frequency stabilization based on a field-programmable gate array (FPGA), which has several advantages compared to both analog electronics and commercial systems. It offers rapid reconfigurability, a user-friendly interface, it is low-cost and easy to contruct.

Several FPGA-based devices have been developed in the field of atomic and molecular physics[13–18], including various laser locking systems[15–18]. The first demonstration of a FPGA-based laser lock realized a side of fringe lock to a cavity[15]. Later, a dedicated stand-alone system including parallel slow and fast feedback was contructed which achieved a linewidth in the kHz regime[17]. The most recent dedicated FPGA-based lock system was employed to stabilize a fibre laser to the precision required in an atomic clock[18]. Alternatively, a FPGA-based loop to optically phase-lock two lasers have been developed[16].

As an alternative to previous FPGA-based locks, we present a simple and versatile solution which is easy to implement. The system is fully applicable for challenging scientific applications such as cooling and trapping neutral atoms, but requires minimal additional electronics. It is based on a single off-the-shelf board which includes a FPGA, a microprocessor, analog-to-digital and digital-to-analog converters. Furthermore, this is the first FPGA-based lock programmed in LabVIEW, which significantly simplifies the task of understanding and reprogramming the software. This additionally allows for a versatile graphical user interface and long distance control.

The paper is structured as follows. In Sec. II, the procedure to obtain a locking signal is reviewed, followed by a description of the FPGA implementation in Sec. III. Optimization and characterization of the locking system is presented in Sec. IV and conclusions are drawn in Sec. V.

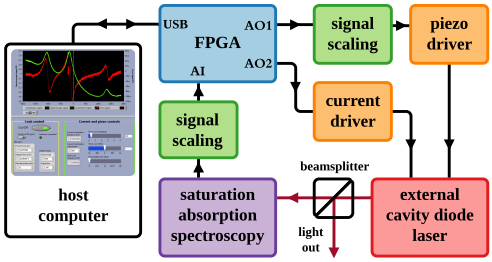

FIG. 1. Overview of the feedback system with the main electronic signals (black lines) and light signals (red lines) displayed. The current and piezo drivers that supply the ECDL recieve their inputs from the FPGA. Laser light is sent to a saturated absorption spectroscopy setup, which produces the spectroscopy signal fed back to the FPGA.

II. PEAK LOCK FOR ATOMIC PHYSICS

The laser locking system was developed for laser cooling and trapping of neutral atoms, where linewidths well below the typical atomic transition linewidths of approximately 5 MHz are required. This is achieved by stabilizing the laser frequency to a spectroscopy signal obtained in an atomic vapor cell. Since the Doppler-broadened signal provides insufficient frequency precision, Doppler-free saturation absorption spectroscopy is used[5].

The design schematic of the feedback system is shown in Fig. 1. The FPGA controls an External Cavity Diode Laser (ECDL)[19] by providing input to its current driver and to the piezo driver that controls the position of the frequency selective grating inside the laser. The signal obtained from saturated absorption spectroscopy, is analyzed within the FPGA which then performs feedback accordingly.

To perform feedback, an error signal is required, which is proportional to the difference between a desired setpoint and the actual laser frequency. A PID controller attempts to minimize this error signal according to a proportional, an integral and a derivative term which respectively account for present, past and possible future values of the error signal. Each of the three terms contain a tunable coefficient, referred to a P, I and D parameters, which allow the strength of the terms to be adjusted.

The derivative of a spectroscopic signal provides a steep, linear zero crossing at an atomic resonance position and is thus well suited as an error signal. To obtain this derivative, heterodyne spectroscopy is employed[20]. In this technique, the laser frequency is modulated with a frequency ω_m, which produces two weak sidebands at $\pm\omega_\mathrm{m}$. After passing through the vapor cell, the laser intensity I is measured on a photodiode. In the limit of small modulation amplitude M, the detected light intensity is given by

$$I(t) = I_0\left[1 + M\delta\cos(\omega_\mathrm{m}t) + M\phi\sin(\omega_\mathrm{m}t)\right],$$

where I_0 is the intensity of the laser without modulation, δ is proportional to the difference in loss experienced by the two sidebands and ϕ is proportional to the difference between the phase shift experienced by the laser frequency and the average of the phase shifts experienced by the sidebands[6]. If ω_m is small compared to the width of the spectral feature, δ corresponds to the derivative of the spectroscopy signal and ϕ to the second derivative of the dispersion.

The demodulation of the signal is implemented through multiplication. An additional sinusoidal signal with frequency ω_m and phase θ is introduced and multiplied with the spectroscopy signal

$$I(t)\cos(\omega_\mathrm{m}t+\theta) = \frac{I_0 M}{2}\Big[\delta\cos(\theta) - \phi\sin(\theta) + \frac{2}{M}\cos(\omega_\mathrm{m}t+\theta) + \delta\cos(2\omega_\mathrm{m}t+\theta) + \phi\sin(2\omega_\mathrm{m}t+\theta)\Big].$$

The resulting signal contains three terms which depend on ω_m; in practice these are eliminated by a low-pass filter. Finally, by adjusting θ to zero, ϕ is eliminated and the derivative δ is obtained and available for feedback.

III. FPGA IMPLEMENTATION

Our laser frequency stabilization system is based on a National Intruments myRIO-1900 device, which is a hardware platform containing a programmable FPGA, a microprocessor, analog-to-digital and digital-to-analog converters[21]. The device can easily be accessed and programmed using LabVIEW software. No custom FPGA functions have been used in our implementation, making the software highly transferable to other LabVIEW based FPGA systems. The source code of the software used in this work is available online along with future versions[22].

The FPGA delivers the input to the current and piezo drivers, receives a signal from the spectroscopy setup and performs the feedback. The frequency modulation is realized by modulating the diode current, and the feedback is performed by adjusting the piezo voltage. The data flow within the FPGA is outlined in Fig. 2 and discussed in the following paragraphs.

The laser used in the setup is a home-built ECDL[19]. It delivers light at 780 nm and the spectroscopy and stabilization is performed using a rubidium vapour cell containing the two isotopes ^{87}Rb and ^{85}Rb in their natural abundances. In the following, the laser is locked to the crossover peak between the $F = 2 \rightarrow F' = 2$ and $F = 2 \rightarrow F' = 3$ transitions of the ^{87}Rb-D2 line[23], but any other spectroscopic feature could equally well be chosen.

The locking system is controlled from a host computer using an interface which displays all relevant data as

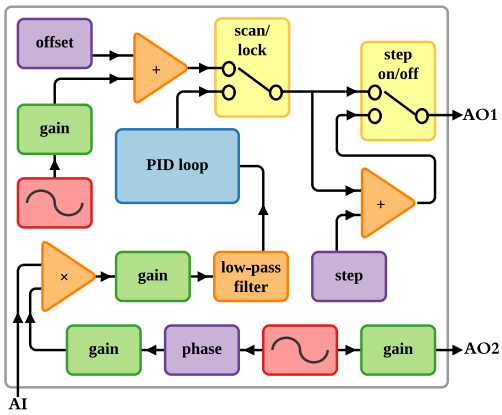

FIG. 2. Dataflow within the FPGA. Before the signal enters the FPGA, it is digitized to a 12 bit signal, which is further upconverted to 16 bit within the FPGA. Finally, all signals are converted to 12 bit before digital-to-analog conversion. The signal paths are further explained in the text.

shown in Fig. 3. The modulation of the laser current to produce sidebands is generated by a digital sine wave generator and sent to the analog output AO2. The spectroscopy signal is scaled to match the voltage range of the analog-to-digital converter (see Fig. 1), then it is digitized, and sent to the FPGA via the input channel AI. It is then multiplied with the phase-shifted modulation signal and by applying a filter, the error signal has been obtained. The low-pass filter used is a 4th order Butterworth filter implemented with a cut-off frequency of 500 Hz, removing the modulation signal of several kHz. Subsequently, the error signal enters the PID controller, which then produces a feedback signal accordingly.

It is often necessary to scan the laser over a range of frequencies to locate and resolve the spectroscopic features for locking. Thus, two different modes of operation are required: a locked mode and a scan mode. In scan mode, a broad range of frequencies is scanned and in lock mode, the feedback stabilizes the laser frequency to a given feature.

When the system is in scan mode, a piezo voltage scan signal is generated by a second digital sine wave generator and sent to the output channel AO1 which supplies the input signal to the piezo driver. In locked mode, the piezo signal is supplied by the PID controller. A key property of the feedback system is its response to a sudden disturbance. A switch has been implemented which can add an offset to the piezo signal, allowing a straightforward test of the step response of the system.

In order to display the obtained data and control the system, the spectroscopy signal, the error signal and the piezo signal is transferred from the FPGA to the host computer. Since the myRIO only has two built-in DC-coupled analog outputs, the AC coupled stereo audio output channel is utilized to allow independent external monitoring of the error signal.

IV. LOCK PERFORMANCE

In this section, the optimization and characterization of the locking system is described. This includes a measurement of the system response as a function of the modulation frequency and the implementation of a step response technique, which allows for an optimization of the settling time. Furthermore, the locking performance is determined by measuring the power spectral density of the frequency fluctuations and the linewidth of the laser through beat measurements.

The primary goal of the laser lock is to obtain fast recoveries from disturbances. This is dependent on the steepness of the error signal slope which in turn depends on the modulation frequency. Since the modulation frequency sets the upper limit for the bandwidth of the locking circuit, a low modulation frequency is undesirable. Additionally, the absorption difference experienced by the sidebands is lower for small modulation frequencies. At high frequencies, technical limitations such as the bandwidth of the system originating from the speed of the FPGA are relevant.

To optimize the slope of the locking signal, it was measured for a range of modulation frequencies with constant modulation amplitude as shown in Fig. 4. Each measurement was repeated five times and the slope was found using a linear fit. The highest locking signal derivative is obtained at 4–5 kHz.

The error signal slope was also measured as a function of the modulation signal amplitude, which displayed a linear dependence for small and moderate amplitudes. A large slope is preferable for the system to react to disturbances, but the linewidth grows at large modulation amplitudes. Hence, depending on the purpose of the laser, the modulation amplitude should be adjusted accordingly.

In the first experiments with the locked laser, the PID parameters were optimized using the step response technique. The Nichols-Ziegler method[24] served as a starting point. Subsequently, the parameters were adjusted to minimise the step response time. A disturbance to the locked laser was introduced through the step switch programmed into the FPGA (see Fig. 2). The step response time was defined as the time it took from the beginning of the disturbance until the spectroscopy signal returned to its locked value $\pm 1\sigma$ of the noise level.

Part of this optimization is shown in Fig. 5, where the step response time was recorded for different values of the P parameter for constant I and D parameters. Each data point shows the average of five measurements. It is evident that the response time decreases with increasing values of P, until substantial oscillations set in. The response for the optimum value is displayed in the inset

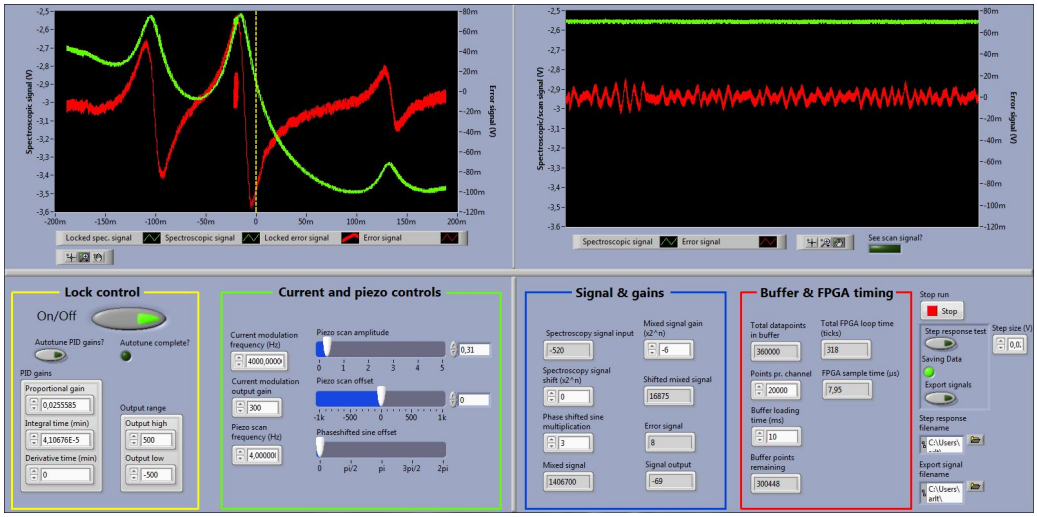

FIG. 3. User interface in locked mode. The interface is divided into four panels. The upper left panel shows the spectroscopic signal (green) and the error signal (red) versus the piezo scan value. In locked mode, the latest scan image is frozen and the PID loop is active. In this case, the spectroscopic signal and error signal are displayed on top of the frozen image. The central peak displayed is the crossover peak between the $F = 2 \rightarrow F' = 2$ and $F = 2 \rightarrow F' = 3$ transitions of the ^{87}Rb-D2 line, which the laser is locked to. The upper right panel displays the spectroscopic and error signal for a timespan of 160 ms, which is convenient to track the lock situation. The locking controls are located in the lower left panel where current modulation, piezo scan and PID parameters can be chosen and the status can be switched between lock and scan mode. The lower right panel displays the internal FPGA signals and additional gains can be adjusted. In the far right corner, there is a panel to export data.

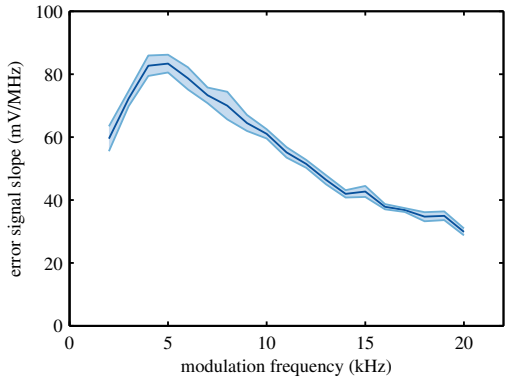

FIG. 4. Slope of the error signal versus modulation frequency. The shaded area is the standard error of the mean for five measurements.

figure, where the spectroscopy signal settles in 10 ms.

To determine the performance of the laser locking system, the power spectral density of frequency fluctuations was measured in unlocked and locked mode. The measurement was performed by recording a 5 s trace of the error signal digitally within the FPGA at a sample rate of 125 kHz. In both cases the frequency of the laser was tuned to the crossover peak of ^{87}Rb.

The results are displayed in Fig. 6 where the Fourier transformation of the signal has been taken. In frequency space, each data point is averaged with its 50 nearest neighbours to give a good estimate of the true mean value in each segment. A clear damping of the noise is observed at lower frequencies when locked, demonstrating the ability to correct for frequency drifts. A noise increase is seen at ~ 300 Hz, corresponding to the bandwidth of the feedback system. The narrow peak at 100 Hz is electronic noise and the current modulation of 4 kHz is also visible in the spectrum. It is likely that the 800 Hz peak orignates from the myRIO device which contains an accelerometer that operates at that sample rate.

The observed frequency noise can be compared with the step response signal shown in the inset of Fig. 5. The bandwidth of some 100 Hz matches the step response time of 10 ms and the high frequency noise of the spectroscopy signal originates from the 4 kHz modulation.

The oscillations observed after 10 ms are damped further on longer time scales and correspond to the bandwidth of the feedback. Depending on the choice of PID parameters, a faint oscillation remains due to a slight overcompensation of the feedback. Usually, the oscilla-

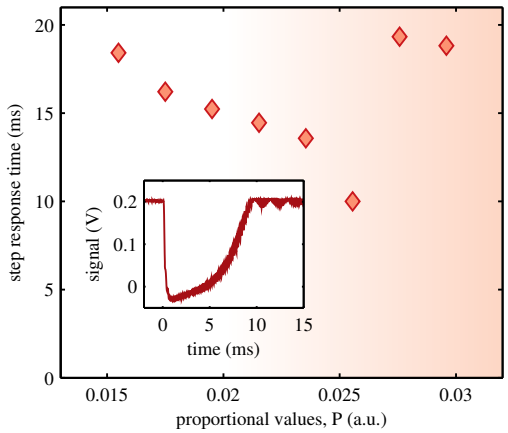

FIG. 5. Settling time for different values of the P parameter. The shaded area indicate the appearence of oscillations. The inset shows a spectroscopy signal for the minimum step response time of 10 ms.

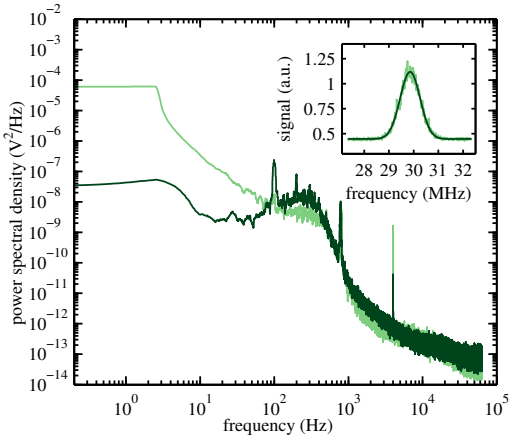

FIG. 6. Power spectral density of frequency fluctuations of the laser when unlocked (light green line) and when locked (dark green line). The inset shows one of the beat measurements (light green), which is used to determine the linewidth of the laser by applying a Gaussian fit (dark green line).

tions are not visible in the spectroscopic signal, but only in the error signal as can be observed in the right panel of Fig. 3.

The long-term stability of the system was tested by leaving it untouched, and in this case the laser remained locked for up to one day. The main limitation to this stability is the mechanical construction of the ECDL.

Finally, the linewidth of the laser was determined. A series of beat measurements was performed with two other lasers of similar design and wavelength. Those lasers are currently in use for the production of ^{87}Rb Bose-Einstein condensates[25] and locked using home-built analog PID controllers acting on a locking signal derived from a 10 MHz modulation of the laser current. For these measurements, all lasers were locked to the crossover peak of ^{87}Rb and acousto-optical modulators were used to shift each pair of lasers to be separated in frequency by ≈ 30 MHz. For each measurement, the beams of two lasers were coupled into a single-mode polarization maintaining fiber to ensure good spatial mode overlap. The fiber output was then directed onto a photodiode and the beat signal was obtained using a spectrum analyzer which recorded spectra at sweeptimes of 500 ms.

An example of such a beat measurement is shown in the inset of Fig. 6. The beat spectrum is composed of a Lorentzian profile due to high frequency noise of the laser and a Gaussian profile due to the drift of the laser within an individual measurement. The signal to noise ratio of our specific setup only allowed the Gaussian component to be resolved. This is fully sufficient, since the Gaussian component determines the effective linewidth in these types of laser systems.

The linewidth of the FPGA-based laser system was found to be 0.7 ± 0.1 MHz using low modulation amplitudes. The other two lasers tested were found to have linewidths of 0.4 ± 0.1 MHz and 0.6 ± 0.1 MHz. No significant alterations of the linewidths were observed for the range of sweeptimes 100–500 ms. Thus, our new laser locking system performs similarly to laser systems currently in use for experiments with ultracold atoms.

V. CONCLUSION

We have developed a simple FPGA-based laser locking system for frequency stabilization. It was optimized and characterized in a series of measurements, which demonstrates the flexibility of the system. The measured laser linewidth was 0.7 ± 0.1 MHz, similar to linewidths of lasers which are currently in use for laser cooling and trapping experiments.

Compared to initial results from FPGA-based locks, this is an improvement by more than a factor of two[15]. On the other hand, our laser-lock does not achieve linewidths comparable to dedicated locks for high precision experiments[17,18].

In contrast, our objective was to develop a simple laser locking solution based on low-cost off-the-shelf hardware, which requires minimal effort to implement in any setting, yet still acheives a performance sufficient for complex tasks such as cooling and trapping of neutral atoms. It was programmed using LabVIEW which is a standard experimental control language and thus the system is easy to understand, construct and configure and is applicable in both state of the art laboratories, teaching environments and remote sensing applications.

VI. ACKNOWLEDGMENTS

We thank the Danish Council for Independent Research, the Lundbeck Foundation, the Templeton Foundation, and a Marie Curie IEF in FP7 for support.

[1] C. Wieman and T. W. Hänsch, Physical Review Letters **36**, 1170 (1976).
[2] J. H. Shirley, Optics Letters **7**, 537 (1982).
[3] K. Overstreet, J. Franklin, and J. Shaffer, Review of scientific instruments **75**, 4749 (2004).
[4] G. Jundt, G. Purves, C. Adams, and I. Hughes, Eur. Phys. J. D **27**, 273 (2003).
[5] W. Demtröder, *Laser Spectroscopy: Basic Concepts and Instrumentation*, 3rd ed. (Springer, Berlin, 2003).
[6] G. Bjorklund, M. Levenson, W. Lenth, and C. Ortiz, Applied Physics B **32**, 145 (1983).
[7] K. B. MacAdam, A. Steinbach, and C. Wieman, Am. J. Phys. **60**, 1098 (1992).
[8] C. Wieman, G. Flowers, and S. Gilbert, Am. J. Phys. **63**, 317 (1995).
[9] A. Arnold, J. Wilson, and M. Boshier, Rev. Sci. Instrum. **69**, 1236 (1998).
[10] A. S. Mellish and A. C. Wilson, Am. J. Phys. **70**, 965 (2002).
[11] K. Singer, S. Jochim, M. Mudrich, A. Mosk, and M. Weidemüller, Rev. Sci. Instrum. **73**, 4402 (2002).
[12] D. L. Whitaker, A. Sharma, and J. M. Brown, Rev. Sci. Instrum. **77**, 126101 (2006).
[13] A. Restelli, R. Abbiati, and A. Geraci, Rev. Sci. Instrum. **76**, 093112 (2005).
[14] S. N. Nikolić, V. Batić, B. Panić, and B. M. Jelenković, Rev. Sci. Instrum. **84** (2013), 10.1063/1.4811147.
[15] A. Schwettmann, J. Sedlacek, and J. P. Shaffer, Rev. Sci. Instrum. **82**, 103103 (2011).
[16] Z. Xu, X. Zhang, K. Huang, and X. Lu, Rev. Sci. Instrum. **83**, 093104 (2012).
[17] G. Yang, J. F. Barry, E. S. Shuman, M. H. Steinecker, and D. DeMille, Journal of Instrumentation **7**, P10026 (2012).
[18] D. Leibrandt and J. Heidecker, Rev. Sci. Instrum. **86**, 123115 (2015).
[19] L. Ricci, M. Weidemüller, T. Esslinger, A. Hemmerich, C. Zimmermann, V. Vuletic, W. König, and T. W. Hänsch, Optics Communications **117**, 541 (1995).
[20] R. Drever, J. L. Hall, F. Kowalski, J. Hough, G. Ford, A. Munley, and H. Ward, Applied Physics B **31**, 97 (1983).
[21] The datasheet of the myRIO device is available online at http://www.ni.com/pdf/manuals/376047a.pdf.
[22] Updated source code is available online at http://phys.au.dk/forskning/forskningsomraader/uqgg0/downloads/.
[23] A crossover peak is located between two regular transitions and is a consequence of a specific non-zero velocity class of atoms being simultaneously resonant with the counterpropagating pump and probe beams.
[24] J. G. Ziegler and N. B. Nichols, trans. ASME **64** (1942).
[25] P. L. Pedersen, M. Gajdacz, F. Deuretzbacher, L. Santos, C. Klempt, J. F. Sherson, A. J. Hilliard, and J. J. Arlt, Phys. Rev. A **89**, 051603 (2014).

BIBLIOGRAPHY

[1] N. Bohr, On the constitution of atoms and molecules, Philos. Mag. **26**, 476–502 (1913).

[2] M. H. Anderson, J. R. Ensher, M. R. Matthews, C. E. Wieman, and E. A. Cornell, Observation of Bose-Einstein condensation in a dilute atomic vapor, Science **269**, 198–201 (1995).

[3] K. B. Davis, M.-O. Mewes, M. R. Andrews, N. J. van Druten, D. S. Durfee, D. M. Kurn, and W. Ketterle, Bose-Einstein condensation in a gas of sodium atoms, Phys. Rev. Lett. **75**, 3969–3973 (1995).

[4] J. P. Dowling and G. J. Milburn, Quantum technology: the second quantum revolution, Philos. Trans. R. Soc. London A **361**, 1655–1674 (2003).

[5] R. P. Feynman, Simulating physics with computers, Int. J. Theor. Phys. **21**, 467–488 (1982).

[6] I. Bloch, J. Dalibard, and S. Nascimbene, Quantum simulations with ultracold quantum gases, Nat. Phys. **8**, 267–276 (2012).

[7] I. Bloch, J. Dalibard, and W. Zwerger, Many-body physics with ultracold gases, Rev. Mod. Phys. **80**, 885–964 (2008).

[8] C. Chin, R. Grimm, P. Julienne, and E. Tiesinga, Feshbach resonances in ultracold gases, Rev. Mod. Phys. **82**, 1225–1286 (2010).

[9] P. Massignan, M. Zaccanti, and G. M. Bruun, Polarons, dressed molecules and itinerant ferromagnetism in ultracold Fermi gases, Rep. Prog. Phys. **77**, 034401 (2014).

[10] P. Naidon and S. Endo, Efimov physics: a review, Rep. Prog. Phys. **80**, 056001 (2017).

[11] A. Schirotzek, C.-H. Wu, A. Sommer, and M. W. Zwierlein, Observation of Fermi polarons in a tunable Fermi liquid of ultracold atoms, Phys. Rev. Lett. **102**, 230402 (2009).

[12] N. Navon, S. Nascimbene, F. Chevy, and C. Salomon, The equation of state of a low-temperature Fermi gas with tunable interactions, Science **328**, 729–732 (2010).

[13] C. Kohstall, M. Zaccanti, M. Jag, A. Trenkwalder, P. Massignan, G. M. Bruun, F. Schreck, and R. Grimm, Metastability and coherence of repulsive polarons in a strongly interacting Fermi mixture, Nature **485**, 615–618 (2012).

[14] M. Koschorreck, D. Pertot, E. Vogt, B. Fröhlich, M. Feld, and M. Köhl, Attractive and repulsive Fermi polarons in two dimensions, Nature **485**, 619–622 (2012).

[15] M. Cetina, M. Jag, R. S. Lous, I. Fritsche, J. T. Walraven, R. Grimm, J. Levinsen, M. M. Parish, R. Schmidt, M. Knap, and E. Demler, Ultrafast many-body interferometry of impurities coupled to a Fermi sea, Science **354**, 96–99 (2016).

[16] F. Scazza, G. Valtolina, P. Massignan, A. Recati, A. Amico, A. Burchianti, C. Fort, M. Inguscio, M. Zaccanti, and G. Roati, Repulsive Fermi polarons in a resonant mixture of ultracold ^{6}Li atoms, Phys. Rev. Lett. **118**, 083602 (2017).

[17] N. B. Jørgensen, L. Wacker, K. T. Skalmstang, M. M. Parish, J. Levinsen, R. S. Christensen, G. M. Bruun, and J. J. Arlt, Observation of attractive and repulsive polarons in a Bose-Einstein condensate, Phys. Rev. Lett. **117**, 055302 (2016).

[18] L. A. P. Ardila, N. B. Jørgensen, K. T. Skalmstang, J. J. Arlt, S. Giorgini, G. M. Bruun, and T. Pohl, Analysis of Bose polaron observations, in preparation.

[19] L. Landau and S. Pekar, Effective mass of a polaron, J. Exp. Theor. Phys **18**, 419–423 (1948).

[20] G. D. Mahan, Many-particle physics (Springer Science & Business Media, 2013).

[21] N. Mannella, W. L. Yang, X. J. Zhou, H. Zheng, J. F. Mitchell, J. Zaanen, T. P. Devereaux, N. Nagaosa, Z. Hussain, and Z.-X. Shen, Nodal quasiparticle in pseudogapped colossal magnetoresistive manganites, Nature **438**, 474–478 (2005).

[22] P. A. Lee, N. Nagaosa, and X.-G. Wen, Doping a Mott insulator: physics of high-temperature superconductivity, Rev. Mod. Phys. **78**, 17–85 (2006).

[23] M. E. Gershenson, V. Podzorov, and A. F. Morpurgo, Colloquium: electronic transport in single-crystal organic transistors, Rev. Mod. Phys. **78**, 973–989 (2006).

[24] L. Wacker, N. B. Jørgensen, D. Birkmose, R. Horchani, W. Ertmer, C. Klempt, N. Winter, J. Sherson, and J. J. Arlt, Tunable dual-species Bose-Einstein condensates of ^{39}K and ^{87}Rb, Phys. Rev. A **92**, 053602 (2015).

[25] K. L. Lee, N. B. Jørgensen, I.-K. Liu, L. Wacker, J. J. Arlt, and N. P. Proukakis, Phase separation and dynamics of two-component Bose-Einstein condensates, Phys. Rev. A **94**, 013602 (2016).

[26] K. L. Lee, N. B. Jørgensen, L. Wacker, M. G. Skou, K. T. Skalmstang, J. J. Arlt, and N. P. Proukakis, Time-of-flight expansion of binary Bose-Einstein condensates at finite temperature, arXiv:1712.07481 (2017).

[27] L. J. Wacker, N. B. Jørgensen, D. Birkmose, N. Winter, M. Mikkelsen, J. Sherson, N. Zinner, and J. J. Arlt, Universal three-body physics in ultracold KRb mixtures, Phys. Rev. Lett. **117**, 163201 (2016).

[28] L. Wacker, N. B. Jørgensen, K. T. Skalmstang, M. G. Skou, A. G. Volosniev, and J. J. Arlt, Temperature dependence of an Efimov resonance in ^{39}K, in preparation.

[29] V. Efimov, Energy levels arising from resonant two-body forces in a three-body system, Phys. Lett. B **33**, 563–564 (1970).

[30] N. B. Jørgensen, M. G. Bason, and J. F. Sherson, One- and two-qubit quantum gates using superimposed optical-lattice potentials, Phys. Rev. A **89**, 032306 (2014).

[31] N. B. Jørgensen, D. Birkmose, K. Trelborg, L. Wacker, N. Winter, A. J. Hilliard, M. G. Bason, and J. J. Arlt, A simple laser locking system based on a field-programmable gate array, Rev. Sci. Instrum. **87**, 073106 (2016).

[32] C. D'Errico, M. Zaccanti, M. Fattori, G. Roati, M. Inguscio, G. Modugno, and A. Simoni, Feshbach resonances in ultracold ^{39}K, New J. Phys. **9**, 223 (2007).

[33] A. Simoni, M. Zaccanti, C. D'Errico, M. Fattori, G. Roati, M. Inguscio, and G. Modugno, Near-threshold model for ultracold KRb dimers from interisotope Feshbach spectroscopy, Phys. Rev. A **77**, 052705 (2008).

[34] F. Dalfovo, S. Giorgini, L. P. Pitaevskii, and S. Stringari, Theory of Bose-Einstein condensation in trapped gases, Rev. Mod. Phys. **71**, 463–512 (1999).

[35] J. L. Roberts, N. R. Claussen, S. L. Cornish, E. A. Donley, E. A. Cornell, and C. E. Wieman, Controlled collapse of a Bose-Einstein condensate, Phys. Rev. Lett. **86**, 4211–4214 (2001).

[36] M. Lysebo and L. Veseth, Feshbach resonances and transition rates for cold homonuclear collisions between ^{39}K and ^{41}K atoms, Phys. Rev. A **81**, 032702 (2010).

[37] A. Marte, T. Volz, J. Schuster, S. Dürr, G. Rempe, E. G. M. van Kempen, and B. J. Verhaar, Feshbach resonances in rubidium 87: precision measurement and analysis, Phys. Rev. Lett. **89**, 283202 (2002).

[38] S. N. Bose, Plancks gesetz und lichtquantenhypothese, Z. Phys. **26**, 178–181 (1924).

[39] A. Einstein, Quantentheorie des einatomigen idealen Gases, Sitzungsber. Kgl. Preuss. Akad. Wiss., 261 (1924).

[40] A. Einstein, Quantentheorie des einatomigen idealen Gases, zweite Abhandlung, Sitzungsber. Kgl. Preuss. Akad. Wiss., 3 (1925).

[41] C. J. Pethick and H. Smith, Bose-Einstein condensation in dilute gases, Second Edition (Cambridge University Press, 2002).

[42] T. Nikuni, M. Oshikawa, A. Oosawa, and H. Tanaka, Bose-Einstein condensation of dilute magnons in $TlCuCl_3$, Phys. Rev. Lett. **84**, 5868–5871 (2000).

[43] M. Kubouchi, K. Yoshioka, R. Shimano, A. Mysyrowicz, and M. Kuwata-Gonokami, Study of orthoexciton-to-paraexciton conversion in Cu_2O by excitonic Lyman spectroscopy, Phys. Rev. Lett. **94**, 016403 (2005).

[44] J. Kasprzak, M. Richard, S. Kundermann, A. Baas, P. Jeambrun, J. Keeling, F. Marchetti, M. Szymanska, R. Andre, J. Staehli, V. Savona, P. Littlewood, B. Deveaud, and L. S. Dang, Bose-Einstein condensation of exciton polaritons, Nature **443**, 409 (2006).

[45] J. Klaers, J. Schmitt, F. Vewinger, and M. Weitz, Bose-Einstein condensation of photons in an optical microcavity, Nature **468**, 545–548 (2010).

[46] B. H. Bransden and C. J. Joachain, Physics of atoms and molecules, Second Edition (Pearson Education, 2003).

[47] E. G. M. van Kempen, S. J. J. M. F. Kokkelmans, D. J. Heinzen, and B. J. Verhaar, Interisotope determination of ultracold rubidium interactions from three high-precision experiments, Phys. Rev. Lett. **88**, 093201 (2002).

[48] S. Falke, H. Knöckel, J. Friebe, M. Riedmann, E. Tiemann, and C. Lisdat, Potassium ground-state scattering parameters and Born-Oppenheimer potentials from molecular spectroscopy, Phys. Rev. A **78**, 012503 (2008).

[49] T. Weber, J. Herbig, M. Mark, H.-C. Nägerl, and R. Grimm, Three-body recombination at large scattering lengths in an ultracold atomic gas, Phys. Rev. Lett. **91**, 123201 (2003).

[50] S. Inouye, M. Andrews, J. Stenger, H.-J. Miesner, D. Stamper-Kurn, and W. Ketterle, Observation of Feshbach resonances in a Bose–Einstein condensate, Nature **392**, 151–154 (1998).

[51] C. A. Regal, M. Greiner, and D. S. Jin, Observation of resonance condensation of fermionic atom pairs, Phys. Rev. Lett. **92**, 040403 (2004).

[52] R. J. Fletcher, A. L. Gaunt, N. Navon, R. P. Smith, and Z. Hadzibabic, Stability of a unitary Bose gas, Phys. Rev. Lett. **111**, 125303 (2013).

[53] J. M. Gerton, D. Strekalov, I. Prodan, and R. G. Hulet, Direct observation of growth and collapse of a Bose–Einstein condensate with attractive interactions, Nature **408**, 692–695 (2000).

[54] E. A. Donley, N. R. Claussen, S. L. Cornish, J. L. Roberts, E. A. Cornell, and C. E. Wieman, Dynamics of collapsing and exploding Bose–Einstein condensates, Nature **412**, 295–299 (2001).

[55] T. Lahaye, J. Metz, B. Fröhlich, T. Koch, M. Meister, A. Griesmaier, T. Pfau, H. Saito, Y. Kawaguchi, and M. Ueda, d-wave collapse and explosion of a dipolar Bose-Einstein condensate, Phys. Rev. Lett. **101**, 080401 (2008).

[56] P. A. Altin, G. R. Dennis, G. D. McDonald, D. Döring, J. E. Debs, J. D. Close, C. M. Savage, and N. P. Robins, Collapse and three-body loss in a ^{85}Rb Bose-Einstein condensate, Phys. Rev. A **84**, 033632 (2011).

[57] C. Eigen, A. L. Gaunt, A. Suleymanzade, N. Navon, Z. Hadzibabic, and R. P. Smith, Observation of weak collapse in a Bose-Einstein condensate, Phys. Rev. X **6**, 041058 (2016).

[58] F. Riboli and M. Modugno, Topology of the ground state of two interacting Bose-Einstein condensates, Phys. Rev. A **65**, 063614 (2002).

[59] D. M. Jezek and P. Capuzzi, Interaction-driven effects on two-component Bose-Einstein condensates, Phys. Rev. A **66**, 015602 (2002).

[60] T.-L. Ho and V. B. Shenoy, Binary mixtures of Bose condensates of alkali atoms, Phys. Rev. Lett. **77**, 3276–3279 (1996).

[61] H. Pu and N. P. Bigelow, Properties of two-species Bose condensates, Phys. Rev. Lett. **80**, 1130–1133 (1998).

[62] P. Ao and S. T. Chui, Binary Bose-Einstein condensate mixtures in weakly and strongly segregated phases, Phys. Rev. A **58**, 4836–4840 (1998).

[63] E. Timmermans, Phase separation of Bose-Einstein condensates, Phys. Rev. Lett. **81**, 5718–5721 (1998).

[64] P. Öhberg, Stability properties of the two-component Bose-Einstein condensate, Phys. Rev. A **59**, 634–638 (1999).

[65] M. Trippenbach, K. Góral, K. Rzazewski, B. Malomed, and Y. Band, Structure of binary Bose-Einstein condensates, J. Phys. B At. Mol. Opt. Phys. **33**, 4017 (2000).

[66] K. Kasamatsu and M. Tsubota, Multiple domain formation induced by modulation instability in two-component Bose-Einstein condensates, Phys. Rev. Lett. **93**, 100402 (2004).

[67] H. Takeuchi, S. Ishino, and M. Tsubota, Binary quantum turbulence arising from countersuperflow instability in two-component Bose-Einstein condensates, Phys. Rev. Lett. **105**, 205301 (2010).

[68] L. Wen, W. M. Liu, Y. Cai, J. M. Zhang, and J. Hu, Controlling phase separation of a two-component Bose-Einstein condensate by confinement, Phys. Rev. A **85**, 043602 (2012).

[69] R. W. Pattinson, T. P. Billam, S. A. Gardiner, D. J. McCarron, H. W. Cho, S. L. Cornish, N. G. Parker, and N. P. Proukakis, Equilibrium solutions for immiscible two-species Bose-Einstein condensates in perturbed harmonic traps, Phys. Rev. A **87**, 013625 (2013).

[70] J. Hofmann, S. S. Natu, and S. Das Sarma, Coarsening dynamics of binary Bose condensates, Phys. Rev. Lett. **113**, 095702 (2014).

[71] M. J. Edmonds, K. L. Lee, and N. P. Proukakis, Kinetic model of trapped finite-temperature binary condensates, Phys. Rev. A **91**, 011602 (2015).

[72] J. Polo, V. Ahufinger, P. Mason, S. Sridhar, T. P. Billam, and S. A. Gardiner, Analysis beyond the Thomas-Fermi approximation of the density profiles of a miscible two-component Bose-Einstein condensate, Phys. Rev. A **91**, 053626 (2015).

[73] I.-K. Liu, R. W. Pattinson, T. P. Billam, S. A. Gardiner, S. L. Cornish, T.-M. Huang, W.-W. Lin, S.-C. Gou, N. G. Parker, and N. P. Proukakis, Stochastic growth dynamics and composite defects in quenched immiscible binary condensates, Phys. Rev. A **93**, 023628 (2016).

[74] A. White, T. Hennessy, and T. Busch, Emergence of classical rotation in superfluid Bose-Einstein condensates, Phys. Rev. A **93**, 033601 (2016).

[75] S. B. Papp, J. M. Pino, and C. E. Wieman, Tunable miscibility in a dual-species Bose-Einstein condensate, Phys. Rev. Lett. **101**, 040402 (2008).

[76] D. J. McCarron, H. W. Cho, D. L. Jenkin, M. P. Köppinger, and S. L. Cornish, Dual-species Bose-Einstein condensate of ^{87}Rb and ^{133}Cs, Phys. Rev. A **84**, 011603 (2011).

[77] F. Wang, X. Li, D. Xiong, and D. Wang, A double species ^{23}Na and ^{87}Rb Bose-Einstein condensate with tunable miscibility via an interspecies Feshbach resonance, J. Phys. B At. Mol. Opt. Phys. **49**, 015302 (2015).

[78] Y. Eto, M. Takahashi, M. Kunimi, H. Saito, and T. Hirano, Nonequilibrium dynamics induced by miscible–immiscible transition in binary Bose–Einstein condensates, New J. Phys. **18**, 073029 (2016).

[79] A. S. Jensen, K. Riisager, D. V. Fedorov, and E. Garrido, Structure and reactions of quantum halos, Rev. Mod. Phys. **76**, 215–261 (2004).

[80] T. Kraemer, M. Mark, P. Waldburger, J. Danzl, C. Chin, B. Engeser, A. Lange, K. Pilch, A. Jaakkola, H. Nägerl, and R. Grimm, Evidence for Efimov quantum states in an ultracold gas of caesium atoms, Nature **440**, 315–318 (2006).

[81] E. Braaten and H.-W. Hammer, Universality in few-body systems with large scattering length, Phys. Rep. **428**, 259–390 (2006).

[82] E. Braaten and H.-W. Hammer, Efimov physics in cold atoms, Ann. Phys. (N.Y.) **322**, 120–163 (2007).

[83] F. Ferlaino and R. Grimm, Trend: forty years of Efimov physics: how a bizarre prediction turned into a hot topic, Physics **3**, 9 (2010).

[84] F. Ferlaino, A. Zenesini, M. Berninger, B. Huang, H.-C. Nägerl, and R. Grimm, Efimov resonances in ultracold quantum gases, Few-Body Syst. **51**, 113 (2011).

[85] J. Ulmanis, S. Häfner, E. D. Kuhnle, and M. Weidemüller, Heteronuclear Efimov resonances in ultracold quantum gases, Natl. Sci. Rev. **3**, 174–188 (2016).

[86] E. Nielsen and J. H. Macek, Low-energy recombination of identical bosons by three-body collisions, Phys. Rev. Lett. **83**, 1566–1569 (1999).

[87] B. D. Esry, C. H. Greene, and J. P. Burke, Recombination of three atoms in the ultracold limit, Phys. Rev. Lett. **83**, 1751–1754 (1999).

[88] J. P. D'Incao, H. Suno, and B. D. Esry, Limits on universality in ultracold three-boson recombination, Phys. Rev. Lett. **93**, 123201 (2004).

[89] M. Zaccanti, B. Deissler, C. DErrico, M. Fattori, M. Jona-Lasinio, S. Müller, G. Roati, M. Inguscio, and G. Modugno, Observation of an Efimov spectrum in an atomic system, Nat. Phys. **5** (2009).

[90] S. E. Pollack, D. Dries, and R. G. Hulet, Universality in three- and four-body bound states of ultracold atoms, Science **326**, 1683–1685 (2009).

[91] N. Gross, Z. Shotan, S. Kokkelmans, and L. Khaykovich, Observation of universality in ultracold ^{7}Li three-body recombination, Phys. Rev. Lett. **103**, 163202 (2009).

[92] R. J. Wild, P. Makotyn, J. M. Pino, E. A. Cornell, and D. S. Jin, Measurements of Tan's contact in an atomic Bose-Einstein condensate, Phys. Rev. Lett. **108**, 145305 (2012).

[93] T. B. Ottenstein, T. Lompe, M. Kohnen, A. N. Wenz, and S. Jochim, Collisional stability of a three-component degenerate Fermi gas, Phys. Rev. Lett. **101**, 203202 (2008).

[94] J. H. Huckans, J. R. Williams, E. L. Hazlett, R. W. Stites, and K. M. O'Hara, Three-body recombination in a three-state Fermi gas with widely tunable interactions, Phys. Rev. Lett. **102**, 165302 (2009).

[95] N. Gross, Z. Shotan, S. Kokkelmans, and L. Khaykovich, Nuclear-spin-independent short-range three-body physics in ultracold atoms, Phys. Rev. Lett. **105**, 103203 (2010).

[96] M. Berninger, A. Zenesini, B. Huang, W. Harm, H.-C. Nägerl, F. Ferlaino, R. Grimm, P. S. Julienne, and J. M. Hutson, Universality of the three-body parameter for Efimov states in ultracold cesium, Phys. Rev. Lett. **107**, 120401 (2011).

[97] S. Roy, M. Landini, A. Trenkwalder, G. Semeghini, G. Spagnolli, A. Simoni, M. Fattori, M. Inguscio, and G. Modugno, Test of the universality of the three-body Efimov parameter at narrow Feshbach resonances, Phys. Rev. Lett. **111**, 053202 (2013).

[98] J. Johansen, B. DeSalvo, K. Patel, and C. Chin, Testing universality of Efimov physics across broad and narrow Feshbach resonances, Nat. Phys. (2017).

[99] J. Wang, J. P. D'Incao, B. D. Esry, and C. H. Greene, Origin of the three-body parameter universality in Efimov physics, Phys. Rev. Lett. **108**, 263001 (2012).

[100] C. Chin, Universal scaling of Efimov resonance positions in cold atom systems, arXiv:1111.1484v2 (2011).

[101] P. Naidon, S. Endo, and M. Ueda, Physical origin of the universal three-body parameter in atomic Efimov physics, Phys. Rev. A **90**, 022106 (2014).

[102] Y. Wang and P. S. Julienne, Universal van der Waals physics for three cold atoms near Feshbach resonances, Nat. Phys. **10**, 768–773 (2014).

[103] B. Huang, L. A. Sidorenkov, R. Grimm, and J. M. Hutson, Observation of the second triatomic resonance in Efimov's scenario, Phys. Rev. Lett. **112**, 190401 (2014).

[104] J. R. Williams, E. L. Hazlett, J. H. Huckans, R. W. Stites, Y. Zhang, and K. M. O'Hara, Evidence for an excited-state Efimov trimer in a three-component Fermi gas, Phys. Rev. Lett. **103**, 130404 (2009).

[105] S. Knoop, F. Ferlaino, M. Mark, M. Berninger, H. Schöbel, H.-C. Nägerl, and R. Grimm, Observation of an Efimov-like trimer resonance in ultracold atom-dimer scattering, Nat. Phys. **5**, 227–230 (2009).

[106] S. Nakajima, M. Horikoshi, T. Mukaiyama, P. Naidon, and M. Ueda, Nonuniversal Efimov atom-dimer resonances in a three-component mixture of ^{6}Li, Phys. Rev. Lett. **105**, 023201 (2010).

[107] T. Lompe, T. B. Ottenstein, F. Serwane, K. Viering, A. N. Wenz, G. Zürn, and S. Jochim, Atom-dimer scattering in a three-component Fermi gas, Phys. Rev. Lett. **105**, 103201 (2010).

[108] T. Lompe, T. B. Ottenstein, F. Serwane, A. N. Wenz, G. Zürn, and S. Jochim, Radio-frequency association of Efimov trimers, Science **330**, 940–944 (2010).

[109] S. Nakajima, M. Horikoshi, T. Mukaiyama, P. Naidon, and M. Ueda, Measurement of an Efimov trimer binding energy in a three-component mixture of ^{6}Li, Phys. Rev. Lett. **106**, 143201 (2011).

[110] O. Machtey, Z. Shotan, N. Gross, and L. Khaykovich, Association of Efimov trimers from a three-atom continuum, Phys. Rev. Lett. **108**, 210406 (2012).

[111] C. E. Klauss, X. Xie, C. Lopez-Abadia, J. P. D'Incao, Z. Hadzibabic, D. S. Jin, and E. A. Cornell, Observation of Efimov molecules created from a resonantly interacting Bose gas, Phys. Rev. Lett. **119**, 143401 (2017).

[112] F. Ferlaino, S. Knoop, M. Berninger, W. Harm, J. P. D'Incao, H.-C. Nägerl, and R. Grimm, Evidence for universal four-body states tied to an Efimov trimer, Phys. Rev. Lett. **102**, 140401 (2009).

[113] A. Zenesini, B. Huang, M. Berninger, S. Besler, H.-C. Nägerl, F. Ferlaino, R. Grimm, C. H. Greene, and J. von Stecher, Resonant five-body recombination in an ultracold gas of bosonic atoms, New J. Phys. **15**, 043040 (2013).

[114] B. Huang, L. A. Sidorenkov, and R. Grimm, Finite-temperature effects on a triatomic Efimov resonance in ultracold cesium, Phys. Rev. A **91**, 063622 (2015).

[115] M. Kunitski, S. Zeller, J. Voigtsberger, A. Kalinin, L. P. H. Schmidt, M. Schöffler, A. Czasch, W. Schöllkopf, R. E. Grisenti, T. Jahnke, D. Blume, and R. Dörner1, Observation of the Efimov state of the helium trimer, Science **348**, 551–555 (2015).

[116] Y. Wang, J. Wang, J. P. D'Incao, and C. H. Greene, Universal three-body parameter in heteronuclear atomic systems, Phys. Rev. Lett. **109**, 243201 (2012).

[117] G. Barontini, C. Weber, F. Rabatti, J. Catani, G. Thalhammer, M. Inguscio, and F. Minardi, Observation of heteronuclear atomic Efimov resonances, Phys. Rev. Lett. **103**, 043201 (2009).

[118] R. Pires, J. Ulmanis, S. Häfner, M. Repp, A. Arias, E. D. Kuhnle, and M. Weidemüller, Observation of Efimov resonances in a mixture with extreme mass imbalance, Phys. Rev. Lett. **112**, 250404 (2014).

[119] S.-K. Tung, K. Jiménez-Garca, J. Johansen, C. V. Parker, and C. Chin, Geometric scaling of Efimov states in a ^{6}Li-^{133}Cs mixture, Phys. Rev. Lett. **113**, 240402 (2014).

[120] R. A. W. Maier, M. Eisele, E. Tiemann, and C. Zimmermann, Efimov resonance and three-body parameter in a lithium-rubidium mixture, Phys. Rev. Lett. **115**, 043201 (2015).

[121] R. S. Bloom, M.-G. Hu, T. D. Cumby, and D. S. Jin, Tests of universal three-body physics in an ultracold Bose-Fermi mixture, Phys. Rev. Lett. **111**, 105301 (2013).

[122] K. Kato, Y. Wang, J. Kobayashi, P. S. Julienne, and S. Inouye, Isotopic shift of atom-dimer Efimov resonances in K-Rb mixtures: critical effect of multichannel Feshbach physics, Phys. Rev. Lett. **118**, 163401 (2017).

[123] J. Ulmanis, S. Häfner, R. Pires, E. D. Kuhnle, Y. Wang, C. H. Greene, and M. Weidemüller, Heteronuclear Efimov scenario with positive intraspecies scattering length, Phys. Rev. Lett. **117**, 153201 (2016).

[124] S. Häfner, J. Ulmanis, E. D. Kuhnle, Y. Wang, C. H. Greene, and M. Weidemüller, Role of the intraspecies scattering length in the Efimov scenario with large mass difference, Phys. Rev. A **95**, 062708 (2017).

[125] J. Ulmanis, S. Häfner, R. Pires, E. Kuhnle, M. Weidemüller, and E. Tiemann, Universality of weakly bound dimers and Efimov trimers close to Li–Cs feshbach resonances, New J. Phys. **17**, 055009 (2015).

[126] J. Ulmanis, S. Häfner, R. Pires, F. Werner, D. S. Petrov, E. D. Kuhnle, and M. Weidemüller, Universal three-body recombination and Efimov resonances in an ultracold Li-Cs mixture, Phys. Rev. A **93**, 022707 (2016).

[127] K. Helfrich, H.-W. Hammer, and D. S. Petrov, Three-body problem in heteronuclear mixtures with resonant interspecies interaction, Phys. Rev. A **81**, 042715 (2010).

[128] G. Baym and C. Pethick, Landau Fermi-liquid theory: concepts and applications (John Wiley & Sons, 2008).

[129] R. Bishop, On the ground state of an impurity in a dilute fermi gas, Ann. Phys. (N.Y.) **78**, 391–420 (1973).

[130] E. Dagotto, Correlated electrons in high-temperature superconductors, Rev. Mod. Phys. **66**, 763–840 (1994).

[131] M. Schirber, Focus: Nobel prize—why particles have mass, Physics **6**, 111 (2013).

[132] F. Chevy, Bose polarons that strongly interact, Physics **9**, 86 (2016).

[133] M.-G. Hu, M. J. Van de Graaff, D. Kedar, J. P. Corson, E. A. Cornell, and D. S. Jin, Bose polarons in the strongly interacting regime, Phys. Rev. Lett. **117**, 055301 (2016).

[134] P. Massignan, G. M. Bruun, and H. T. C. Stoof, Spin polarons and molecules in strongly interacting atomic Fermi gases, Phys. Rev. A **78**, 031602 (2008).

[135] N. V. Prokof'ev and B. V. Svistunov, Bold diagrammatic Monte Carlo: a generic sign-problem tolerant technique for polaron models and possibly interacting many-body problems, Phys. Rev. B **77**, 125101 (2008).

[136] N. Prokof'ev and B. Svistunov, Fermi-polaron problem: diagrammatic Monte Carlo method for divergent sign-alternating series, Phys. Rev. B **77**, 020408 (2008).

[137] S. Pilati, G. Bertaina, S. Giorgini, and M. Troyer, Itinerant ferromagnetism of a repulsive atomic Fermi gas: a quantum Monte Carlo study, Phys. Rev. Lett. **105**, 030405 (2010).

[138] X. Cui and H. Zhai, Stability of a fully magnetized ferromagnetic state in repulsively interacting ultracold Fermi gases, Phys. Rev. A **81**, 041602 (2010).

[139] P. Massignan and G. Bruun, Repulsive polarons and itinerant ferromagnetism in strongly polarized Fermi gases, Eur. Phys. J. D **65**, 83–89 (2011).

[140] R. Schmidt and T. Enss, Excitation spectra and rf response near the polaron-to-molecule transition from the functional renormalization group, Phys. Rev. A **83**, 063620 (2011).

[141] M. Cetina, M. Jag, R. S. Lous, J. T. M. Walraven, R. Grimm, R. S. Christensen, and G. M. Bruun, Decoherence of impurities in a Fermi sea of ultracold atoms, Phys. Rev. Lett. **115**, 135302 (2015).

[142] S. Nascimbène, N. Navon, K. J. Jiang, L. Tarruell, M. Teichmann, J. McKeever, F. Chevy, and C. Salomon, Collective oscillations of an imbalanced Fermi gas: axial compression modes and polaron effective mass, Phys. Rev. Lett. **103**, 170402 (2009).

[143] J. Tempere, W. Casteels, M. K. Oberthaler, S. Knoop, E. Timmermans, and J. T. Devreese, Feynman path-integral treatment of the BEC-impurity polaron, Phys. Rev. B **80**, 184504 (2009).

[144] S. P. Rath and R. Schmidt, Field-theoretical study of the Bose polaron, Phys. Rev. A **88**, 053632 (2013).

[145] W. Li and S. Das Sarma, Variational study of polarons in Bose-Einstein condensates, Phys. Rev. A **90**, 013618 (2014).

[146] L. A. P. Ardila and S. Giorgini, Impurity in a Bose-Einstein condensate: study of the attractive and repulsive branch using quantum Monte Carlo methods, Phys. Rev. A **92**, 033612 (2015).

[147] R. S. Christensen, J. Levinsen, and G. M. Bruun, Quasiparticle properties of a mobile impurity in a Bose-Einstein condensate, Phys. Rev. Lett. **115**, 160401 (2015).

[148] J. Levinsen, M. M. Parish, and G. M. Bruun, Impurity in a Bose-Einstein condensate and the Efimov effect, Phys. Rev. Lett. **115**, 125302 (2015).

[149] F. Grusdt, Y. E. Shchadilova, A. N. Rubtsov, and E. Demler, Renormalization group approach to the Fröhlich polaron model: application to impurity-BEC problem, Sci. Rep. **5** (2015).

[150] C. Zipkes, S. Palzer, C. Sias, and M. Köhl, A trapped single ion inside a Bose–Einstein condensate, Nature **464**, 388–391 (2010).

[151] S. Schmid, A. Härter, and J. H. Denschlag, Dynamics of a cold trapped ion in a Bose-Einstein condensate, Phys. Rev. Lett. **105**, 133202 (2010).

[152] J. B. Balewski, A. T. Krupp, A. Gaj, D. Peter, H. P. Büchler, R. Löw, S. Hofferberth, and T. Pfau, Coupling a single electron to a Bose-Einstein condensate, Nature **502**, 664–667 (2013).

[153] S. Ospelkaus, C. Ospelkaus, O. Wille, M. Succo, P. Ernst, K. Sengstock, and K. Bongs, Localization of bosonic atoms by fermionic impurities in a three-dimensional optical lattice, Phys. Rev. Lett. **96**, 180403 (2006).

[154] R. Scelle, T. Rentrop, A. Trautmann, T. Schuster, and M. K. Oberthaler, Motional coherence of fermions immersed in a Bose gas, Phys. Rev. Lett. **111**, 070401 (2013).

[155] N. Spethmann, F. Kindermann, S. John, C. Weber, D. Meschede, and A. Widera, Dynamics of single neutral impurity atoms immersed in an ultracold gas, Phys. Rev. Lett. **109**, 235301 (2012).

[156] P. Naidon, Two impurities in a Bose-Einstein condensate: from Yukawa to Efimov attracted polarons, arXiv:1607.04507 (2016).

[157] L. A. P. Ardila and S. Giorgini, Bose polaron problem: effect of mass imbalance on binding energy, Phys. Rev. A **94**, 063640 (2016).

[158] M. Sun, H. Zhai, and X. Cui, Visualizing the Efimov correlation in Bose polarons, Phys. Rev. Lett. **119**, 013401 (2017).

[159] M. Sun and X. Cui, Enhancing the Efimov correlation in Bose polarons with large mass imbalance, Phys. Rev. A **96**, 022707 (2017).

[160] S. M. Yoshida, S. Endo, J. Levinsen, and M. M. Parish, Universality of an impurity in a Bose-Einstein condensate, arXiv:1710.02968 (2017).

[161] J. Levinsen, M. M. Parish, R. S. Christensen, J. J. Arlt, and G. M. Bruun, Finite-temperature behavior of the Bose polaron, Phys. Rev. A **96**, 063622 (2017).

[162] N.-E. Guenther, P. Massignan, M. Lewenstein, and G. M. Bruun, Bose polarons at finite temperature and strong coupling, arXiv:1708.08861 (2017).

[163] F. Chevy, Universal phase diagram of a strongly interacting Fermi gas with unbalanced spin populations, Phys. Rev. A **74**, 063628 (2006).

[164] Y. E. Shchadilova, R. Schmidt, F. Grusdt, and E. Demler, Quantum dynamics of ultracold Bose polarons, Phys. Rev. Lett. **117**, 113002 (2016).

[165] N. Winter, Creation of ^{39}K Bose-Einstein condensates with tunable interaction, PhD thesis (Aarhus University, 2013).

[166] L. Wacker, Few-body physics with ultracold potassium rubidium mixtures, PhD thesis (Aarhus University, 2015).

[167] G. Kleine-Büning, Lange Kohärenzzeit optisch gefangener Ensembles, PhD thesis (University of Hannover, 2011).

[168] J. Will, Symmetrieabhängige Frequenzverschiebungen in Atomuhren, PhD thesis (University of Hannover, 2012).

[169] G. Kleine Büning, J. Will, W. Ertmer, C. Klempt, and J. Arlt, A slow gravity compensated atom laser, Appl. Phys. B **100**, 117–123 (2010).

[170] G. Kleine Büning, J. Will, W. Ertmer, E. Rasel, J. Arlt, C. Klempt, F. Ramirez-Martinez, F. Piéchon, and P. Rosenbusch, Extended coherence time on the clock transition of optically trapped rubidium, Phys. Rev. Lett. **106**, 240801 (2011).

[171] A. Lercher, T. Takekoshi, M. Debatin, B. Schuster, R. Rameshan, F. Ferlaino, R. Grimm, and H.-C. Nägerl, Production of a dual-species Bose-Einstein condensate of Rb and Cs atoms, Eur. Phys. J. D **65**, 3–9 (2011).

[172] S. Sugawa, R. Yamazaki, S. Taie, and Y. Takahashi, Bose-Einstein condensate in gases of rare atomic species, Phys. Rev. A **84**, 011610 (2011).

[173] S. Stellmer, R. Grimm, and F. Schreck, Production of quantum-degenerate strontium gases, Phys. Rev. A **87**, 013611 (2013).

[174] B. Pasquiou, A. Bayerle, S. M. Tzanova, S. Stellmer, J. Szczepkowski, M. Parigger, R. Grimm, and F. Schreck, Quantum degenerate mixtures of strontium and rubidium atoms, Phys. Rev. A **88**, 023601 (2013).

[175] G. Modugno, M. Modugno, F. Riboli, G. Roati, and M. Inguscio, Two atomic species superfluid, Phys. Rev. Lett. **89**, 190404 (2002).

[176] G. Thalhammer, G. Barontini, L. De Sarlo, J. Catani, F. Minardi, and M. Inguscio, Double species Bose-Einstein condensate with tunable interspecies interactions, Phys. Rev. Lett. **100**, 210402 (2008).

[177] T. Kishimoto, J. Kobayashi, K. Noda, K. Aikawa, M. Ueda, and S. Inouye, Direct evaporative cooling of ^{41}K into a Bose-Einstein condensate, Phys. Rev. A **79**, 031602 (2009).

[178] V. Gokhroo, G. Rajalakshmi, R. K. Easwaran, and C. Unnikrishnan, Sub-Doppler deep-cooled bosonic and fermionic isotopes of potassium in a compact $2D^+$–3D MOT set-up, J. Phys. B At. Mol. Opt. Phys. **44**, 115307 (2011).

[179] M. Landini, S. Roy, G. Roati, A. Simoni, M. Inguscio, G. Modugno, and M. Fattori, Direct evaporative cooling of ^{39}K atoms to Bose-Einstein condensation, Phys. Rev. A **86**, 033421 (2012).

[180] C. Klempt, T. van Zoest, T. Henninger, O. Topic, E. Rasel, W. Ertmer, and J. Arlt, Ultraviolet light-induced atom desorption for large rubidium and potassium magneto-optical traps, Phys. Rev. A **73**, 013410 (2006).

[181] U. Schlöder, H. Engler, U. Schünemann, R. Grimm, and M. Weidemüller, Cold inelastic collisions between lithium and cesium in a two-species magneto-optical trap, Eur. Phys. J. D **7**, 331–340 (1999).

[182] L. G. Marcassa, G. D. Telles, S. R. Muniz, and V. S. Bagnato, Collisional losses in a K-Rb cold mixture, Phys. Rev. A **63**, 013413 (2000).

[183] W. Ketterle, K. B. Davis, M. A. Joffe, A. Martin, and D. E. Pritchard, High densities of cold atoms in a dark spontaneous-force optical trap, Phys. Rev. Lett. **70**, 2253–2256 (1993).

[184] M. H. Anderson, W. Petrich, J. R. Ensher, and E. A. Cornell, Reduction of light-assisted collisional loss rate from a low-pressure vapor-cell trap, Phys. Rev. A **50**, R3597–R3600 (1994).

[185] C. G. Townsend, N. H. Edwards, K. P. Zetie, C. J. Cooper, J. Rink, and C. J. Foot, High-density trapping of cesium atoms in a dark magneto-optical trap, Phys. Rev. A **53**, 1702–1714 (1996).

[186] N. Radwell, G. Walker, and S. Franke-Arnold, Cold-atom densities of more than 10^{12} cm^{-3} in a holographically shaped dark spontaneous-force optical trap, Phys. Rev. A **88**, 043409 (2013).

[187] N. Nemitz, F. Baumer, F. Münchow, S. Tassy, and A. Görlitz, Production of heteronuclear molecules in an electronically excited state by photoassociation in a mixture of ultracold Yb and Rb, Phys. Rev. A **79**, 061403 (2009).

[188] S. Dutta, A. Altaf, J. Lorenz, D. Elliott, and Y. P. Chen, Interspecies collision-induced losses in a dual species ^{7}Li–^{85}Rb magneto-optical trap, J. Phys. B At. Mol. Opt. Phys. **47**, 105301 (2014).

[189] *Aarhus University's Strategy 2013-2020*, http://www.au.dk/en/about/profile/strategy/, 2013.

[190] M. Landini, S. Roy, L. Carcagn, D. Trypogeorgos, M. Fattori, M. Inguscio, and G. Modugno, Sub-doppler laser cooling of potassium atoms, Phys. Rev. A **84**, 043432 (2011).

[191] W. Ketterle and N. Van Druten, Evaporative cooling of trapped atoms, Adv. At. Mol. Opt. Phys. **37**, 181–236 (1996).

[192] G. Modugno, G. Ferrari, G. Roati, R. J. Brecha, A. Simoni, and M. Inguscio, Bose-Einstein condensation of potassium atoms by sympathetic cooling, Science **294**, 1320–1322 (2001).

[193] G. Ferrari, M. Inguscio, W. Jastrzebski, G. Modugno, G. Roati, and A. Simoni, Collisional properties of ultracold K-Rb mixtures, Phys. Rev. Lett. **89**, 053202 (2002).

[194] M. J. Edmonds, K. L. Lee, and N. P. Proukakis, Nonequilibrium kinetic theory for trapped binary condensates, Phys. Rev. A **92**, 063607 (2015).

[195] M. Zaccanti, C. D'Errico, F. Ferlaino, G. Roati, M. Inguscio, and G. Modugno, Control of the interaction in a Fermi-Bose mixture, Phys. Rev. A **74**, 041605 (2006).

[196] S. Tojo, Y. Taguchi, Y. Masuyama, T. Hayashi, H. Saito, and T. Hirano, Controlling phase separation of binary Bose-Einstein condensates via mixed-spin-channel Feshbach resonance, Phys. Rev. A **82**, 033609 (2010).

[197] E. Nicklas, H. Strobel, T. Zibold, C. Gross, B. A. Malomed, P. G. Kevrekidis, and M. K. Oberthaler, Rabi flopping induces spatial demixing dynamics, Phys. Rev. Lett. **107**, 193001 (2011).

[198] S. Ospelkaus, C. Ospelkaus, L. Humbert, K. Sengstock, and K. Bongs, Tuning of heteronuclear interactions in a degenerate Fermi-Bose mixture, Phys. Rev. Lett. **97**, 120403 (2006).

[199] E. Zaremba, T. Nikuni, and A. Griffin, Dynamics of trapped Bose gases at finite temperatures, J. Low. Temp. Phys. **116**, 277–345 (1999).

[200] C. Ospelkaus and S. Ospelkaus, Heteronuclear quantum gas mixtures, J. Phys. B At. Mol. Opt. Phys. **41**, 203001 (2008).

[201] R. Grimm, M. Weidemüller, and Y. B. Ovchinnikov, Optical dipole traps for neutral atoms, Adv. At. Mol. Opt. Phys. **42**, 95–170 (2000).

[202] D. S. Hall, M. R. Matthews, J. R. Ensher, C. E. Wieman, and E. A. Cornell, Dynamics of component separation in a binary mixture of Bose-Einstein condensates, Phys. Rev. Lett. **81**, 1539–1542 (1998).

[203] J. J. Chang, P. Engels, and M. A. Hoefer, Formation of dispersive shock waves by merging and splitting Bose-Einstein condensates, Phys. Rev. Lett. **101**, 170404 (2008).

[204] S. Ivanov and A. Kamchatnov, Expansion dynamics of a two-component quasi-one-dimensional Bose–Einstein condensate: phase diagram, self-similar solutions, and dispersive shock waves, J. Exp. Theor. Phys **124**, 546–563 (2017).

[205] A. Marte, T. Volz, J. Schuster, S. Dürr, G. Rempe, E. G. M. van Kempen, and B. J. Verhaar, Feshbach resonances in rubidium 87: precision measurement and analysis, Phys. Rev. Lett. **89**, 283202 (2002).

[206] M. Mikkelsen, A. Jensen, D. Fedorov, and N. T. Zinner, Three-body recombination of two-component cold atomic gases into deep dimers in an optical model, J. Phys. B At. Mol. Opt. Phys. **48**, 085301 (2015).

[207] M.-G. Hu, R. S. Bloom, D. S. Jin, and J. M. Goldwin, Avalanche-mechanism loss at an atom-molecule Efimov resonance, Phys. Rev. A **90**, 013619 (2014).

[208] G. Thalhammer, G. Barontini, J. Catani, F. Rabatti, C. Weber, A. Simoni, F. Minardi, and M. Inguscio, Collisional and molecular spectroscopy in an ultracold Bose–Bose mixture, New J. Phys. **11**, 055044 (2009).

[209] E. Tiemann, Private communication.

[210] M. W. Zwierlein, Z. Hadzibabic, S. Gupta, and W. Ketterle, Spectroscopic insensitivity to cold collisions in a two-state mixture of Fermions, Phys. Rev. Lett. **91**, 250404 (2003).

[211] N. B. Jørgensen, Few-body physics in ultracold mixtures of potassium and rubidium, part-A dissertation, Aarhus University, 2015.

[212] M. M. Parish and J. Levinsen, Quantum dynamics of impurities coupled to a Fermi sea, Phys. Rev. B **94**, 184303 (2016).

[213] P. Makotyn, C. E. Klauss, D. L. Goldberger, E. Cornell, and D. S. Jin, Universal dynamics of a degenerate unitary Bose gas, Nat. Phys. **10**, 116–119 (2014).

[214] C. Eigen, J. A. P. Glidden, R. Lopes, N. Navon, Z. Hadzibabic, and R. P. Smith, Universal scaling laws in the dynamics of a homogeneous unitary Bose gas, Phys. Rev. Lett. **119**, 250404 (2017).

[215] T. Rentrop, A. Trautmann, F. A. Olivares, F. Jendrzejewski, A. Komnik, and M. K. Oberthaler, Observation of the phononic Lamb shift with a synthetic vacuum, Phys. Rev. X **6**, 041041 (2016).

[216] M. Hohmann, F. Kindermann, T. Lausch, D. Mayer, F. Schmidt, E. Lutz, and A. Widera, Individual tracer atoms in an ultracold dilute gas, Phys. Rev. Lett. **118**, 263401 (2017).

[217] F. Camargo, R. Schmidt, J. Whalen, R. Ding, G. Woehl Jr, S. Yoshida, J. Burgdorfer, F. Dunning, H. Sadeghpour, E. Demler, and T. Killian, Creation of Rydberg polarons in a Bose gas, arXiv:1706.03717v3 (2017).

[218] B. Midya, M. Tomza, R. Schmidt, and M. Lemeshko, Rotation of cold molecular ions inside a Bose-Einstein condensate, Phys. Rev. A **94**, 041601 (2016).

[219] N. J. S. Loft, Z. Wu, and G. M. Bruun, Mixed-dimensional Bose polaron, Phys. Rev. A **96**, 033625 (2017).

[220] L. Parisi and S. Giorgini, Quantum Monte Carlo study of the Bose-polaron problem in a one-dimensional gas with contact interactions, Phys. Rev. A **95**, 023619 (2017).

[221] Y. Ashida, R. Schmidt, L. Tarruell, and E. Demler, Many-body interferometry of magnetic polaron dynamics, arXiv:1701.01454v2 (2017).

[222] F. Grusdt, K. Seetharam, Y. Shchadilova, and E. Demler, Strong coupling Bose polarons out of equilibrium: dynamical RG approach, arXiv:1711.03478v2 (2017).

[223] T. Lausch, A. Widera, and M. Fleischhauer, Prethermalization in the cooling dynamics of an impurity in a BEC, arXiv:1708.09242 (2017).

[224] T. Lausch, A. Widera, and M. Fleischhauer, Role of thermal two-phonon scattering for impurity dynamics in a low-dimensional BEC, arXiv:1712.07912 (2017).

[225] R. Schmidt, M. Knap, D. A. Ivanov, J.-S. You, M. Cetina, and E. Demler, Universal many-body response of heavy impurities coupled to a Fermi sea, arXiv:1702.08587 (2017).

[226] M. Sidler, P. Back, O. Cotlet, A. Srivastava, T. Fink, M. Kroner, E. Demler, and A. Imamoglu, Fermi polaron-polaritons in charge-tunable atomically thin semiconductors, Nat. Phys. **13**, 255–261 (2017).

[227] G. M. Bruun, Private communication.

[228] T. D. Lee, K. Huang, and C. N. Yang, Eigenvalues and eigenfunctions of a Bose system of hard spheres and its low-temperature properties, Phys. Rev. **106**, 1135–1145 (1957).

[229] D. S. Petrov, Quantum mechanical stabilization of a collapsing Bose-Bose mixture, Phys. Rev. Lett. **115**, 155302 (2015).

[230] C. Cabrera, L. Tanzi, J. Sanz, B. Naylor, P. Thomas, P. Cheiney, and L. Tarruell, Quantum liquid droplets in a mixture of Bose-Einstein condensates, Science, published online (eaao5686) (2017).

[231] P. Cheiney, C. Cabrera, J. Sanz, B. Naylor, L. Tanzi, and L. Tarruell, Bright soliton to quantum droplet transition in a mixture of Bose-Einstein condensates, arXiv:1710.11079 (2017).

[232] G. Semeghini, G. Ferioli, L. Masi, C. Mazzinghi, L. Wolswijk, F. Minardi, M. Modugno, G. Modugno, M. Inguscio, and M. Fattori, Self-bound quantum droplets in atomic mixtures, arXiv:1710.10890 (2017).

[233] H. Kadau, M. Schmitt, M. Wenzel, C. Wink, T. Maier, I. Ferrier-Barbut, and T. Pfau, Observing the Rosensweig instability of a quantum ferrofluid, Nature **530**, 194–197 (2016).

[234] L. Chomaz, S. Baier, D. Petter, M. J. Mark, F. Wächtler, L. Santos, and F. Ferlaino, Quantum-fluctuation-driven crossover from a dilute Bose-Einstein condensate to a macrodroplet in a dipolar quantum fluid, Phys. Rev. X **6**, 041039 (2016).

[235] I. Ferrier-Barbut, H. Kadau, M. Schmitt, M. Wenzel, and T. Pfau, Observation of quantum droplets in a strongly dipolar Bose gas, Phys. Rev. Lett. **116**, 215301 (2016).

[236] M. Schmitt, M. Wenzel, F. Böttcher, I. Ferrier-Barbut, and T. Pfau, Self-bound droplets of a dilute magnetic quantum liquid, Nature **539**, 259–262 (2016).

[237] N. B. Jørgensen, Single- and two-qubit quantum gates using superimposed optical lattice potentials, bachelor's thesis (Aarhus University, 2012).

[238] D. Birkmose, Investigation of dual species Bose-Einstein condensates, MA thesis (Aarhus University, 2015).